EXCHANGE FLOW THROUGH A CHANNEL WITH AN UNDERWATER SILL

by

ZHIWEI ZHU

B.Sc.	Shanghai Jiao Tong University, China	1986
M.Sc.	Shanghai Jiao Tong University, China	1989
M.Eng.	University of British Columbia	1991

A THESIS SUBMITTED IN PARTIAL FULFILLMENT OF

THE REQUIREMENTS FOR THE DEGREE OF

DOCTOR OF PHILOSOPHY

in

THE FACULTY OF GRADUATE STUDIES

DEPARTMENT OF CIVIL ENGINEERING

We accept this thesis as conforming

to the required standard

THE UNIVERSITY OF BRITISH COLUMBIA

July, 1996

Department of Civil Engineering

The University of British Columbia
2324 Main Mall
Vancouver, Canada
V6T 1Z4

Date: July, 1996

ABSTRACT

The gravitational exchange of fluids between two bodies of water of slightly different density through a channel with a smooth two-dimensional underwater sill is studied theoretically and experimentally. Internal hydraulic theory is extended to incorporate the effects of streamline curvature caused by the sill. The extended theory is applied to both single and two-layer flows. Unlike internal hydraulic theory which fails to predict a whole class of two-layer flows, namely, approach-controlled flows, the extended theory with non-hydrostatic pressure considered achieves excellent agreement with previous experimental measurements.

Internal hydraulic theory is further extended to incorporate the effects of friction caused by the channel and the two-layer interface, as well as the streamline curvature. For the exchange flow through a channel of constant width with a sill, maximal exchange occurs when both sill and exit controls are present. With the effects of curvature and friction considered, the sill control is shifted away from the sill crest, and the internal energy is no longer constant. Exchange flows established in the laboratory are studied using flow visualization, particle tracking, and image processing techniques. The friction factors for the sidewalls and bottom are estimated using boundary layer theories, while the interfacial friction factor is determined experimentally. The friction reduces the internal energy throughout the channel, significantly increases the interface slope and reduces the flow rate. The frictional effect is important throughout the channel, whereas the curvature effect is mainly important in the sill region. With both effects included, the exchange flow over a sill is accurately predicted.

On the interface of exchange flows, interfacial instabilities are observed, with Kelvin-Helmholtz instabilities at both ends of the channel where shear is strong, and Holmboe instabilities in the middle region where shear is weaker. The Holmboe instabilities have been studied in detail. The existence of the negative shift, *i.e.*, the shear center being lower than the

density interface, is confirmed. This shift initially results in non-symmetric Holmboe waves. Later in the experiments, the shift reduces to zero and symmetric Holmboe waves are observed. The growth rate, wave lengths, and wave speeds of the Holmboe instabilities are measured and found to be in agreement with the linear stability theory of Haigh (1995). Variations in wave speeds when the positive and negative waves pass through each other have been observed for the first time experimentally. The Holmboe waves are stabilized when the bulk Richardson number exceeds about 0.8.

TABLE OF CONTENTS

List of Tables

List of Figures

Figure | Page

List of Symbols

Roman

b	width of the channel
$c = c_r + ic_i$	complex wave speed
d	shift of the shear center and the density interface
E	mechanical energy per unit volume for single-layer flow or internal energy for two-layer flow
E_i	mechanical energy per unit volume of layer i
$F = U^2/gy$	Froude number for single-layer flow
$F_i^2 = U_i^2/g'y_i$	densimetric Froude number for layer i
f_I	interfacial frictional factor
f_w	sidewall frictional factor
$G^2 = F_1^2 + F_2^2$	composite internal Froude number
g	gravitational acceleration
$g' = g(\rho_2 - \rho_1)/\rho_2$	reduced gravitational acceleration
h	sill height
h_m	maximum sill height
$J = g'\delta/(\Delta U)^2$	bulk Richardson number
$K = (\Delta U)^3/g'\nu$	Keulegan number
L	horizontal scale or length of the channel
L_s	length of the sill
P	pressure
q	flow rate per unit width
q_i	flow rate per unit width for layer i
Q	volumetric flow rate
Q_i	volumetric flow rate for layer i

$r = \rho_1/\rho_2$	relative density difference
R	hydraulic radius
$R = \delta/\eta$	ratio of the shear layer thickness to density layer thickness
$Re = \Delta U\ \delta/\nu$	shear Reynolds number
$Re_x = \overline{U}\ x/\nu$	layer Reynolds number
$s = h+y$	elevation of the free surface for one-layer flow
$s = h+y_1+y_2$	elevation of the free surface for two-layer flow
S_c	curvature slope
S_f	frictional slope
S_0	topographic slope
t	time
$T_H = L/\sqrt{g'H}$	time scale for the study of hydraulics
$T_s = \delta/(\frac{1}{2}\Delta U)$	time scale for the study of interfacial stability
u	horizontal velocity
U	horizontal mean velocity
$U_i = q_i/y_i$	horizontal mean velocity for layer i
	or maximal velocity for layer i in stability analysis
$\overline{U} = \frac{1}{2}(U_1 + U_2)$	mean velocity
$\Delta U = \lvert U_1 - U_2 \rvert$	velocity difference between two layers
w	vertical velocity
x	horizontal coordination
y	layer thickness for sing-layer flow
$y = h+y_2$	elevation of the interface for two-layer flows
y_i	thickness (or depth) of layer i
z	vertical coordination

Subscripts and superscripts

H, NH	hydrostatic or non-hydrostatic component
i (i = 1, 2)	parameters for layer i
I	parameters for the interface
I, w, s	friction due to the interface, walls or surface
r, i	real or imaginary component of the complex wave speed
R, L	parameters for the right or left reservoir
s, e	parameters at the sill crest or the channel right hand exit
+, -	positive or negative waves
*	non-dimensional parameter

Greek

$\alpha = 2\pi\delta / \lambda$	non-dimensional wave number
δ	thickness of interfacial shear layer
η	thickness of interfacial density layer
$\varepsilon = \Delta\rho/\rho_2$	relative density difference
$\varepsilon = 2d / \delta$	non-dimensional shift of the density interface from the shear center
$\sigma = (H / L)^2$	shallowness parameter
σ_t	density unit, where ρ in kg/m^3 can be expressed by 1000 + σ_t
ρ	density
ρ_i	density for layer i
$\Delta\rho$	density difference
λ	wave length
τ	shear stress

Acknowledgments

This thesis would not be possible without the constant guidance and encouragement from my supervisor, Professor Gregory A. Lawrence. I thank him for his help, patience and consideration: he made my student life much more enjoyable than it would otherwise be. Also I would like to thank the other members of my supervisory committee for their helpful suggestions in the preparation of this document.

Throughout the course of the research work and in the preparation of this thesis, I received generous help and valuable suggestions from my colleagues: Dr. Craig Stevens in image processing and experimental setups; Dr. Noboru Yonemitsu in many enlightening discussions on instabilities; Dr. Roger Pieters in correcting my English and in discussions on hydraulics. I would also like to thank Professor Uri Ascher for providing me his code COLNEW, and Dr. Paul Hamblin of National Water Research Institute for many constructive suggestions.

My appreciation also goes to Wayne Evans, Susan Haigh, Michael MacLatchy, Jason Vine, and other friends in the Environmental Fluid Mechanics group for their help in checking my English and in various other things. I also thank Thomas Wong for his help in my unique computing requirements.

Finally, a special thanks to my wife Jufang for her understanding and support during the long period of my Ph.D. program.

Financial support from the Natural Sciences and Engineering Research Council (NSERC) and a Graduate Fellowship from the University of British Columbia is gratefully acknowledged.

Chapter 1

INTRODUCTION

Adjacent water bodies connected by straits or channels often have slightly different densities as a result of differences in temperature, salinity, and/or sediment concentration. These density differences can drive a gravitational exchange flow between the two bodies of fluid. One example which has attracted considerable interest is the exchange of more saline Mediterranean sea water with less saline Atlantic Ocean water through the Strait of Gibraltar, as indicated in Figure 1.1 (Knauss 1978; Armi & Farmer 1988). Important exchange flows also occur in other straits, such as the Bosphorus connecting the Black Sea and the Marmara Sea (Oguz *et al.* 1990), the Strait of Bab el Mandeb connecting the Indian Ocean with the highly saline Red Sea, and the Strait of Hormuz connecting the Arabian Sea and the Persian Gulf (Defant 1961). The understanding of exchange flows is also important in many environmental engineering problems. Some examples include the desire to avoid any reduction in the exchange flow through the Great Belt linking the Baltic to the North Sea after the construction of a bridge (Ottesen-Hansen & Moeller 1990), and the impact of the summertime exchange of warmer, heavily polluted Hamilton Harbor water with cooler (more dense) Lake Ontario water through the Burlington ship canal (Hamblin & Lawrence 1990).

A better understanding of exchange flows should consider the effects of channel topography and the friction caused by both the channel walls and by the interface between the two layers. Previous studies on two-layer flows over topography use hydraulic theory where the vertical velocity is neglected and pressure is therefore hydrostatic (Long 1954; Baines 1984, 1988; Armi 1986). This hydraulic approach is generally valid in which the streamline curvature is minimal. However, the effects of streamline curvature and non-hydrostatic pressure cannot always be ignored for two-layer flows over a sill, (Lawrence 1993). Non-hydrostatic effects are also found to be important in other flow situations, such as the flow over certain types of ridges (Rottman & Smith 1989), and the two-layer flow through a contraction (Helfrich 1994). Non-hydrostatic effects might also be responsible for the "plunging flows" observed over fjord sills (Farmer & Denton 1985).

Friction, especially interfacial friction, may significantly reduce the magnitude of exchange flows (Hamblin & Lawrence 1990; Dalziel 1990), and determines the dynamics of saline wedge flows (Arita & Jirka 1987; Yonemitsu 1996). Despite its importance, the factors influencing the interfacial friction factor are not well understood. A number of empirical and semi-empirical formulations have been proposed to predict the interfacial friction factor (Dermisses & Partheniades 1984; Arita & Jirka 1987). However, for any particular flow the values given by these formulations may vary by up to an order of magnitude (Cheung & Lawrence 1991). Given that interfacial friction is a function of interfacial flow parameters, a better understanding of the interfacial phenomena will enhance our ability to predict interfacial friction.

The interfacial region between the two-layers in an exchange flow is characterized by strong velocity and density gradients. If the vertical extent of the velocity variation (sometimes known as the "vorticity thickness" or "shear layer thickness") is much greater than the thickness of the density interface, as is the case in many salinity stratified flows, interfacial instabilities, known as Kelvin-Helmholtz (Kelvin 1871; Helmholtz 1868) and Holmboe instabilities (Holmboe 1962), (see Figure 1.2), are generated. The type of the instability generated depends on the relative significance of the gravitational force and the shear force, measured by the Richardson number. When the Richardson number is small, *i.e.* shear is strong, Kelvin-Helmholtz instabilities are observed. When the Richardson number is large, *i.e.* stratification is strong, Holmboe instabilities are observed, where two sets of waves having the same growth rate propagate in opposite directions at the same speed with respect to the mean flow velocity. When the flow is non-symmetric with the center of the shear layer displaced from the center of the density interface, then the two sets of waves have different growth rates and propagation speeds (Lawrence *et al.* 1991; Haigh 1995). Holmboe instabilities are generated with relatively less shear and hence might be more common in nature. A better understanding of interfacial instabilities is important in many applications in oceanography, meteorology, and environmental engineering, since they are fundamental to the generation of turbulence and mixing in stably stratified shear flows (Thorpe 1987). The study of these instabilities is also one of the fundamental problems in the field of the hydrodynamic stability.

In this thesis, theoretical and experimental studies are conducted on the effects of streamline curvature and friction on exchange flows over a two-dimensional obstacle through a channel of constant width. The interfacial instabilities are studied experimentally, with special attention paid to Holmboe instabilities. This study is restricted to two-layer flows with a small density difference. Barotropic forcing and Coriolis effects are also neglected. The barotropic force can be accommodated without difficulty for the quasi-steady exchange flows (Armi & Farmer 1986). Coriolis force may be important for some large scale flow problems. It, however, does not alter the essential results, as is shown for the exchange flow through the Strait of Gibraltar, (Bormans & Garrett 1989; Dalziel 1991).

Chapter Two starts with a review of the studies of two-layer flows using hydraulic theory, assuming the flow is inviscid and hydrostatic. Studies on the effects of streamline curvature and friction in single-layer or two-layer flows are then reviewed, together with a survey of interfacial friction effects. This is followed by a review of theoretical and experimental studies on interfacial instabilities in two-layer flows.

Chapter Three describes the experimental apparatus and experimental techniques utilized to study exchange flows. Instantaneous information on velocity fields and interface positions are obtained using various flow visualization, particle tracking, and image processing techniques, while the density profiles are measured using a conductivity probe. A brief description of the experimental design and the experimental procedure is also given.

Chapter Four discusses the evolution of the exchange flows conducted in the laboratory. As the flow evolves, its mean properties (the flow rate and the interface position) change. The various regimes through which the flow passes are discussed. During some period of the experiments, Holmboe instabilities are observed at the interface of the two layers. The development of these Holmboe waves is discussed qualitatively.

Chapters Five and Six are devoted to the study of hydraulics of the mean flow. Chapter Five investigates the effects of streamline curvature on layered flows over a sill. Hydraulic theory is extended to incorporate the effects of the streamline curvature for a general layer in a multi-layer flows. The extended theory is directly applied to single-layer flows, and is compared with other theoretical and experimental studies on single-layer flows. The theory is also applied to uni-directional two-layer flows over a sill. The experimental observations of Lawrence (1993), where hydraulic theory fails, are explained using this theory. In Chapter Six, hydraulic theory is extended to include both effects of streamline curvature and friction in exchange flows over a sill. The friction factors for the bottom and sidewalls of the channel are obtained from boundary layer theories, whereas the interfacial friction factor is estimated from experimental measurements. Using these friction factors, comparisons are made between the extended theory and the experimental measurements.

Chapter Seven presents quantitative studies on the Holmboe instabilities observed in the experiments. The development and propagation of Holmboe waves are studied by measuring the wave growth rate, wave length and wave speed. The results are compared with linear stability theories. The conditions needed to generate Holmboe instabilities are also examined.

Chapter Eight discusses some two-layer flows that are of concern to civil and environmental engineers. The importance of friction is studied, and an engineering initiative to reduce the excessive saline intrusion is considered. Some field observations of interfacial instabilities are also reported. The thesis is summarized in Chapter Nine.

Chapter 2

LITERATURE REVIEW

2.1 HYDRAULICS OF TWO-LAYER FLOWS

Many flows of oceanographic, meteorological, and engineering importance can be modeled as homogeneous layers of inviscid fluid with negligibly small vertical velocities. Consequently, the pressure distribution can be considered hydrostatic and the horizontal velocity uniform across the depth (Whitham 1974). The resulting equations, called the hydraulic (or shallow water) equations, are used extensively in the study of single-layer flows, see, for example, Henderson (1966). The extension of the hydraulic equations to two-layer flows, forming the basis of internal hydraulic theory, was first described by Stommel & Farmer (1953) and Schijf & Schonfeld (1953) in studying the intrusion of salt water into estuaries and rivers. Internal hydraulic theory was later used to study many other two-layer flow problems: two-layer flows through a channel with a width-contraction (Wood 1968, 1970), two-layer flows over a broad-crested weir (Wood & Lai 1972), two-layer flows over a sill by towing a bottom/surface obstacle (Long 1954, 1974; Baines 1984, 1988) or by using a stationary bottom obstacle (Lawrence 1993), and two-layer exchange flow through the combination of a contraction and a sill (Armi 1986; Farmer & Armi 1986; Dalziel 1988, 1991; Garrett *et al.* 1990). Here internal hydraulic theory for inviscid two-layer flow through a channel with an underwater sill is briefly summarized. This is followed by a review of the studies on friction and curvature effects.

2.1.1 Hydraulics of Inviscid Hydrostatic Two-layer Flows

Steady, two-layer, inviscid, hydrostatic, irrotational flows through a channel with a two-dimensional sill, as illustrated in Figure 2.1, can be studied using the mechanical energy (or

Bernoulli constant) E_i, which is conserved in each layer in the absence of internal hydraulic jumps. We write

$$E_i = P_i + \rho_i g z + \tfrac{1}{2}\rho_i U_i^2, \tag{2.1}$$

where U_i, ρ_i and P_i are the horizontal velocity, density and pressure for layer i, respectively. Subscripts i = 1, 2 relate to the upper and lower layer, respectively. g is the gravitational acceleration, and z is the vertical coordinate. The pressure P_i can be expressed, after applying zero pressure at the free surface, as:

$$P_1 = \rho_1 g(s - z), \tag{2.2}$$

$$P_2 = \rho_1 g y_1 + \rho_2 g(s - y_1 - z), \tag{2.3}$$

where s is the elevation of the free surface, and y_i is the thickness of the layer i.

Define the internal energy E as

$$E = \frac{E_2 - E_1}{(\rho_2 - \rho_1)g}, \tag{2.4}$$

and substituting (2.1) - (2.3) into (2.4), we obtain

$$E = y_2 + h + \frac{1}{2g'}(U_2^2 - rU_1^2), \tag{2.5}$$

where h is the sill height, $r = \rho_1/\rho_2$, $g' = \varepsilon g$ is the reduced gravity, $\varepsilon = (\rho_2 - \rho_1)/\rho_2 = 1 - r$.

Given that E_1 and E_2 are conserved, E is also conserved. Using $y_1 + y_2 + h = s$, and dE/dx = 0, the slope of the interface, y_x, ($y = y_2 + h$), can be expressed as

$$y_x = -\frac{1}{1 - rF_1^2 - F_2^2}\{F_2^2 h_x + (rF_1^2 y_1 - F_2^2 y_2)\frac{b_x}{b} + rF_1^2 s_x\}, \tag{2.6}$$

where b is the channel width, x is the horizontal coordinate, subscript x denotes the differentiation with respect to x, $F_i^2 = U_i^2/g'y_i$ is the densimetric Froude number.

Knowing that dE_1/dx = 0, and applying Eq. (2.6), the slope of the free surface, s_x, becomes

$$s_x = \frac{\varepsilon F_1^2}{1-G^2}(F_2^2 h_x + (y_1 - F_2^2 y_2)\frac{b_x}{b}), \tag{2.7}$$

where $G^2 = F_1^2 + F_2^2 - \varepsilon F_1^2 F_2^2$ is the composite internal Froude number.

When the density difference between the two layers is small, *i.e.* $\varepsilon << 1$, (the Boussinesq approximation), we can write

$$G^2 = F_1^2 + F_2^2,$$

and the interface slope, y_x,

$$y_x = -\frac{1}{1-G^2}\{F_2^2 h_x + (F_1^2 y_1 - F_2^2 y_2)\frac{b_x}{b}\}. \tag{2.8}$$

When $F_i^2 = O(1)$, $s_x = O(\varepsilon) << 1$, and the slope of the free surface is negligible compared to that of the interface. This is commonly referred as the "rigid lid" or horizontal free surface assumption. In this study, we are interested only in the flows with small density difference. Thus the "rigid lid" assumption can be applied.

The composite Froude number, G^2, serves the same role for two-layer flows, as the classical Froude number does for single-layer, open channel flows, (see, for example, Henderson 1966), *i.e.*, the locations where $G^2 = 1$ are described as (internal) control points, and the flow is supercritical (or subcritical) when $G^2 > 1$ (or $G^2 < 1$). At control points where $G^2 = 1$, $F_2^2 h_x + (F_1^2 y_1 - F_2^2 y_2)\frac{b_x}{b} = 0$ and the interface slope $y_x \neq 0$. These conditions can be used to identify the location of the controls.

For exchange flows through a channel of constant width with a sill, see Figure 2.2, for a wide range of reservoir conditions, there exits two controls, located at the sill crest point and the channel right hand exit (Armi 1986; Farmer & Armi 1986). To the left of the sill crest the lower layer accelerates down the sill as a supercritical flow ($G^2 > 1$). The interface of the two layers then matches that of the left hand reservoir through an internal hydraulic jump or turbulent mixing. Upon exiting from the channel, the upper layer accelerates, and the interface eventually matches that of the right hand reservoir through turbulent mixing. The existence of the two controls effectively isolates the flow in the channel from the changes in the interface positions in either reservoir. The subcritical channel region bounded by the sill control and the exit control is separated from the outside reservoirs by the supercritical flows outside it. The flow rate, as well as the interface level between the controls, is independent of the flow conditions in the reservoirs. Such exchange flows with two controls have the maximum flow rate for the given channel geometry, and are called maximal exchange flows.

When the interface level in the left-hand reservoir is sufficiently high, or that in the right-hand is sufficiently low, the sill or the exit control can be submerged. The exchange flow with only one control is called submaximal exchange flow. Figure 2.2c shows a submaximal flow with the sill control while the exit control is submerged. The submaximal exchange has smaller flow rate and, in contrast to the maximal exchange, is no longer isolated from the reservoir conditions. The reservoir conditions required for maximal exchanges were studied by Armi (1986) and Farmer & Armi (1986) neglecting the energy loss due to the channel entrance. In this study of internal hydraulics, we are primarily interested in maximal exchange flows.

A number of processes not included here have been described in the literature. The barotropic forces on exchange flows were considered by Armi & Farmer (1986) and Farmer & Armi (1986) for quasi-steady flows. Some other effects were also studied for two-layer flows: the effect of the rotation (of the earth) and cross-channel geometry on exchange flows (Dalziel 1991), the unsteady two-layer flow over a sill with barotropic tides (Geyer 1990), the unsteady exchange flows through a contraction (Helfrich 1994), and the pulse started two-layer flow over an obstruction (Jameel 1991). In the present study we neglect these effects so that we can concentrate on the effects of the non-hydrostatic pressure distributions and the friction forces due to the sidewalls and bottom of the channel, as well as the interface between the two layers.

2.1.2 Effects of Streamline Curvature

Though hydraulic theory is usually valid for flows with much larger horizontal than vertical scales, it fails to explain a whole class of two-layer flow over a sill, namely, approach-controlled flows (Lawrence 1993). Figure 2.3 shows a typical approach-controlled flow over a bottom sill in a constant width channel. The flow is internally critical near the foot of the sill. It starts passing the sill supercritically, and is followed by an internal hydraulic jump This asymmetric flow behavior cannot be explained using hydraulic theory with the assumption of hydrostatic pressure distribution (Lawrence 1993), as hydraulic theory will predict a symmetric interface profile over the sill. Non-hydrostatic effects are also found to be important in stratified flows over ridges (Rottman & Smith 1989), and two-layer flows over some fjords (Farmer & Smith 1985). A brief review of previous studies incorporating the effects of streamline curvature is presented here.

Several studies have addressed the effects of streamline curvature in single-layer flows. Dressler (1978) and Sivakumaran *et al.* (1981, 1983) have successfully studied single-layer flows over curved beds by transforming the equations of motion using orthogonal curvilinear co-ordinates. Unfortunately, their approach is not amenable to two-layer flows. Naghdi & Vongsarnpigoon (1986) have used the direct theory of constrained fluid sheets to accurately describe single-layer flows. However, their method did not provide pressure information, and thus cannot be applied to two-layer flow problems. They also failed to solve their equation (non-linear second order ordinary differential equation) for the surface profiles. Pratt (1984) studied single-layer flow over multiple obstacles using asymptotic methods. While he restricted the sill to be small, his method could be extended to two-layer flows.

Other techniques have been developed that apply to both single and two-layer flows, but they are not of general applicability. For example, Forbes (1988, 1989) used conformal mapping techniques to study one or two-layer flows over a semi-circular obstacle. Melville & Helfrich (1987), Shen *et al.* (1989) and Shen (1992) look at transcritical flows ($F^2 \approx 1$) over a small sill with very small disturbances to the surface (in single-layer flow) or to the interface (in two-layer flow).

2.1.3 Effects of Friction

The effects of friction on the motion of two-layer flows were first considered by Schijf & Schonfeld (1953), and later by many other researchers in studies of salt water intrusion and exchange flows. Friction, especially interfacial friction, is important in the study of arrested saline wedge problems, see Figure 2.4, since its magnitude determines the shape and the intrusion length of an arrested salt wedge (Grubert 1990). In exchange flows, Pratt (1986) and Bormans & Garrett (1989) showed that when friction is considered, the positions of the controls are shifted, and the flow rate and the interface positions are also changed. Friction was found to reduce the flow rate significantly (Dalziel 1991; Helfrich 1994), bringing the prediction of the flow rate much closer to the observations (Hamblin & Lawrence 1990; Cheung & Lawrence 1991). Anati *et al.* (1977) and Pratt (1986) classified the length of channels according to the relative magnitude of the friction force compared to the momentum force. Several natural channels are considered long channels as the friction force is dominant.

Given its importance, better estimates of the friction are needed. The wall friction can be determined either theoretically (White 1991) or empirically (Henderson 1966). The determination of the interfacial friction is much more difficult. The interfacial friction τ_I can be expressed as $\tau_I = \rho\nu(du/dz) - \rho\overline{u'w'}$, where u is the mean horizontal velocity, while u' and w' are the turbulent fluctuating components of horizontal and vertical velocities. Thus, $\rho\nu(du/dz)$ is the viscous component of τ_I, and $\rho\overline{u'w'}$ is the Reynolds stress, with overbar referring to a time average. The measurement of the interfacial friction, therefore, requires the measurement of the Reynolds stress as well as velocity profiles. Only limited measurements of τ_I have been obtained (Dermissis & Partheniades 1985). Given the difficulty of direct measurement, the interfacial friction is most commonly estimated from the balance of forces (Dermissis & Partheniades 1984). This force balance has been widely used in saline wedge flows with the averaged interfacial friction estimated from the observed wedge shapes, *i.e.*, wedge lengths and wedge interface shapes (Arita & Jirka 1987). Some other methods, such as the one used by Abraham & Eysink (1971) assuming that the shear stress varies linearly with elevation, only apply to particular flow situations.

Different parameterization methods have been suggested by various researchers to predict the interfacial friction factor f_I, $f_I = \tau_I / \frac{1}{2}\rho(\Delta U)^2$, where ΔU is the velocity difference between the upper and lower layer. Arita & Jirka (1987) plotted f_I against the layer Reynolds number Re_i for different layer densimetric Froude numbers, where $Re_i = U_i \cdot R_i / \nu$ with R_i being the hydraulic radius for layer i. Bo Pedersen (1986) proposed that f_I be a function of the layer Reynolds number, channel roughness and hydraulic radius. Dermissis & Partheniades (1984) related the interfacial friction factor with the parameter $Re_1 F_0^2$ for any given density difference, where Re_1 is the Reynolds number for the upper layer, and F_0^2 is the Froude number for the entire channel cross section. Some other studies relate f_I to the interfacial shear layer parameters, such as the shear Reynolds number, $Re = \Delta U \cdot \delta / \nu$, and the bulk Richardson number, $J = g'\delta / (\Delta U)^2$, where δ is the shear layer thickness, see Figure 2.5. Abraham *et al.* (1979) expressed f_I as a function of the shear Reynolds number and the type of flow. Eidenes (1986) linked the interfacial friction factor to the Richardson number. Sherenkov *et al.* (1971) and Grubert (1989) suggested that f_I be a function of the stability number or Keulegan number $K = \theta^{-3} = (\Delta U)^3 / g'\nu$. It can be shown that for one flow condition, the estimated f_I from the above formations varies by one to two orders of magnitude (Cheung & Lawrence 1991). In the present study of exchange flows, f_I will be determined experimentally using the force balance method.

2.2 INTERFACIAL INSTABILITIES IN TWO-LAYER FLOWS

Studies on the stability of incompressible, steady-state (the mean flow), parallel, two-layer stratified flows are reviewed here. The density difference between the two layers is assumed small, and Boussinesq approximation is invoked. The governing equation for an infinitesimal two-dimensional disturbance, of wave number α, $\alpha = 2\pi/\lambda$, (λ is the wave length), and wave speed c, $c = c_r + ic_i$, can be obtained using the normal mode method, with the amplitude of the vertical velocity w expressed as $w = \hat{w}\exp(i\alpha(x - ct))$. For inviscid nondiffusive flows, the governing equation becomes the Taylor-Goldstein equation (Taylor 1931; Goldstein 1931):

$$(U - c)(\hat{w}_{zz} - \alpha^2\hat{w}) + (\frac{N^2}{U - c} - U_{zz})\hat{w}_{zz} = 0, \tag{2.9}$$

where $N = (-\frac{g}{\rho}\frac{d\rho}{dz})^{1/2}$ is the Brunt-Vaisala frequency, ρ and U are the background density and velocity, respectively. The stability of the flow is determined by solving for the wave speed c and the wave number α from the eigenvalues of the governing equation: when c_i is positive, the initial disturbance has an exponential growth rate of αc_i, and a propagating speed of c_r. When viscosity and diffusivity are included, the governing equation is then a sixth-order ordinary differential equation (Koppel 1964).

2.2.1 Linear Stability Theories of Inviscid Non-diffusive Flows

Linear stability of inviscid nondiffusive flows can be studied by solving the Taylor-Goldstein equation for given velocity and density profiles. Kelvin (1871) and Helmholtz (1868) showed that uniform two-layer flows are always unstable for any given velocity difference, as long as the wave number α is sufficiently large. This instability, subsequently named the Kelvin-Helmholtz (K-H) instability, is stationary relative to the mean velocity, and it tends to roll up causing significant mixing. When the velocity profile is piece-wise linear while the density profile is still two-layer discontinuous, see Figure 2.6, Holmboe (1962) found that, besides a small region of K-H instability for a very small bulk Richardson number J, there is also a large unstable region extending to infinite J. In that region, the instabilities are composed of waves protruding into the upper or lower layer, having the same growth rate and propagating in opposite directions, but with the same speed with respect to the mean flow. This symmetric instability is known as the Holmboe instability.

In real flows, the velocity and density profiles are under the influence of viscous diffusion and thermal (or salinity) diffusion, as shown by the heavy curves in Figure 2.5. The ratio R of the shear layer thickness δ and the density layer thickness η, $R = \delta/\eta$, is a function of the Prandtl number, $Pr = \nu/\kappa$, where ν is the kinematic viscosity and κ is the thermal (or salinity) diffusivity, (Smyth *et al.* 1988). They showed that R can be approximated as $\sqrt{Pr}$. Even if R has some other value initially, it will approach $\sqrt{Pr}$ asymptotically on a non-dimensional time scale proportional to the shear Reynolds number. Therefore $R \approx 1$ for thermally stratified air flows where $Pr \approx 1$, and $R >> 1$ for salinity stratified flows where $Pr \approx 700$.

Hazel (1972) studied numerically the effects of the ratio R on interfacial instabilities using hyperbolic-tangent functions for both the velocity and density profiles. Hyperbolic-tangent functions are chosen since they are good approximations to the error functions which result from viscous and density diffusion, and the difference between the hyperbolic-tangent functions and the error functions is small (Hazel 1972). Hazel found that, for $R = 1$, K-H instabilities occur for $J < 0.25$, and flow is stable for any J larger than 0.25. For $R > 2$, however, besides a small region of K-H instability, there is also a region of Holmboe instability which extends to infinitely large J. Later Smyth *et al.* (1988) and Haigh (1995) showed that R must be greater than 2.4 in order for flow to generate Holmboe instabilities. When $R = \infty$, Nishida & Yoshida (1990), using a hyperbolic-tangent velocity profile and two-layer density profile, found that the flow is unstable at large wave numbers.

The effects of R on interfacial instabilities of two-layer stratified flows were studied experimentally. When $R \approx 1$, only K-H instabilities were possible, as was found by Thorpe (1968, 1973) in his experiments where the density interface was allowed to diffuse before the experiments started, and by Scotti & Corcos (1972) and Delisi & Corcos (1973) in the two-layer thermally stratified flow in a wind tunnel where $R \approx 1$. In these experiments, the flow was stabilized when $J > 0.25$. When $R >> 1$ as in salinity stratified flows, Koop & Browand (1979) confirmed that for small J ($J < 0.07$), the most unstable waves were K-H waves, while for large J

($J > 0.07$), only Holmboe waves were visualized. Holmboe instabilities were also observed in other experiments with large J (Browand & Wang 1972; Grubert 1980; Poulequen *et al.* 1994).

Besides the Holmboe instabilities with two symmetric modes, non-symmetric instabilities with two modes of waves having different growth rates and speeds were also observed (Moore & Long 1971; Poulequen *et al.* 1994). The extreme non-symmetric instability occurs when one mode is completely suppressed, leaving only the other observable (Koop & Browand 1979; Lawrence *et al.* 1991; Guez & Lawrence 1995). These are often called one-sided waves. Lawrence *et al.* (1991) explained these one-sided instabilities using non-symmetric flow fields where the density interface is shifted from the center of the shear layer. For non-zero shift ε, $\varepsilon = 2d / \delta$, where d is the shift of the density interface from the shear center, see Figure 2.7, Lawrence *et al.* (1991) showed that the stability boundaries for two modes of instabilities bifurcate. For $\varepsilon > 0$, *i.e.*, the shear center is higher than the density interface, the growth rate of the set of waves protruding into the upper layer and propagating towards right (the positive waves) is increased, while the growth rate of the set of waves protruding into the lower layer and propagating towards left (the negative waves) is decreased or suppressed. The wave number of the fastest growth (or dominant) positive waves decreases while that of the negative wave increases when ε increases. Meanwhile the fastest growth positive waves slow down, whereas that of the negative waves speed up. When the shift is large enough, one set of waves is totally suppressed.

The shift of the density interface relative to the shear center has been confirmed experimentally (Koop & Browand 1979; Yonemitsu 1991; Lawrence *et al.* 1991). A significant positive shift ($\varepsilon \approx 0.5$) is found to be the reason that only the positive component of the Holmboe waves were observed in the experiments of Koop & Browand and Lawrence *et al.* Some other experimental observations might also be due to the shift, such as the one-sided waves observed by Keulegan (1949), and the more dominant positive waves observed by Moore & Long (1971). More recently, Pouliquen *et al.* (1994) found that the shift can also be caused by the surface tension at the interface of two immiscible fluids. By using different combinations of various fluids, the surface tension, and thus the shift, were changed.

Experimental measurements of Holmboe waves were compared to the theoretical predictions by Browand & Wang (1972). They found the instability region of the symmetric Holmboe instabilities agreed well with the prediction of Holmboe (1962). The measured growth rate of instabilities, however, was about ten times smaller than the prediction. Lawrence *et al.* (1991) found that the measured wavelength of the non-symmetric Holmboe waves agreed well with the predictions of their linear stability with the shift considered. The experimental results of Pouliquen *et al.* (1994) for the flows with different shifts are also well explained using the piecewise linear velocity profile and two-layer density profile with shift.

2.2.2 Effects of Viscosity and Diffusivity

It is generally accepted that viscosity has little effect on the conditions at the onset of instability except that it changes the length-scale of the shear layer (Thorpe 1971; Turner 1973). Thus the inviscid theory can be used for stability study, with the effect of viscosity being considered on velocity profiles. Similarly, only nondiffusive flows need to be considered with the effect of diffusion on density profiles properly considered (Maslowe & Thompson 1971). The only likely exceptions are the flows with very low Reynolds number where viscous damping will reduce the growth rate of disturbances, and the flows with very small Prandtl number ($Pr < 0.1$) where the results are different (Gage 1972, 1973; Miller & Gage 1972).

Viscous effects were studied numerically by Nishida & Yashido (1987) and Yonemitsu *et al.* (1996) using two-layer density profile with a hyperbolic-tangent velocity profile. By including viscosity, they found a critical Richardson number existed for Holmboe instabilities, beyond which, instability is impossible and the flow is stabilized. This critical Richardson number was relatively insensitive to variations of the Reynolds number. They also found that waves with larger wave numbers were stabilized when the Reynolds number was decreased.

The instabilities for the flow with viscosity and diffusivity considered were studied by Smyth *et al.* (1988), using hyperbolic-tangent profiles for both the velocity and density profiles. They found that the diffusivity does not qualitatively change the stability characteristics, and there is no significant change in the wave number of the fastest-growing wave at any J. However, diffusion alters the magnitude of the growth rate to a substantial degree. Haigh (1995) furthered this study by allowing the density interface to shift from the shear center. Haigh showed that compared to the piece-wise linear profiles of Lawrence *et al.* (1991), the stability boundaries for the smooth profiles open up; the wave number of the fastest-growing wave becomes larger for $\varepsilon = 0$; for $\varepsilon > 0$, the wave number for positive waves of the fastest-growing wave increased, but that for the negative waves had no noticeable change. It was also found that the difference in growth rate between the positive and negative waves was much larger than that predicted using piece-wise linear profiles, probably due to the difference in velocity profiles.

2.2.3 Effects of Boundaries, Non-linearity and Three-dimensionality

The effects of symmetric boundaries on the flow were studied by Hazel (1972). He found that the waves with small wave numbers are de-stabilized while those with large wave numbers are stabilized. But the effects are small when the boundaries are reasonably far away from the interface (2.5 δ). When the boundaries are very close to the shear center (about 0.6 δ), the flow is stable for all wavelengths. The effects of non-symmetric boundaries were studied by Yonemitsu (1991) by moving the lower boundary closer. The negative waves were found to be significantly affected, while the positive waves were relatively unaffected. Smyth *et al.* (1988) included boundaries in Holmboe's model and found that the transition to Holmboe instabilities starts with smaller J. Similar results were obtained by Haigh (1995), where she also studied the boundary effects on non-symmetric flow field.

Non-linear evolution of Holmboe instabilities was studied numerically by Smyth *et al.* (1988) and Smyth & Peltier (1989) for viscous and diffusive flows using unshifted hyperbolic tangent profiles for both density and velocity. They found Holmboe waves have much longer developing periods. Thus, despite their relatively small growth rates, Holmboe waves can achieve similar magnitudes as K-H waves. Smyth *et al.* also confirmed the prediction of Holmboe (1962) that wave speeds vary when positive and negative waves pass through each other, with the waves speeding up when they approach each other, and slowing down when they pass through each other. Haigh (1995) furthered this study for shifted flows and found that wave speeds increase slightly as non-linear effects become important. Her numerical simulations compared favorably with the experimental observations of both symmetric and non-symmetric Holmboe waves.

The assumption that instabilities are two-dimensional is generally justified since they will normally pass through a distinct two-dimensional state before being dependent on the third spatial coordinate, as shown by Squire (1933) for homogeneous viscous flows. For steady two-dimensional inviscid stratified flows, Yih (1955) extended Squire's theorem and showed that, for each infinitesimal three-dimensional wave, there is a two-dimensional wave having the same growth rate but with larger Richardson number. Since an increase in the Richardson number usually reduces the growth rate of unstable waves, the most unstable disturbances will therefore be two-dimensional. Smyth *et al.* (1988) confirmed that Squire's theorem holds in symmetric, piecewise linear, two-layer flows. However, Smyth & Peltier (1989) found that the fastest-growing Holmboe instability was three-dimensional for sufficiently small Reynolds number and two-dimensional for sufficiently large Reynolds number. When the flow is shifted, Haigh (1995) showed that for $\varepsilon > 0$, the fastest growing (dominant) positive waves can be 2-D, while the negative waves 3-D. The observations of 3-D Holmboe waves were reported by Moore & Long (1971), Koop & Browand (1979), and Sargent & Jirka (1987), but these flows may have initially been two-dimensional with 3-D disturbances being developed later.

In this study, we will assume the Holmboe instabilities are two-dimensional, and the linear theories will be used to compare with the experimental measurements of Holmboe instabilities in exchange flows.

Chapter 3

EXPERIMENTAL APPARATUS AND TECHNIQUES

3.1 EXPERIMENTAL DESIGN AND EXPERIMENTAL SETUP

For steady exchange flows through a channel with a sill, see Figure 2.1 and Figure 3.1, the volumetric flow rate Q is a function of various parameters: the sill height (h_m), the total water depth (H), the channel width (b), the channel length (L), the density of the fluid for both layers (ρ_1 and ρ_2), the gravitational acceleration (g), the viscosity (ν), and thermal diffusivity (κ):

$$Q = f(h_m,\ H,\ L,\ b,\ \rho_1,\ \rho_2,\ g,\ \nu,\ \kappa). \tag{3.1}$$

In Eq. (3.1), the temperatures T_1 and T_2 for the upper and lower layer are omitted since their effects on density, viscosity and diffusivity are already taken into account by incorporating ρ_1, ρ_2, ν and κ as independent variables. Also the difference in the interface levels between two reservoirs will not affect the flow rate for maximal exchange flows, as the flows are controlled by two controls, see Section 2.1.1.

We use the density in the lower layer ρ_2 and the relative density difference $\varepsilon = (\rho_2 - \rho_1)/\rho_2$ instead of ρ_1 and ρ_2, and we further replace g and ε with the reduced gravity g' given $\varepsilon << 1$. Eq. (3.1) can then be simplified by considering only the flow rate per unit width, $q = Q/b$:

$$q = f(h_m, H, L, b, \rho_2, g',\ \nu,\ \kappa). \tag{3.2}$$

Non-dimensionalizing Eq. (3.2) with respect to ρ_2, g' and H, yields

$$q\big/\sqrt{g'H^3} = f(h_m/H, L/H, b/H, Re, Pr), \tag{3.3}$$

where $Re = \sqrt{g'H^3}\big/\nu$ (a characteristic Reynolds number which is different from those defined later) and $Pr = \nu/\kappa$. The number of variables in Eq. (3.3) can be reduced if the total water depth

H, the length of the channel L and the channel width b are fixed in the experiments. This leaves four parameters, h_m, g', Re and Pr, which can be varied to study the exchange flows under various experimental conditions.

In the present study, our emphasis was on examining the effects of h_m and the Reynolds number. Thus, experiments were designed mainly by varying g' and h_m. The change of both g' and h_m will vary the flow velocity in both layers, and thus vary the Reynolds number. Additional experiments were also designed by varying Pr and L/H.

Experiments were conducted in a 370 cm long, 106 cm wide and 30 cm deep tank, see Figure 3.1. The front panel of the tank was made of Plexiglas to enable observation of the flow. The tank was divided into two reservoirs which were connected by a narrow channel of constant width, b = 10 cm. A straight channel with a length of 134 cm (the short channel) was primarily used to study internal hydraulics, whereas a longer (200 cm) channel was used mainly to study interfacial instabilities.

An underwater sill was placed in the left portion of the channel, see Figure 3.1, to study the effects of bottom topography on two-layer flows. The sills were made of a sheet of aluminum, shaped into the form,

$$h(x) = h_m \cos^2(\pi \cdot x / L_s) \qquad \text{for} \quad |x / L_s| \le \tfrac{1}{2}, \tag{3.4}$$

where h is the sill height, h_m is the sill height at its crest, and $L_s = 2\pi\, h_m$ is the sill length. The cosine shape was chosen to ensure low slopes and curvature for a given length of a sill. The size of the sill can be varied by choosing different h_m. The sill was placed with its crest at 31 cm from the left hand end of the channel for the short channel. Thus the length of the channel, L, measured from the sill control to the right hand end of the channel, becomes L = 103 cm.

A series of experiments were conducted in the short channel with a sill of h_m = 8 cm using the reduced gravity g' varying from about 1 to 12 cm/sec^2. Experiments were also conducted using different sizes of sills, (h_m = 0 ~ 12 cm). The salinity stratified flows, formed by dissolving a known amount of salt into the right reservoir to make the water slightly heavier, were mainly used for this study. Additional experiments were conducted using thermally stratified flows and using a longer channel of 200 cm (the long channel). The effects of the Prandtl number were studied using warm and cool water for the upper and lower layer. The long channel experiments were conducted with a sill of h_m = 8 cm, where the sill was placed 25 cm from the left end of the channel, and thus L = 175 cm. The long channel experiments provide a better opportunity to study the effects of channel length, and more importantly, the interfacial instabilities since the change of the flow conditions was much more gradual. A list of the experiments is shown in Table 3.1.

For each experiment, three sets of measurements were sometimes necessary. The first set was needed for the study of internal hydraulics where the instantaneous information on velocity field and interfacial positions along the whole channel are required. The second set was needed for the study of interfacial instabilities, which required the simultaneous wave characteristics and the shift of the density interface from the shear center, and the third set was for the measurements of density profiles.

3.2 FLOW MEASUREMENTS

3.2.1 Velocity Field

Velocity field was obtained by adding tiny neutrally buoyant particles into both the fresh and salt water and following their movements. Pliolite VT-L particles (Goodyear Chemical Co.), with a gravity of 1.026 g/cm^3 and a commercial name of polyvinyltoluene butadiene, were chosen for this study. These particles, a kind of solid white resin, are insoluble in water, exhibit

Table 3.1 List of Experiments

EXP	h_m cm	g' cm/s²	U_1(1) cm/s	U_2(1) cm/s	δ(1) cm	q*(1) (2)	Re(3)	J(4)	T_H(5)	T_s(6)	Repeat (7)
1	8	1.09	2.1	-1.1	4.0	0.110	1123	0.43	18.6	2.5	
2[a]	8	1.56	2.6	-1.3	4.0	0.113±0.003	1368	0.41	15.6	2.1	3
3	8	2.18	3.2	-1.8	4.0	0.119	1754	0.35	13.2	1.6	
4	8	2.34	3.4	-1.9	3.9	0.117±0.003	1813	0.32	12.7	1.5	2
5[b]	8	2.50	3.8	-1.9	4.2	0.123	2100	0.32	12.3	1.5	
6	8	3.12	3.8	-2.0	3.6	0.120	1832	0.33	11.0	1.2	
7	8	6.24	5.7	-3.3	4.1	0.126	3237	0.32	7.8	0.9	
8	8	12.48	8.0	-4.4	4.5	0.123±0.001	4895	0.37	5.5	0.7	2
9[c]	8	1.60	2.7	-1.8	4.4		1737	0.35	15.4	2.0	3
10[d]	0	0.94	2.6	-2.4	4.7	0.189	2061	0.18	20.1	1.9	
11	4.5	12.48				0.153			5.5		
12	6	1.56	2.6	-1.6	3.5	0.141±0.002	1289	0.31	15.6	1.7	2
13	10	2.34	3.0	-1.4	3.7	0.094	1428	0.45	12.7	1.7	

All experiments were conducted in the short channel with L = 103 cm, and total depth H = 28.0 cm, except for Exp. 9 and Exp. 10.

1: U_1, U_2, δ and q^* were measured for maximal exchange flows.
2: $q^* = q/\sqrt{g' H^3}$ is non-dimensional flow rate, where H = 28 cm is used for all experiments.
3: $Re = \Delta U \cdot \delta/\nu$ is the shear Reynolds number for maximal exchange flows.
4: $J = g'\delta/(\Delta U)^2$ is the bulk Richardson number for maximal exchange flows.
5: $T_H = L/\sqrt{g'H}$ is time scale for the study of hydraulics, where L = 103 cm and H = 28 cm.
6: $T_s = \delta/(\frac{1}{2}\Delta U)$ is time scale for the study of interfacial stability, where δ and ΔU are obtained from maximal exchange flows.
7: Number of repetitions of experiments.
a: Additional experiments were conducted to measure the velocity field around the sill.
b: Cool (16 °C) and warm (27 °C) water was used to create the density difference.
c: Experiments were conducted in the long channel with L = 175 cm and H = 28.5 cm.
d: Experiment was conducted without sill, thus L = 134 cm.

a high degree of reflectivity, and can be ground to yield sizes from 10 μm to 200 μm. Particles with a size of 100 to 200 μm were used for our experiments since they were clearly visible, but still had a relatively small settling velocity. The settling velocity w_p of a spherical particle of diameter d_p can be calculated assuming that Stokes' law applies:

$$w_p = (g d_p^2 / 18 \nu_F)(\rho_p - \rho_F)/\rho_F, \tag{3.5}$$

where ρ_p is the particle density, ρ_F and ν_F are the density and kinematic viscosity of the fluid, g is the gravitational acceleration. For a particle with d_p from 100 μm to 200 μm, w_p changes from 0.01 to 0.05 cm/sec. As a result, the Reynolds number $Re_p = w_p\, d_p/\nu$ ranges from 0.01 to 0.1. For flows having a velocity of several centimeters per second, this settling velocity does not affect velocity measurements. Thus these particles are suitable for visualizing flow velocity field. For an experiment lasting several minutes, the use of these particles as neutral buoyancy particles was satisfactory.

A sheet of light was used to illuminate the particles within the channel. The light sheet was obtained by using a scanner mirror to split the laser beam from a 4 W argon laser (Stabilite 2017 by Spectra-Physics). The light was then reflected by a large mirror to illuminate the flow from the top, see Figure 3.2. The scanner mirror was controlled by a function generator (Kenwood Function Generator) through a scanner drive (Ax-200 by General Scanning Inc.). The mirror was scanning at a frequency of about 300 Hz, fast enough to enable video recording which has a frequency of 30 Hz.

The movements of the particles were recorded using a low-noise CCD camera (Cohu High Performance CCD camera with a lens of 1:2.5/18-108) and the images were stored in a Hi 8 mm video camera (Sony CCD F701). The use of Hi 8 camera enabled high quality and high resolution images to be recorded. Those video images were captured by a Macintosh IIci computer using a frame grabber board (QuickCapture DT 2255 by Data Translation), controlled by the software IMAGE version 1.50 (National Institute of Health). The captured images were analyzed using IMAGE or downloaded to a Sun Sparc workstation (Sparc 2) for further analysis using PV-Wave (by Visual Numerics Inc.) or FORTRAN codes.

Velocity fields were obtained by following particle "patterns" using a spatial cross-correlation between successive images, (Stevens & Coates 1994). Pairs of images were captured at a given time interval, see Figure 3.3. A grid of nodes, at which velocities were required, was set up on the first image. A window of certain size was extracted, centered on each node in turn. The second image was then searched for a similar window of the same size that was maximally spatially correlated to the first window. The result was a set of displacement vectors regularly spaced over the image describing the "instantaneous" velocity field. Post processing of the data was generally necessary and a multi-pass filter was used to remove erroneous vectors. The technique provided an instantaneous velocity field and was non-intrusive, ideal for this study. Since this technique is to follow the rigid motion of the "patterns", considerable error may be possible in the interfacial shear region where there is significant straining or rotation. Thus, in applying this technique, the choosing of the time interval and window size is crucial to reduce the errors.

3.2.2 Density Profiles

Density profiles were obtained using a Micro-scale Conductivity Temperature Instrument (Model 125, Precision Measurement Engineering). The probe carriage system was driven by a stepper motor, which was linked to a stepper motor controller. The entire profiling and sampling process was controlled by a computer. The computer signaled the stepper motor controller to set the carriage in motion. At the same time, the computer sampled the amplified output of the conductivity probe, and converted the analog data to a 12-bit binary number, using an A/D board (DAS8 from Strawberry Tree Inc).

To ensure that the measurements of the conductivity of both the upper and lower layer were within the linear range of the conductivity probe (5 to 800 mS/cm), salt was added into both reservoirs, with extra amount added into the right one to obtain the desired density difference. Within its linear range, the output voltage of the conductivity probe V_0 can be expressed as:

$$V_0 = G \times K + V_{off}, \tag{3.6}$$

where V_{off} is the calibration voltage, K is the conductivity, and G is the constant coefficient which is determined through the calibration using the standard solutions of 0.05 and 0.10 mol/L KCl. For the solutions at temperature other than 25 °C, the effects of the temperature should be considered (Standard Methods 1989).

The probe sampled only on downward traverses, as it entrained a small amount of denser fluid with it when it was pulled up. The probe was traversed slowly (0.5 cm/sec) to minimize disturbances, and to increase the spatial resolution. The measured voltage data was converted to conductivity using Eq. (3.5). The conductivity data were further converted to salinity and then to density, with the temperature of the fluid also being considered. The formulae used for these conversions were found in Head (1983) for salt water of NaCl.

3.2.3 Simultaneous Measurements of Velocity Field and Density Interface

The density interface of the two layers was visualized by dissolving a dye into the lower layer and shining a sheet of laser light from the top, see Figure 3.2. Either sodium fluorocein dye (green) or Rhodamine WT dye (orange) was used. A Super-VHS camera (Hitachi VMS 7200A) was used to record the interface position. The video images were grabbed, downloaded and processed in a similar way as the video images of particle movements, see Section 3.3.1.

Locating the density interface between the two layers was relatively straightforward as the dyed lower layer was much brighter than the transparent upper layer. The interface position was defined as the location with maximum gradient of light intensity. However, in detecting the interface, some noise had to be considered: interfacial instabilities could cause interfacial waves to roll over, or eject fluid from the lower layer. To prevent mistaking these waves or plumes for the interface, the consistency of the gradient of light intensity was checked. The measurements were also post-processed using a multi-pass filter to remove the erroneous points. The above techniques were very successful for most of the experiments. However, when the interface was very turbulent, the accurate determination of the interface position was difficult.

The above interface is, in fact, the dye interface between the two layers. Since the density layer thickness is very thin, less than a couple millimeters, and the diffusion of the dye and salt is similar, the difference between the dye interface and the density interface is negligible and the dye interface can be used to represent the density interface (Merzkirch 1987).

Given that simultaneous measurements of velocity field and interface position were needed for the hydraulic studies, both dye and particles were added into the flow. Sufficient dye concentration in the lower layer was required to have enough light contrast in order to detect the interface automatically. This, however, would make the particles in the lower layer hardly visible, thus make the particle tracking very difficult. To overcome this difficulty, Rhodamin WT dye (orange) was selected and filters were used. A green or blue filter was used to visualize the particles which reflect the laser light of blue/green giving a wave length of 500 nm. An orange filter was used to visualize the lower layer dyed with Rhodamin WT. With the help of these filters, high quality images of particles and dye were recorded onto separate video tapes. Usually one video camera was focused on the middle region of the channel recording the movements of particles, while the other recording the interface position throughout the whole channel. Thus instantaneous and simultaneous velocity and interface information was obtained.

For the study of the interfacial instabilities, the shift of the density interface from the shear center needs to be measured. Instead of recording particles and dye onto two video tapes, they were recorded onto the same video image to avoid possible errors resulted in dealing with two video images. A lower dye concentration was used in order to visualize particles. This made dye interface more difficult to detect. This difficulty was partially compensated by increasing the spatial resolution by recording images in the middle region of the channel.

3.2.4 Experimental Preparation

Experiments were conducted in a dark room with the channel illuminated by a sheet of laser light from the top. The channel and the sill were shaped according to experimental requirements. The tank was filled with fresh water to the specified depth, and a gate was inserted into the middle of the channel to separate the tank into two reservoirs. Known amount of salt was added into the reservoirs to form the density difference. The water in the right reservoir is made slightly heavier, so that the upper layer is from left to right, while the lower layer from right to left. Selected dye was also dissolved into the right reservoir. Pliolite particles were added and mixed into both reservoirs. The water was stirred for several minutes to make sure it was well mixed, and the temperature of the water was measured. The recording facilities were set up and physical scales were recorded to calibrate video images. After the water became quiescent, the experiments were started by pulling out the gate.

3.3 ERROR ANALYSIS

Errors in velocity determination and flow rate calculation

The images used for the velocity analysis covered an area of 40 cm (horizontal) x 30 cm (vertical). Given that each image had a size of 640 x 480 pixels, pixels had a resolution of about 0.06 cm. The time interval between two images was chosen to ensure that particles had an averaged travel distance of about 20 pixels. With a possible error of ± 0.5 pixel in determining the traveling distance, a relative error of about 3 % in velocity determination is possible (Stevens & Coates 1994). In practice, three or four neighboring velocity profiles (about 0.6 cm apart for a grid of 10 pixel) were averaged. Thus the relative error was reduced. Other minor errors include those due to the relatively low spatial resolution of velocity fields, (about 0.6 cm or 10 pixels), and the erroneous velocity vectors due to the quality of images. Considering that our experiments were relatively steady and reasonably two-dimensional, these errors should not be significant (less than 1 %). Therefore an estimate of the possible error in velocity determination is about 4 %.

Estimating the velocity gradient in the interfacial layer is also important. Due to the smaller travel distances of the particles in the interfacial region (from 0 to 10 pixels), the relative error in velocity determination could be as large as 10 %. Considering the relative low accuracy in determining the velocity in the interfacial region due to the deformation of the particle "patterns", the errors in estimating velocity gradient could be about 15 %.

The flow rate was obtained by integrating the upper and lower layer velocity profiles. Therefore, besides the errors from the velocity calculation, the errors in flow rate could also come from the determination of the surface and bottom positions. The accurate determination of the surface and bottom was difficult, since they were shown as strips of a thickness of about 2 pixels in video images. This was caused by the finite thickness of the light sheet and the fact that images were taken with an angle to both the surface and the bottom. Besides, the images were also slightly distorted and the surface and bottom positions slight curved. As a result, it was possible to have 1 - 2 pixel error in reading the position of the surface and the bottom, thus resulting in an error of 1 - 2 % in the flow rate calculation. Considering the errors in velocity measurements, an error of about 5 % is possible in the flow rate measurements. This error was reduced by multiple averaging the flow rate of the upper and lower layers.

Errors in determining density layer thickness and interface positions

In estimating the density layer thickness, one significant error could be caused by the fluctuations of the interface position due to interfacial waves. When the interface was rising, it took the probe less time to transverse through the interface region, while it took longer when the interface was falling. The effects of this interface fluctuation were estimated by taking multiple profiles and estimating the standard deviation of the density layer thickness. Errors could also come from the spatial resolution of the conductivity measurements. The accuracy of the positioning of the probe was controlled to 0.01 cm. The spatial resolution of the measurements when the probe moving at 0.5 cm/sec and data sampling at 20 Hz was 0.025 cm. The accuracy of the speed measurement was about 0.02 cm/sec. The spatial resolution of the probe was about 0.05 cm. Thus a combined error was about 0.1 cm in conductivity measurement.

The errors in determination of interface position came mainly from the coarse resolution of the video images. For the hydraulic studies, the video images covered the whole channel of 134 cm. Thus the image had horizontal and vertical resolutions of about 0.2 cm/pixel for video images of 640 x 480 pixels. With an error of 1 - 2 pixels in interface detection, the error thus could be 0.2 - 0.4 cm. Errors from the distortion of the video images and the difference between the dye interface and the density interface were minor, less than 0.1 cm. Thus, an error of about 0.4 cm in the determination of interfacial positions was possible. Similarly, the error was reduced through temporal and spatial averaging.

Other minor errors

For experiments with a sill of h_m = 8.0 cm, an error of up to 0.1 cm is possible in the sill height h_m. Errors could also be caused by the slight distortion of the video images. But these errors are minor since the video camera is placed relatively far (about 3 m) away from the flume, see Figure 3.2. Furthermore, the image positions are calibrated against a physical scale placed within the light sheet. The steep gradient of the refractive index due to the density interface, on the other hand, will not affect the measurements outside the interface region. This is because the camera is looking at the particles horizontally while the flume is illuminated vertically by the light sheet, see Figure 3.2. The region of the density interface is very thin (about 0.3 cm, see Section 4.3), and the flow within the region has very small velocity. Thus the error on the flow rate is small.

Chapter 4

EVOLUTION OF FLOWS

4.1 OVERVIEW OF FLOW EVOLUTION

Experiments on exchange flows over a sill in a channel of constant width were conducted. The mean flow evolved through four regimes after experiments were started by pulling out the gate in the middle of the channel and allowing fluids to exchange:

Regime A (Unsteady start-up flow): upon removal of the gate, two gravity currents developed, (Figure 4.1a), and gradually an unsteady exchange flow was established (Figure 4.1b). During this start-up period, significant mixing occurred. The mixed fluid was gradually advected into the supply reservoirs. The sill control was established first, and the exit control was established at a later time.

Regime B (Maximal exchange): the maximal exchange flow with both the sill control and the exit control (Figure 4.1c) was steady with constant flow rate and interface position. As the experiments proceeded, the interface level in the right hand reservoir (y_R) gradually decreased, while that at the left reservoir (y_L) gradually increased.

Regime C (Submaximal exchange): when the exit control became submerged due to the decrease of y_R, the flow was then submaximal (Figure 4.1d). This flow depended on the remaining sill control and y_R. Due to the decrease of y_R, the interface level along the channel, as well as the flow rate, decreased. This submaximal exchange had a smaller flow rate, and could be regarded as quasi-steady due to the large reservoir size.

Regime D (Uncontrolled flow): eventually, the sill control was also submerged due to the rising of the interface level in the left reservoir. The flow was then uncontrolled, and the flow rate and interface position depended solely on the interface level at the right and left reservoirs. The actual flow at this stage was quite complicated: significant mixing occurred downstream of the sill. Some of the mixed fluid was brought to the middle region of the channel by advection of the upper layer, and a three-layer density structure was formed (Figure 4.1e).

Evolution of the mean flow

The evolution of the mean flow can be described quantitatively by a non-dimensional time, $t^* = t/T_H$, where the time scale T_H is defined as

$$T_H = L/\sqrt{g'H}, \tag{4.1}$$

with L and H being the length and total depth of the channel. T_H varied from 5.5 s (Exps. 8 & 11) to 20.1 s (Exp. 10), see Table 3.1. This time scale characterizes the time needed for the internal disturbances to pass through the channel, and by non-dimensionalizing the time, the experiments with the same setup but different g' can be compared.

The flow evolution is illustrated using Exp. 2 where T_H = 15.6 s, see Figure 4.2(a). This evolution is characterized using the mean properties of the flow, the flow rate, $q^* = q/\sqrt{g'H^3}$, and the interface position at the right hand exit, $y_e^* = y_e/H$. The short term fluctuations due to the interfacial instabilities were filtered. In Regime A, y_e^* decreased from its initial value of 1.0, once the fresh-water gravity current reached the right reservoir. At $t^* \approx 5$, the exit control was established and the flow was in Regime B (maximal exchange). In this regime, y_e^* and the flow rate q^* remained constant. Gradually, the interface level at the right reservoir could not support the exit control, and the flow was in Regime C (submaximal exchange). This happened at $t^* \approx 22$. During Regime C, y_e^* and q^* gradually decreased due to the lowering of the interface level at the right reservoir. Regime C lasted until $t^* \approx 60$ when the sill control was also submerged by the rising of the interface level at the left reservoir.

Evolution of interfacial disturbances

During the experimental process, the interfacial layer in the middle region of the channel evolved through three phases: Phase I with no Holmboe instabilities being generated, Phase II with Holmboe instabilities being generated locally, and Phase III with Holmboe waves decaying and the interfacial layer stabilizing (see Figure 4.2b). This process can be described quantitatively using the standard deviation of wave amplitude, σ_y , for the Holmboe waves measured in the middle region of the channel.

$$\sigma_y = \{\int_{x_1}^{x_2} (y - \overline{y})^2 dx \Big/ (x_2 - x_1)\}^{\frac{1}{2}}, \tag{4.2}$$

where y and $\overline{y}$ are the interface and mean interface position respectively, x_1 and x_2 are the starting and ending points of the region of interest. The change of σ_y against time was plotted in Figure 4.2(b) for Exp. 2 where $x_1 = 0.5\ L$ and $x_2 = 0.8\ L$ were chosen. Phase I lasted until t^* $\approx$ 10 after the experiment started. Phase II with Holmboe instabilities generated locally lasted for a quite long period from $t^* \approx 10$ to 50. Note that Holmboe instabilities started to be generated at $t^* \approx 10$ instead of $t^* \approx 5$ when the flow became maximal exchange. Phase III lasted for a quite long period covering the rest of the maximal and most of the submaximal flows. The reasons for the evolution of the interfacial instabilities will be detailed later in this chapter.

In the present study, we will use maximal exchange flows (Regime B) to study the extended internal hydraulic theory incorporating the effects of friction and streamline curvature. We will use Phase II of the experiments, which covers part of maximal and submaximal exchange, to look at interfacial instabilities. The conditions for maximal exchange are studied in Section 4.2, and the evolution of the interfacial layer and interfacial instabilities are presented in Section 4.3 and Section 4.4 respectively.

4.2 CONDITIONS FOR MAXIMAL EXCHANGE FLOWS

Maximal exchange flows with the sill and exit controls can be maintained for a wide range of reservoir conditions, but when the interface level at the right reservoir, y_R, is low enough (or that at the left reservoir, y_L, is high enough), the exit (or the sill) control is submerged. Here the conditions to maintain the maximal exchange flows are studied.

Internal energy at the right hand exit and the right reservoir

When there are no energy losses, the layer energy (Bernoulli constant) is conserved for both the upper and lower layer between the exit and the right reservoir. Since there are energy losses when the upper layer flows out of the channel and when the lower layer enters the channel, we then have the following relations for the upper and lower layer:

$$E_{1e} - E_{1R} = \tfrac{1}{2}\alpha_1 \rho_1 U_{1e}^2 + \Delta E_1, \tag{4.3}$$

and

$$E_{2R} - E_{2e} = \tfrac{1}{2}\alpha_2 \rho_2 U_{2e}^2 + \Delta E_2, \tag{4.4}$$

where subscripts R and e represent the conditions at the right hand reservoir and the right hand exit of the channel, respectively. α_1 and α_2 are the energy loss coefficients due to the exit (for the upper layer) and entrance (for the lower layer), respectively. ΔE_1 and ΔE_2 are the additional energy losses due to internal hydraulic jump and/or turbulent mixing.

Subtracting Eq. (4.3) from Eq. (4.4), and using Eq. (2.4), we obtain a relationship for the internal energy:

$$E_R - E_e = \alpha_1 \frac{U_{1e}^2}{2g'} + \alpha_2 \frac{U_{2e}^2}{2g'} + \Delta E, \tag{4.5}$$

where $\Delta E = (\Delta E_1 + \Delta E_2)/(\rho_2 - \rho_1)g$ is the additional loss of internal energy.

Equation (4.5) relates the internal energy in the right reservoir and that at the right hand exit. Without energy losses, i.e., $\alpha_1 = \alpha_2 = 0$, and $\Delta E = 0$, the internal energy is conserved. When there are energy losses, E_R is then larger than E_e. In most cases, E_R is determined by the reservoir conditions, while E_e is determined by the control conditions for maximal exchange flows, ΔE is then determined from the difference between E_R and E_e. ΔE is needed to dissipate the extra energy available in the reservoir beyond that needed to drive the exchange flow. Therefore the minimum E_R required for the exchange flow will have $\Delta E = 0$.

Conditions for maximal exchange flows

Using Eq. (2.5), Eq. (4.5) relates the interface position between the reservoir and the exit, y_R and y_e, considering the flow velocities in the right reservoir are negligibly small,

$$y_R - y_e = (\alpha_1 - 1)\frac{U_{1e}^2}{2g'} + (\alpha_2 + 1)\frac{U_{2e}^2}{2g'} + \Delta E. \tag{4.6}$$

Equations (4.5) and (4.6) are applicable to both maximal exchange flows and sub-maximal exchange flows. For the exchange flows in our experiments, $\alpha_1 \approx 1.0$ and $\alpha_2 \approx 0.5$ since the channel has a sharp end (Henderson 1966). The minimum y_R needed for maximal exchange flows can be obtained from Eq. (4.6) with $\Delta E = 0$:

$$(y_R)_{min} = y_e^c + (1.5)\frac{(U_{2e}^c)^2}{2g'}, \tag{4.7}$$

where superscript c denotes that the parameters are for maximal exchange flows.

Equation (4.7) shows that $(y_R)_{min}$ needs to be higher than y_e^c when the exit loss due to the channel sharp end is considered. For the exchange flow studied here, $y_1 \approx \frac{1}{3}y_2$ thus $F_1^2 \approx 1$ while $F_2^2 \approx 0$. This gives $(y_R)_{min} \approx y_e^c$. Armi (1986) and Farmer & Armi (1986) studied the reservoir conditions neglecting the energy loss. Without energy losses and knowing that $U_{2e}^c \approx 0$, Eq. (4.6) becomes

$$(y_R)_{min} - y_e^c \approx -\frac{(U_{1e}^c)^2}{2g'} \approx -\tfrac{1}{2} y_1^c, \tag{4.8}$$

where $y_1^c = H - y_e^c$, with H being the total depth. Considering that the energy loss is usually significant and cannot be neglected, using $(y_R)_{min}$ from Eq. (4.8) significantly under-estimates the required $(y_R)_{min}$ for maximal exchange flows. This is especially true for our experiments using a sharp end channel.

The condition to maintain the sill control is much easier to determine:

$$(y_L)_{max} = y_s^c, \tag{4.9}$$

where y_s^c is the interface height at the sill crest for maximal exchange flows. When $y_L \leq (y_L)_{max}$, the sill control is formed, and a hydraulic jump occurs within the channel. But when $y_L > (y_L)_{max}$, the sill control is then submerged. Therefore, the reservoir conditions to maintain maximal exchange flows with the exit and sill controls are

$$y_R \geq (y_R)_{min} \quad \text{and} \quad y_L \leq (y_L)_{max}. \tag{4.10}$$

When $y_R < (y_R)_{min}$ (or $y_L > (y_L)_{max}$), the exit (or sill) control is submerged with $G^2 < 1$. On the other hand, when the above conditions are satisfied, the flow must be maximal exchange with both the exit and sill controls.

For our experimental tank where both reservoirs are of approximately same size and $q_1 = q_2$, the interface level in the right reservoir drops at the same speed as that in the left reservoir rises. Given that $1 - (y_R)_{min} < (y_L)_{max}$, the exit control is invariably submerged first. Therefore, after a period of maximal exchange, the flow becomes submaximal exchange with the sill control. Submaximal flows are determined by both the sill control and the interface level in the right reservoir.

4.3 EVOLUTION OF INTERFACIAL LAYERS

In order to understand the generation and propagation of the Holmboe instabilities, the interfacial shear and density profiles were measured. Their changes with time and along the channel were also studied.

4.3.1 Interfacial Shear and Density Layer

Typical measurements of the mean velocity and density profiles are shown in Figure 4.3 for Exp. 2 at $t^* \approx 16$ (about 4 minutes). The mean velocity profile was obtained by averaging several neighboring velocity profiles both in time and space. This averaging is needed since the velocity field could be affected by local interfacial instabilities. The density profile was measured using a conductivity probe. Both the velocity and density were relatively uniform in the upper and lower layer, except in the interfacial region where they changed sharply.

The measured velocity profile compares very well with a hyperbolic tangent function, similar to other experimental measurements of two-layer stratified flows, see, for example, Yonemitsu (1991). In Exp. 2, the velocity difference $\Delta U \equiv |U_1 - U_2| \approx 3.8$ cm/sec and the shear layer thickness $\delta \equiv \Delta U/(du/dz)_{\max} \approx 3.5$ cm.

Similarly, the thickness of the density layer η was obtained from the maximum density gradient and the density difference. The measurements of η were affected by the interface fluctuations, with η smaller (or larger) than the real thickness when the probe and the interface were approaching (or moving away from) each other. Thus estimates of η were obtained by averaging the measurements from 10 profiles. The measurements of η were also affected by the resolution of the probe. Given the probe resolution of 0.1 cm, the real density layer thickness was slightly smaller than the measurement of $\eta \approx 0.3$ cm. Nevertheless, this η was more than 10 times smaller than the shear layer thickness, δ.

The layer velocities U_1 and U_2 used for instability study were obtained by fitting the measured velocity profiles with hyperbolic tangent functions using least square method. The obtained U_1 and U_2, measured at $x = 0.4\ L$, were plotted against time in Figure 4.4 for Exp. 2. Due to the existence of the sill, the flow was asymmetric, see Figure 4.1c, and there was a non-zero mean velocity $\overline{U}$, $\overline{U} = \frac{1}{2}(U_1 + U_2)$. This mean velocity gradually decreased with time when the flow became submaximal.

The shear layer thickness, δ, did not change significantly with time during the experiment even though ΔU decreased, as the decrease in the maximum velocity gradient partially compensated for the decrease in ΔU. The density layer thickness η was initially large, due to the significant interfacial mixing caused by the disturbances at the start of the experiment. The mixed fluid was then gradually swept downstream in both the upper and lower layers, and the density layer was sharpened to $\eta \approx 0.3$ cm at $t^* \approx 10$, which was much later than the establishment of the maximal exchange flow at $t^* \approx 5$. The density layer remained thin for the rest of the experiment. The ratio of the shear layer thickness to the density layer thickness R, $R = \delta/\eta$, was initially small, $R \approx 2$, and then increased to $R \approx 10$ - 15 at $t^* \approx 10$. The large R in salinity stratified flows is caused by the fact that the diffusion of salt, κ, is much smaller than that of the velocity, ν, with Prandtl number $Pr = \nu/\kappa \approx 700$. This large Pr leads to a large R, as is shown by Smyth *et al.* (1988) that $R \to \sqrt{Pr}$. The measurement of R is also comparable to other studies using salinity stratified flows, for example, $R \approx 15$ by Koop & Browand (1979). The density layer thickness for thermally stratified flows, however, can be different due to a significantly different Prandtl number.

The shear Reynolds number, $Re = \Delta U \cdot \delta/\nu$, and the bulk Richardson number J, $J = g'\delta/(\Delta U)^2$, were also plotted in Figure 4.4. The Richardson number was relatively constant when the flow was maximal exchange ($5 \le t^* \le 22$) with $J \approx 0.4$. It then increased with time as the flow velocity decreased in the submaximal exchange. The shear Reynolds number, after remaining relatively constant in the maximal exchange, decreased from about 1500 during the experimental process.

The density interface (the point with the maximum density gradient) was shifted from the center of the shear layer. The amount of the shift has significant effects on the generation and propagation of Holmboe waves. The amount of the shift, d, (see Figure 2.7), in the middle region was measured for two experiments: Exp. 2 (the short channel) and Exp. 9 (the long channel), and the averaged non-dimensional shift ε, $\varepsilon = 2d/\delta$, was plotted against time in Figure 4.5. For both experiments, the shift was large initially, being about - 0.25, with the negative sign corresponding to the shear center lower than the density interface. It then decreased to zero. The shift for Exp. 9 decreased much faster with $\varepsilon \approx 0$ at $t^* \approx 40$ (10 minutes), while that for Exp. 2 remained relatively constant before it finally approached zero at $t^* \approx 60$ (15 minutes).

4.3.2 Change of Flow Conditions along the Channel

In exchange flows over a sill, the flow conditions change along the channel. The Richardson number J increased from the sill crest towards the middle of the channel for Exp. 2, (see Figure 4.6), mainly due to the decrease in ΔU. It then remained quite constant in the region between $x = 0.4 - 0.7\ L$. At a given location, J was relatively constant during the maximal exchange stage, and it increased with time when the flow was submaximal. The change of J with time was small in the sill region, with J increasing slightly from about 0.2 to 0.4 at $x = 0.2\ L$, while J increased from 0.4 to 1.0 in the middle of the channel ($x = 0.5\ L$) during the same period.

The mean velocity of the flow, $\overline{U}$, also changed along the channel, Figure 4.7. $\overline{U}$ was negative in the sill region due to the much larger lower layer velocity. It then increased with x since the upper layer velocity increased while the lower layer velocity decreased due to the rise of the interface position. In the right portion of the channel, the mean velocity is always positive.

The propagation of interfacial waves was affected by the mean velocity $\overline{U}$. The waves have a propagating speed of $c_r^{\pm}+\overline{U}$ to a fixed observer, where $c_r^{\pm}$ is the speed of waves with respect to the mean velocity. According to the propagation of the negative waves, the channel can be divided into three regions: the sill region (x = 0 - 0.3 L), the middle region (0.3 - 0.8 L), and the exit region (0.8 - 1.0 L), see Figure 4.7. In the sill region, the negative waves propagate only to the left since $c_r^{-}+\overline{U}<0$. In the exit region, the negative waves are prevented from propagating towards left to the middle region due to the large $\overline{U}$ which gives $c_r^{-}+\overline{U}>0$. In the middle region, the locally generated negative waves can propagate towards both the sill and exit region. Therefore, the mean velocity prevents the negative waves from propagating into the middle region from the sill or exit region, thus the negative waves in the middle region can only be generated locally. All the positive waves, however, propagate towards right, given that $c_r^{+}+\overline{U}>0$.

This study is focused on the Holmboe instabilities observed in the middle region, where the flow conditions varied gradually with location and the flow was relatively parallel, given the much smaller interface slope. In the sill and the exit region, the flow conditions change dramatically and are quite complicated: the flow has significant acceleration with x, and is no longer parallel.

4.4 GENERATION AND PROPAGATION OF INTERFACIAL WAVES

At the interface of exchange flows, both Kelvin-Helmholtz (K-H) instabilities and Holmboe instabilities, were observed, see Figure 4.8(a). To the left of the sill crest, K-H instabilities were observed since the shear was strong due to the large flow velocity of the lower layer. These K-H waves had zero propagating speed with respect to the mean flow, and thus were washed down the sill due to the left-moving mean velocity. In the middle of the channel (the right part of the photo), Holmboe instabilities were observed since the shear was weaker. A sequence of photos showing the propagation of Holmboe instabilities in Exp. 9 is shown in Figure 4.8(b). Two sets of Holmboe waves were observed, with one set cusping into the upper layer and moving from left to right with respect to the mean velocity (the positive waves) and the other cusping into the lower layer and moving from right to left (the negative waves). The positive and negative waves were moving at approximately the same speed with respect to the positive mean velocity.

Holmboe instabilities are important since they require less shear, and thus might be more common in nature. However, despite recent advances in theoretical and numerical studies, better experimental realizations of Holmboe instabilities have been limited and the conditions for the instabilities poorly understood. To improve our understanding, Holmboe instabilities were studied experimentally using both the short channel and the long channel with a sill of h_m = 8.0 cm. The short channel provided an opportunity to study the evolution of interfacial instabilities along the channel, while the long channel enabled better wave development and better wave visualization by having a more gradual change of flow conditions along the channel.

The development of interfacial waves was studied using wave characteristic plots. A time sequence of the interface position was first obtained. The development of interfacial waves was then shown by displaying these interface positions in an x - t characteristic plot, similar to these used in open channel flows (Henderson 1966). A typical wave characteristics plot for Exp. 9 was shown in Figure 4.9. Figure 4.9 was constructed by stacking the obtained interface positions along the channel as rows. Each strip contained 480 such rows, covering the change of the interface positions in 4 minutes The light intensity within each row represents the relative height of the interfacial position, with the bright and dark points representing higher and lower elevations, respectively. Thus, we see the characteristics for the movements of the upward cusps (positive waves) and movements of the downward cusps (negative waves) as oblique bands of light and dark. In order to obtain better visualization of the interfacial waves, the mean interface position was removed in Figure 4.9 using a simple bi-linear surface.

Given that the measured bulk Richardson number J was larger than 0.2 in both the sill and the middle region (see Figure 4.4), the flow was always stable to K-H instabilities, and only Holmboe waves could be generated (Lawrence *et al.* 1991). The positive waves were generated in the sill region and started propagating towards the right at $t^* \approx 5$ soon after the flow became maximal exchange, while the flow in the middle region was stable, (Figure 4.9). This is because the density layer thickness was quite large in the middle region, with the measured R being about 2. Thus the flow was stable to Holmboe waves (Haigh 1995). In the sill region, however, R was increased much faster by the large shear stress. At $t^* \approx 12$, the density layer in the middle region became very thin, with $R \approx 10$ - 15, while $J \approx 0.4$ and $Re \approx 1500$. Holmboe instabilities were generated locally, and the flow was in Phase II. The initial generation of Holmboe instabilities in the middle of the channel was seen as the sudden generation of the negative waves. The positive wave originated at the sill region, and propagated through the middle region without significant growth. The difference in the growth rate between the positive and negative waves was due to the large negative shift (Figure 4.5). The positive waves propagated much faster, while the negative waves propagated much slower to a fixed observer, given $\overline{U} > 0$. To a fixed observer, the wave speed and direction of the negative waves could change, due to the change of mean velocity $\overline{U}$ with time and location. When $\overline{U}$ was large, so that $c_r^- + \overline{U} > 0$, the negative waves were seen as propagating towards the right.

When t^* increased from 16 to 32, the shift remained relatively constant, $\varepsilon \approx -0.2$, (Figure 4.5), the growth rate of the positive waves was small compared with that of the negative waves. The positive waves from the sill region grew slowly during their propagation in the middle region. The observed positive waves were dependent on their initial characteristics as well as the local flow conditions. The positive waves were then seen as irregular and messy. The negative waves, on the other hand, were seen as quite regular (Figure 4.9). This transition period ended when the shift decreased and the positive waves had sufficient growth rate.

After $t^* =$ 32, the shift in the middle region gradually decreased to zero, thus the growth rate of positive waves increased. Both the positive and negative waves had the same growth rate and grew to an approximately equal amplitude. The positive waves achieved their maximal amplitude, and the symmetric Holmboe waves were observed in the middle region, with waves becoming regularly spaced. The wave speeds were stable, and both the positive and negative waves traveling at about the same speed relative to the mean flow.

Later, after about $t^* =$ 48, the shear decreased rapidly as ΔU and the Richardson number increased. Also the viscous force increased as the shear Reynolds number decreased in the submaximal regime. The wave length became short, and the wave amplitude became much smaller. Finally, at about $t^* =$ 52, when $J \approx 0.8$ and $Re \approx 1300$, the shear was not sufficient to generate the instabilities, and the viscous forces took over. The flow was in Phase III. The waves gradually died down and the interface was stabilized.

It has been stated that in the middle region the negative waves were locally generated, while the positive waves originated in the sill region. A direct confirmation of this was represented in Figure 4.10, where the propagation of the waves along the whole channel was shown. It is seen that most positive waves in the middle region could be traced back to the sill region. These positive waves propagated into the middle region and were little affected by the local conditions during their propagation. The negative waves, however, were generated in the middle region of the channel and propagated in both upstream and downstream depending on the mean flow.

Chapter 5

EFFECTS OF CURVATURE IN LAYERED FLOWS

Although hydraulic theory generally assumes hydrostatic pressure distribution, there are circumstances when the assumption should not be made. Non-hydrostatic pressure are clearly importance in flows over obstacles with relatively large curvature (Dressler 1978; Naghdi & Vongsarnpigoon 1986; Sivakumaran *et al.* 1983). However, Lawrence (1993) has shown that there is an important regime of two-layer flow over an obstacle in which non-hydrostatic pressures cannot be ignored even if the obstacle does not have large curvature. In this chapter, hydraulic theory is extended to incorporate the non-hydrostatic pressure caused by a smooth two-dimensional bottom sill. The effects of friction will be considered in Chapter 6. In Section 1, hydraulic theory is extended to incorporate the effect of the curvature for a general layer of flow in a multi-layered flow. The extended theory is then applied to a single-layer flow over a bottom sill in Section 2. The results of the single layer flow are compared with the theoretical results of Naghdi and Vongsarnpigoon (1986), and with the experimental results of Sivakumaran *et al.* (1983). A detailed study of the effect of curvature on uni-directional two-layered flows is presented in Section 3, along with comparisons to the experimental measurements of Lawrence (1993).

5.1 EQUATION DERIVATION

We study the effect of streamline curvature for a homogenous layer within a multi-layered flow over a sill, as depicted in Figure 5.1. The fluid is assumed to be inviscid and incompressible, and the flow irrotational. The density is constant within each layer, but increasing for each successively deeper layer. We ignore regions of the flow where there are significant energy loss, for example, internal hydraulic jumps or flow separation. When the flow is steady, the following equations govern the flow motion in each layer.

The momentum equations,

$$\rho(uu_x + wu_z) = -P_x, \tag{5.1a}$$

$$\rho(uw_x + ww_z) = -P_z - \rho g; \tag{5.1b}$$

the continuity equation,

$$u_x + w_z = 0; \tag{5.1c}$$

the irrotationality condition,

$$u_z - w_x = 0; \tag{5.1d}$$

along with a boundary condition for the pressure at the top of the layer,

$$P = P_s \qquad \text{at} \qquad z = s, \tag{5.1e}$$

and kinematic boundary conditions at the top and bottom of the layer,

$$w = u \cdot s_x \qquad \text{at} \qquad z = s, \tag{5.1f}$$

$$w = u \cdot h_x \qquad \text{at} \qquad z = h, \tag{5.1g}$$

where the horizontal and vertical velocities are denoted by u and w respectively, P is the pressure, P_s is the pressure at the top of the layer, ρ is the density which is constant, g is the gravitational acceleration, $z = s(x)$ and $z = h(x)$ are the elevations for the top and the bottom of the layer respectively, $s = y + h$, with y being the layer thickness. Subscripts x and z refer to the differentiation with respect to the horizontal and vertical, respectively.

Integrating (5.1a) and (5.1b) with respect to x and z, and applying (5.1d), yields

$$E \equiv P + \rho g z + \tfrac{1}{2}\rho(u^2 + w^2) = constant, \tag{5.1h}$$

where E is the Bernoulli constant (mechanical energy per unit volume), and is constant throughout the flow field. It is common to simplify (5.1h) by neglecting the vertical velocity and assuming a hydrostatic pressure distribution. However, in the present study, we will include the non-hydrostatic pressure and the vertical velocity for the flow with gentle streamline curvatures, *i.e.*, $\sigma = (H/L)^2 << 1$, where H and L are the characteristic vertical and horizontal length scales.

Following the approach of Pratt (1984), the parameters are non-dimensionalized using L and H as horizontal and vertical length scales, $\sqrt{gH}$ and $\sqrt{\sigma gH}$ as horizontal and vertical velocity scales, and ρgH as a pressure scale,

$$x^* = x/L\,, \qquad z^* = z/H\,,$$

$$u^* = u/\sqrt{gH}\,, \qquad w^* = w/\sqrt{\sigma gH}\,,$$

$$P^* = P/\rho gH\,, \qquad E^* = E/\rho gH\,,$$

$$h^* = h/H\,, \qquad q^* = q/\sqrt{gH^3}\,,$$

where q is the two-dimensional flow rate. All the dimensionless variables are of $O(1)$. Substituting these dimensionless variables into (5.1) and dropping the stars, yields the following set of dimensionless equations:

$$uu_x + wu_z = -P_x, \tag{5.2a}$$

$$\sigma(uw_x + ww_z) = -P_z - 1, \tag{5.2b}$$

$$u_x + w_z = 0, \tag{5.2c}$$

$$u_z - \sigma w_x = 0, \tag{5.2d}$$

$$P = P_s \qquad \text{at} \qquad z = s, \tag{5.2e}$$

$$w = u \cdot s_x \qquad \text{at} \qquad z = s, \tag{5.2f}$$

and

$$w = u \cdot h_x \qquad \text{at} \qquad z = h. \tag{5.2g}$$

After expanding u, w, P and E in terms of the small parameter σ:

$$u = u_0 + \sigma u_1 + \cdots, \qquad w = w_0 + \sigma w_1 + \cdots, \tag{5.3a, b}$$

$$P = P_0 + \sigma P_1 + \cdots, \qquad E = E_0 + \sigma E_1 + \cdots, \tag{5.3c, d}$$

Substituting (5.3) into (5.2) yields, to zeroth order:

$$u_0 u_{0x} + w_0 u_{0z} = -P_{0x}, \tag{5.4a}$$

$$0 = -P_{0z} - 1, \tag{5.4b}$$

$$u_{0x} + w_{0z} = 0, \tag{5.4c}$$

$$u_{0z} = 0, \tag{5.4d}$$

$$P_0 = P_s \qquad \text{at} \qquad z = s, \tag{5.4e}$$

$$w_0 = u_0 \cdot s_x \qquad \text{at} \qquad z = s, \tag{5.4f}$$

and

$$w_0 = u_0 \cdot h_x \qquad \text{at} \qquad z = h. \tag{5.4g}$$

From (5.4d), u_0 is a function of x only. Integrating (5.4c) vertically and applying (5.4f) and (5.4g), yields

$$u_0 = U = q / y, \tag{5.5}$$

and

$$w_0 = U\{(\frac{z-h}{y})y_x + h_x\}. \tag{5.6}$$

If we integrate (5.4b) vertically from z to s and apply (5.4e), the pressure, to zeroth order, is hydrostatic,

$$P_0 = P_s + s - z. \tag{5.7}$$

Integrating (5.4a) with respect to x, and applying (5.4d) and (5.7), yields

$$E_0 = P_s + s + \tfrac{1}{2}u_0^2. \tag{5.8}$$

Thus to the lowest order, the horizontal velocity is uniform across the depth, and the vertical velocity does not affect the pressure and the layer energy, with the pressure being hydrostatic. The above results give the hydraulic theory. Note, however, that (5.6) gives non-zero vertical velocity. This is due to the different scales adopted for u and w.

To first order, Eq. (5.2) becomes

$$u_0 u_{1x} + u_1 u_{0x} + w_0 u_{1z} + w_1 u_{0z} = -P_{1x} \ , \tag{5.9a}$$

$$u_0 w_{0x} + w_0 w_{0z} = -P_{1z} \ , \tag{5.9b}$$

$$u_{1x} + w_{1z} = 0 \ , \tag{5.9c}$$

$$u_{1z} - w_{0x} = 0 \ , \tag{5.9d}$$

$$P_1 = 0 \qquad \text{at} \qquad z = s \ , \tag{5.9e}$$

$$w_1 = u_1 \cdot s_x \qquad \text{at} \qquad z = s \ , \tag{5.9f}$$

and

$$w_1 = u_1 \cdot h_x \qquad \text{at} \qquad z = h \ . \tag{5.9g}$$

Using (5.6), u_1 can be obtained by integrating (5.9d) vertically

$$u_1 = U\left\{\frac{(z-h)^2}{2y^2}(-2y_x^2 + yy_{xx}) + \frac{z}{y}(-2y_x h_x + yh_{xx})\right\} + c_2(x) \ . \tag{5.10}$$

Integrating (5.3a) vertically from h to s, and using $u_0 = U$, yields

$$\int_h^s u_1 dz = O(\sigma). \tag{5.11}$$

Integrating (5.10) vertically from h to s and applying using (5.11), u_1 then becomes

$$u_1 = U\left\{\frac{3(z-h)^2 - y^2}{6y^2}(-2y_x^2 + yy_{xx}) + \frac{2(z-h) - y}{2y}(-2y_x h_x + yh_{xx})\right\}. \tag{5.12}$$

Integrating (5.9b) vertically from z to s, after applying (5.9d), (5.9e), and (5.4d), yields

$$P_1 = u_{0s} u_{1s} + \tfrac{1}{2} w_{0s}^2 - u_0 u_1 - \tfrac{1}{2} w_0^2 \ . \tag{5.13}$$

Substituting w_0 and u_1, the correction to the pressure becomes

$$P_1 = U^2\left\{\frac{y^2 - (z-h)^2}{2y^2}(yy_{xx} - y_x^2) + \frac{y - (z-h)}{y}(yh_{xx} - h_x y_x)\right\} . \tag{5.14}$$

Using (5.9d) and (5.4d), integrating (5.9a) with respect to x, yields

$$E_1 = u_{0s} u_{1s} + \tfrac{1}{2} w_{0s}^2. \tag{5.15}$$

Substituting u_0, u_1 and w_0, the correction to the energy becomes

$$E_1 = U^2 \{y(2y_{xx} + 3h_{xx}) - y_x^2 + 3h_x^2\}/6. \tag{5.16}$$

The vertical velocity w_I can also be obtained using (5.9c), (5.9f) and (5.9g), but is not needed for this study.

Thus to order $O(\sigma^2)$, the Bernoulli constant (layer energy) can be expressed as

$$E = P_s + y + h + \tfrac{1}{2}U^2 + \tfrac{1}{6}\sigma U^2\left\{y(2y_{xx} + 3h_{xx}) - y_x^2 + 3h_x^2\right\} . \tag{5.17}$$

The pressure on the layer bottom P_h becomes

$$P_h = P_s + y + \tfrac{1}{2}\sigma U^2\{y(y_{xx} + 2h_{xx}) - y_x^2 - 2y_x h_x\} . \tag{5.18}$$

Equation (5.17) is the same as that obtained by Naghdi and Vongsarnpigoon (1986) for a single-layer flow using the direct theory of constrained fluid sheets. Our method presented above is simpler and can be easily applied to problems with any number of layers. This is important as we are mainly interested in two-layer flow problems. In the following sections, the above equations will be used to study the curvature effects in both single and two-layered flows over a sill.

5.2 SINGLE LAYER FLOW WITH CURVATURE EFFECTS

The above equations can be readily applied to single-layer flows over a smooth sill with $\sigma = (H/L)^2 << 1$, where H and L are chosen as the far upstream layer thickness and the sill length, respectively. Here y is the layer thickness, h is the sill height, q is the two-dimensional flow rate, and $U = q/y$ is the mean flow velocity. For single layer flows, the pressure at the free surface $P_s = 0$, and the layer energy and the pressure on the bed can be obtained from (5.17) and (5.18). Write the layer energy E in terms of a hydrostatic (H) and non-hydrostatic (NH) part:

$$E = E_H + E_{NH}, \tag{5.19}$$

with

$$E_H = y + h + \tfrac{1}{2}U^2,$$

and

$$E_{NH} = \tfrac{1}{6}\sigma U^2\left\{y(2y_{xx} + 3h_{xx}) - y_x^2 + 3h_x^2\right\}.$$

Since E is conserved, $dE/dx = 0$, and (5.19) gives

$$\frac{dy}{dx} = -\frac{S_0 + S_c}{1 - F^2} \tag{5.20a}$$

where $S_0 = \sigma^{\frac{1}{2}}(F^2 h_x)$ is the topographic slope for the straight channel, (5.20b)

$S_c = d(E_{NH}) / dx$ is the slope due to the curvature effects, (5.20c)

with $F^2 = U^2/y$ being the Froude number.

At the control point, *i.e.*, $F^2 = 1$, $S_0 + S_c = 0$ must be satisfied, see (5.20a). For the hydrostatic crest-controlled flow, the flow is critical at $S_0 = 0$, which is satisfied at the sill crest point. However, when the curvature effects are included, the critical point is shifted to the position where $S_0 + S_c = 0$.

5.2.1 Numerical Schemes

For crest-controlled flows, the hydrostatic solution gives a good approximation to the real solution. This hydrostatic solution can be improved by including the effect of curvature (E_{NH}) calculated from the hydrostatic solution. Further improvement can be made using the newly obtained solution. The iteration can be continued until the result converges. In fact, this iteration converges very quickly: two to three iterations are usually enough. Unfortunately, the iteration method is not generally applicable for some flow situations where there are no hydrostatic solutions, such as approach-controlled flows. Thus an alternative to the iteration method is required.

Equation (5.19) is a non-linear second order ordinary differential equation (ODE), and can be arranged in the following form

$$\sigma y_{xx} - \tfrac{1}{2}\sigma y^{-1} y_x^2 + a_1 y^{-1} + a_2 y + a_3 y^2 + \tfrac{3}{2}\sigma h_{xx} = 0, \tag{5.21}$$

where

$$a_1 = \tfrac{3}{2}(1 + \sigma h_x^2),$$

$$a_2 = -3(E - h)q^{-2},$$

$$a_3 = 3q^{-2}.$$

a_1, a_2 and a_3 have an order of one. The energy E is unknown and can be solved using the control conditions for crest-controlled flows.

Given that the coefficients in both the y_{xx} and y_x terms in (5.21) are small due to the small parameter $\sigma << 1$, the equation is therefore a stiff equation. To solve such an equation is a mathematical challenge due to its sensitivity to the boundary conditions, (Wetton, pers. comm.). The equation is further complicated by its non-linear nature, and the implicit singular point within the computation domain, *i.e.*, the critical point (Naghdi & Vongsarnpigoon, 1986). On top of these, the real boundary conditions are unknown: these are determined by the implicit control conditions.

Naghdi & Vongsarnpigoon (1986) used a shooting method to solve the equation by adjusting the upper stream layer thickness. However they found that the layer thickness vanished at some point within the computation domain before they found the real solution. The reason for their failure is that the solution to (5.21) contains a significant exponential component. Therefore small disturbances in the initial guess grow exponentially and eventually overwhelm the real solution. We have, however, successfully solved (5.21) as a boundary value problem (BVP) using a general-purpose code, COLNEW, developed by Ascher *et al.* (1981). In applying the code, two boundary conditions are needed. With the constant energy equation, the flow conditions at the two boundaries are related. The equation is solved using trial and error by adjusting the boundary condition until the control condition is satisfied.

5.2.2 Comparison with Experimental Results

Sivakumaran *et al.* (1983) conducted experiments using single-layer crest-controlled flows over a bell-shaped sill satisfying $h = h_m \exp[-(2x/L)^2]$, where the sill height h_m = 20 cm, the sill length L = 192 cm. The upstream layer depth H = 34.3 cm, and the flow rate q = 1119.7 cm^2/s. Thus $\sigma = (H/L)^2 = 0.04 << 1$ and the sill is finite with $h_m/H = 0.6$.

The predictions for the bed pressure and the surface position are shown in Figure 5.2, compared with the experimental measurements of Sivakumaran *et al.* (taken from their Figure 5.7(a)). The pressure on the sill crest is therefore reduced, given the negative surface and the sill curvatures (s_{xx} and h_{xx} both less than zero) at the sill crest. Conversely, the pressure at the foot of the sill is increased given the positive surface and the sill curvatures. With non-hydrostatic effect considered, the pressure on the sill is very well predicted. The importance of the non-hydrostatic pressure is therefore confirmed.

The change of the curvature slope (S_c) and the topographic slope (S_0) are plotted in Figure 5.2 (here ($-S_0$) is plotted). At the intersection of the two lines, where $S_0 + S_c = 0$, the flow is critical ($F^2 = 1$), as expected from Eq. (5.20). Given that S_c is slightly negative, the control point is shifted about 0.01 (2 to 3 cm) upstream from the sill crest. The shift of the control is not significant, but needs to be included when solving Eq. (5.20).

Given the small shift of the control position, E_H at the new control point is almost identical to that from the hydrostatic problem. However, the total energy E is reduced by an amount $E_{NH}(x=0)$. At the far upstream and downstream, the curvature effect is negligibly small, thus E_H is also reduced by E_{NH} (x=0). This causes the layer thickness to change by $\Delta y = \Delta E_H / (1 - F^2)$ (see Eq.(5.19)). The upstream layer thickness is then reduced given the flow is subcritical, while the downstream layer thickness is increased. With the effects of curvature included, the prediction of the interface position is improved, as shown in Figure 5.2.

Both E_{NH} and P_{NH} come mainly from of the curvature of the surface, s_{xx}, and the sill, h_{xx}, see Figure 5.3. At the sill crest region, only s_{xx} and h_{xx} are important while all other terms are negligibly small. At $x = 0.2$, these two terms are still dominant while other terms are canceling each other. Thus the change of E_{NH} and P_{NH} are consistent with the change of s_{xx} and h_{xx}, with E_{NH} going to a minimum in the vicinity of the sill crest and to a maximum at about $x = 0.2$. E_{NH} is important in the sill region, while it is small far upstream and downstream where the bottom is almost flat.

5.3 TWO-LAYER FLOW OVER A SILL

5.3.1 Equation Derivation for Two-layer Flows

We now study the steady, inviscid and irrotational two-layer flow over a smooth isolated two-dimensional sill in an otherwise horizontal channel. The flow is shallow with $\sigma = (H/L)^2 << 1$, where H and L are chosen as the total upstream depth and the sill length respectively. The density difference between the two layers is small, *i.e.*, $\varepsilon = \Delta\rho/\rho_2 << 1$, or the flow is Boussinesq. For Boussinesq flows, the slope of the free surface, with an order as ε, is much smaller than that of the interface, with an order of one, (see, for example, Lawrence 1993).

All variables are non-dimensionalized with respect to H, L, ρ_2, and g, except for u_i and q_i, where $g' = \varepsilon g$ is the relevant variable as the flow velocities are dependent on g' rather than g:

$$
\begin{aligned}
x^* &= x/L\ , & z^* &= z/H\ , \\
u_i^* &= u_i\big/\sqrt{g'H}\ , & P_i^* &= P_i/\rho_2 gH\ , \\
E_i^* &= E_i/\rho_2 gH\ , & q_i^* &= q_i\big/\sqrt{g'H^3}\ .
\end{aligned}
\tag{5.22}
$$

The stars indicate that variables are non-dimensional, and will later be dropped. All the dimensionless variables are in the order of $O(1)$.

Write the mean horizontal velocity for each layer as:

$$U_i = q_i/y_i \quad (i = 1, 2), \tag{5.23}$$

the layer energy for the upper and lower layer and the pressure on the interface can be obtained from (5.17) and (5.18). For the upper layer, the pressure at the free surface $P_s = 0$. In applying (5.17) and (5.18), substituting $h + y_2$ into h, y_1 into y, and s into $h + y$, yields the pressure on the interface and the energy for the upper layer,

$$P_1(x, y_2 + h) = ry_1 + \frac{r\varepsilon\sigma U_1^2}{2}(-y_1 y_{1xx} + y_{1x}^2)\ , \tag{5.24}$$

and $$E_1 = rs + r\varepsilon\{\tfrac{1}{2}U_1^2 + \frac{\sigma U_1^2}{6}(-y_1 y_{1xx} + 2y_{1x}^2)\}, \tag{5.25}$$

where $r = \rho_1/\rho_2$, and $\varepsilon = 1 - r = \Delta\rho/\rho_2 << 1$.

For the lower layer, the pressure on the interface becomes

$$P_s = P_2(x,\ h + y_2) = P_1(x,\ h + y_2), \tag{5.26}$$

since the pressure is continuous across the interface. Substituting h into h, y_2 into y, and $h + y_2$ into $h + y$, (5.17) gives:

$$E_2 = rs + \varepsilon\{h + y_2 + \tfrac{1}{2}U_2^2 + \frac{\sigma U_2^2}{6}(2y_2 y_{2xx} + 3y_2 h_{xx} + 3h_x^2 - y_{2x}^2) + \frac{r\sigma U_1^2}{2}(-y_1 y_{1xx} + y_{1x}^2)\}\ . \tag{5.27}$$

In deriving (5.24) - (5.27), the terms with ε^2 are neglected given the flow is Boussinesq (*i.e.*, $\varepsilon << 1$). Subtracting (5.25) from (5.27) to cancel the term *rs*, which has an order of one while all other terms have a factor of ε, we define the internal energy for two layer flows, E, as

$$E = \frac{E_2 - E_1}{\varepsilon}. \tag{5.28}$$

This internal energy E describes the internal hydraulics of two-layer flows (Armi 1986; Lawrence 1993). With the term *rs* being canceled out, the deflection of the surface elevation then has only higher order effects on E and can be neglected. Writing E as the sum of the hydrostatic part E_H and the non-hydrostatic part E_{NH} due to the flow streamline curvature

$$E = E_H + E_{NH}, \tag{5.29a}$$

with $$E_H = h + y_2 + \frac{1}{2}(U_2^2 - U_1^2)\ , \tag{5.29b}$$

$$E_{NH} = \frac{\sigma U_2^2}{6}(2y_2 y_{2xx} + 3y_2 h_{xx} + 3h_x^2 - y_{2x}^2) + \frac{\sigma U_1^2}{6}(2y_1(y_{2xx} + h_{xx}) + (y_{2x} + h_x)^2). \tag{5.29c}$$

Given that E_1 and E_2 are conserved, E is also conserved throughout the channel in the absence of hydraulic jumps or flow separation. Differentiating (5.29) with respect to x, the slope of the interface y ($y = y_2 + h$) becomes

$$y_x = -\frac{S_o + S_c}{1 - G^2} \tag{5.30a}$$

where $S_0 = \sigma^{\frac{1}{2}}(F_2^2 h_x)$ is the topographic slope for the straight channel, (5.30b)

$S_c = d(E_{NH})/dx$ is the slope due to the curvature effects, (5.30c)

and $$G^2 = F_1^2 + F_2^2 - \varepsilon F_1^2 F_2^2 \approx F_1^2 + F_2^2$$

is the composite Froude number, with $F_i^2 = U_i^2/y_i$ being the densimetric Froude number for layer i.

The composite Froude number, G^2, serves the same role for two layer flows, as the classical Froude number (see, for example, Henderson 1966) does for single-layer (open channel) flows, *i.e.*, the locations where $G^2 = 1$ are described as (internal) control points, and the flow is supercritical (or subcritical) when $G^2 > 1$ (or $G^2 < 1$). At control points where $G^2 = 1$, $S_0 + S_c = 0$ must be satisfied. With the curvature effects considered, the control point moves from the point where $S_0 = 0$ to the point where $S_0 + S_c = 0$. The exact location of this control depends on the flow conditions.

Equation (5.29) can be re-arranged in terms of a single parameter, such as the interface position y, ($y = y_2 + h$).

$$\tfrac{1}{3}\left(\frac{q_1^2}{y_1} + \frac{q_2^2}{y_2}\right)y_{xx} + \frac{q_2^2}{y_2^2}\left(\tfrac{1}{6}y_2 h_{xx} + \tfrac{1}{2}h_x^2 - \tfrac{1}{6}y_{2x}^2\right) + \frac{1}{6}\frac{q_1^2}{y_1^2}y_x^2 + \tfrac{1}{2}\left(-\frac{q_1^2}{y_1^2} + \frac{q_2^2}{y_2^2}\right) + y = E \tag{5.31}$$

Eq. (5.31) is a non-linear second order ODE, similar to (5.21). Unlike single-layer flows over a sill, however, some of the two-layer flows have no hydrostatic solutions, such as approach-controlled flows, (see Lawrence 1993). Thus the iteration method starting from the hydrostatic solution cannot be applied. Equation (5.31) will then be solved numerically as a boundary value problem (BVP) using a solver COLNEW, similar to the single-layer flows. Here we study approach-controlled flows using the equations derived above to include curvature effect.

5.3.2 Comparison with experiments

Two-layer uni-directional flow over a sill has been studied by Lawrence (1993). Four flow regimes were identified: subcritical, crest-controlled, supercritical, and approach-controlled. The first three regimes have their one-layer counterparts, while the approach-controlled flow, with the flow being critical at the foot of the sill, is unique for the two-layer flows, and can not be predicted using hydrostatic theory. The approach-controlled flow of Experiment 17 of Lawrence (1993) (plotted in his Figure 14) is predicted and compared with the experimental measurements in Figure 5.4. The flow has the following parameters: q_1 = 101 cm^2/s, q_2 = 99 cm^2/s, g' = 8.0 cm/s^2, and the sill has a shape $h = h_m \cos^2(\pi x/L)$ (for $|x / L| \leq \frac{1}{2}$), with the sill height h_m = 15 cm, and the sill length L = 188 cm. The total depth H = 40.2 cm. Therefore, the sill is smooth and of finite size, with $\sigma = (H/L)^2 \approx 0.05 << 1$ and $h_m/H \approx 0.35$.

This approach-controlled flow is critical around the foot of the sill. It starts passing the sill supercritically with the interface level rising, similar to supercritical flows, Figure 5.4, but unlike the supercritical flow where the interface level is symmetric with respect to the sill crest, the composite Froude number G^2 decreases after the sill crest and being symmetric with respect to the sill crest, the G^2 initially decreases after the sill crest but it then increases until the jump starts, similar to crest-controlled flows, Figure 5.4. The variation of the curvature slope S_c, the topographic slope (here ($-S_0$) is plotted) are also plotted in Figure 5.4. There are three points where $S_0 + S_c = 0$. The first, point A, occurs upstream of the sill crest at about x = - 0.07, and the other two, points B and C, are located in the downstream portion of the sill at x = 0.3 and x = 0.4, respectively. At point A, G^2 achieves its local maximum, increasing from the approach control (G^2 = 1) near the foot of the sill, similar to supercritical flows. But, unlike supercritical flows, G^2 drops shortly below one in the region between B and C, and it then increases to become supercritical again until the jump occurs at x about 0.6, similar to the crest-controlled flow passing a sill. Also notice that at B and C, $G^2 = 1$. However, for this approach-controlled flow, these points are different from the conventional control points.

The variation of E_{NH} along x-axis is shown in Figure 5.5, together with each component of E_{NH}. The change of E_{NH} is initially small, until it is close to the sill crest, at about $x = -0.3$. It then starts to decrease with increasing rate when the flow passes through the crest, with its minimum of - 0.04 reached at about $x = 0.2$ downstream of the sill crest. It then increases sharply until about $x = 0.4$ with a maximum of 0.04. After that, E_{NH} decreases gradually to zero. This change of E_{NH} is mainly due to the curvature of the interface position y_{xx}, while the contribution of the sill curvature, h_{xx}, is almost insignificant. This large y_{xx} term is the characteristic of approach-controlled flows.

The prediction of the interface position, Figure 5.4, shows that the interfacial position is so unique that it differs significantly from the symmetric supercritical flow predicted from hydraulic theory. Hydraulic theory fails to predict approach-controlled flows since the curvature effects are too significant to be neglected. If non-hydrostatic effects are included, approach-controlled flows can be accurately predicted.

Chapter 6

EXCHANGE FLOWS WITH FRICTION AND CURVATURE EFFECTS

Effects of streamline curvature on inviscid single and two-layer flows over a sill were studied in Chapter 5. Effects of friction can also be important in some flow situations, particularly in exchange flows where two layers move in opposite directions (Bormans & Garrett 1989; Hamblin & Lawrence 1990; Cheung & Lawrence 1991). In this chapter, the effects of friction and curvature are incorporated into the analysis of steady maximal exchange flow through a channel of constant width. The flow is shallow, with $\sigma = (H/L)^2 << 1$, where H is the total depth and L is the channel length, (see Figure 2.1). The sill is smooth with its height much less than its length. Also the density difference between the two layers is small, and there is no barotropic forcing, *i.e.*, $q_1 = q_2 = q$. The non-hydrostatic internal hydraulic theory is first extended to include the friction caused by the sidewalls, bottom, and the interface. The friction factors are then estimated theoretically and experimentally. Finally, the theoretical predictions incorporating the effects of both friction and curvature are compared with the experimental measurements.

6.1 EQUATION DERIVATION

Exchange flows through a channel are subject to friction caused by the sidewalls, bottom, surface, and the interface, (see Figure 6.1). Internal hydraulic theory can be extended to include the frictional effects. For layer i, the change in Bernoulli energy, $E_i = P + \rho_i g z + \frac{1}{2}\rho_i(u^2 + w^2)$, due to the shear stresses can be written as,

$$\frac{dE_i}{dx} = \frac{\sum_j \tau_j \cdot dS_j}{A \cdot dx}, \tag{6.1}$$

where Σ is the summation over the shear stress τ_j acting on the layer, S_j is the area over which the shear stress τ_j acts on the layer, and A is the layer cross section area, $A = by_i$, with b being the width of the channel and y_i the layer thickness. Subscripts i = 1, 2 refer to the upper and lower layer, respectively.

The shear stresses can be expressed as:

$$\tau_{wi} = f_{wi} \cdot \tfrac{1}{2}\rho_i U_i^2, \qquad \tau_s = f_s \cdot \tfrac{1}{2}\rho_1 U_1^2, \qquad \tau_I = f_I \cdot \tfrac{1}{2}\overline{\rho}(\Delta U)^2, \tag{6.2}$$

where f is the friction factor, $\overline{\rho}$ is the mean density of the two layers, $U_i = q_i/y_i$ is the averaged layer velocity, and $\Delta U = |U_1 - U_2|$. Subscripts I, w and s denote the interface, wall and surface, respectively. In Eq. (6.2) we assume that the sidewalls have the same friction factors f_{wi} (i = 1, 2) for each layer, and for the lower layer, the bottom and the sidewalls have the same friction factor.

After substituting Eq. (6.2) into Eq. (6.1), non-dimensionalizing all the parameters according to Eq. (5.22), and dropping the stars, the slope of the internal energy dE/dx, where $E = (E_2 - E_1)/\varepsilon$, (see Eq. 5.28), can be expressed as:

$$\frac{dE}{dx} = S_f, \tag{6.3}$$

where S_f is the friction slope, similar to that of single-layer flows, (Henderson 1966), with

$$S_f = \sigma^{-1/2}\Big\{[\pm\tfrac{1}{2} f_{w2} U_2^2 (2y_2 + b) + \tfrac{1}{2} f_I (\Delta U)^2 b]/y_2 b \\ + [\tfrac{1}{2} f_{w1} U_1^2 (2y_1) + \tfrac{1}{2} f_I (\Delta U)^2 b + \tfrac{1}{2} f_s U_1^2 b]/y_1 b\Big\}. \tag{6.4}$$

In Eq. (6.4), $\sigma = (H/L)^2$. Eq. (6.4) can be applied to both exchange flows and uni-directional flows: for exchange flows, $\Delta U = |U_1| + |U_2|$ and plus sign is chosen for the first term on the right hand side; for uni-directional flows, $\Delta U = |U_2 - U_1|$ and minus sign is chosen.

When curvature effects are also significant, the internal energy is then $E = E_H + E_{NH}$, (see Eq. (5.29)). Equation (5.29) can be re-arranged as,

$$\sigma y_{xx} = \frac{3y_1y_2}{y_1+y_2}\left\{\frac{E-y}{q^2} - \frac{1}{2}\left(\frac{1}{y_2^2} - \frac{1}{y_1^2}\right) - \sigma\left(\frac{h_{xx}}{6y_2} + \frac{h_x^2}{2y_2^2} - \frac{y_{2x}^2}{6y_2^2} + \frac{y_x^2}{6y_1^2}\right)\right\}, \tag{6.5}$$

where y_1 and y_2 are the upper and lower layer thickness, $y = y_2 + h$ is the interface position. In deriving Eq. (6.5), $q_1 = q_2 = q$ is used assuming no barotropic forcing.

Equations (6.3) and (6.5) can be used to solve exchange flows with both friction and curvature effects considered. For maximal exchange flows, two control conditions are needed to solve the above coupled equations.

6.1.1 Control Conditions for Maximal Exchange Flows

For maximal exchange flows, the flows are controlled by two hydraulic controls (Armi 1986; Farmer & Armi 1986). To identify the points of control, Eq. (6.3) is expressed in the following form by substituting $E = E_H + E_{NH}$:

$$y_x = \frac{S_f - S_0 - S_c}{1 - G^2}, \tag{6.6}$$

where S_f is the friction slope and given in Eq. (6.4),

S_c is the curvature slope, $S_c = \mathrm{d}(E_{NH})/\mathrm{d}x$, where E_{NH} is given by Eq. (5.29c),

S_0 is the topographic slope,

$$S_0 = \sigma^{\frac{1}{2}}[F_2^2 h_x + (y_1F_1^2 - y_2F_2^2)b_x/b]\,. \tag{6.7}$$

The effects of the change in the channel width b is also included in Eq. (6.7) as it will be used to study the effect of the channel exit.

For inviscid hydrostatic flows, both S_f and S_c are zero. The point where $G^2 = 1$, *i.e.* the control point, must have $S_0 = 0$, as well as $y_x \neq 0$. Thus the two controls are at the sill crest and at the right hand exit of the channel, as has been discussed by Farmer & Armi (1986).

When friction is considered while curvature effects are neglected, *i.e.*, $S_c = 0$, S_f can be calculated from Eq. (6.4) and is always a positive value throughout the channel. The sill control is then shifted to the point where $S_f - S_0 = 0$. This new control occurs at a point left to the sill crest point since the sill has a positive slope h_x there (see Eq.(6.7)). The amount of the shift depends on the flow conditions as well as the shape of the sill, and is unknown before the flow is determined. To the right of the sill, $S_0 = 0$ due to $h_x = 0$ and $b_x = 0$ within the channel. Thus $S_f - S_0 = 0$ cannot be satisfied since S_f is a positive value. At the channel right hand exit, however, S_0 jumps from zero within the channel to a value very large, due to the large b_x resulting from the sharp end and the fact that $y_1 < y_2$, see Eq. (6.7). Therefore $S_f - S_0 = 0$ is forced at the channel right hand exit, and the exit control $G^2 = 1$ stays at the exit. The sharp end of the channel, however, also complicates the flow, as the lower layer is no longer uniform due to the flow separation after the entrance. Nevertheless, this effect is not significant due to the fact that $F_1^2 >> F_2^2$, (see Section 6.4).

When both the curvature and friction are considered, the sill control is then shifted to the point where $S_f - S_0 - S_c = 0$. The amount of the shift depends on the flow conditions as well as the sill shape. The exit control is still forced at the channel right hand exit due to the large S_0 caused by the sharp end of the channel.

6.1.2 Numerical Methods

Exchange flow problems can be greatly simplified when curvature effects are neglected. Without curvature effects, $E_{NH} = 0$ and $S_c = 0$, Eq. (6.6) becomes

$$y_x = \frac{S_f - S_0}{1 - G^2}, \tag{6.8}$$

where S_f is obtained in Eq. (6.4), and S_0 is expressed in Eq. (6.7). Equation (6.8) is a first order ordinary differential equation (ODE). The equation and the flow rate q can be solved numerically using two control conditions for maximal exchange flows. The problem is complicated by the fact that the position of the sill control is shifted to an unknown point due to the friction. Detailed numerical schemes are presented in Appendix A with the shift of the sill control due to the friction accommodated, unlike other studies (*e.g.* Bormans & Garrett 1989) where this shift is neglected.

When both friction and curvature effects are considered, two coupled equations, Eqs. (6.3) and (6.5), together with two control conditions can be used to solve for the exchange flow. Equation (6.3) is a first order ODE, while Eq. (6.5) is a second order ODE. The prediction of the exchange flows is much more complicated with both the flow rate and the sill control position unknown. The details of the numerical techniques employed to solve the exchange flow problem are presented in Appendix A.

6.2 ESTIMATION OF FRICTION FACTORS

To quantify the frictional effects, the friction factors need to be determined. The wall friction factors are estimated from boundary layer theories, while the interfacial friction factor is estimated experimentally.

6.2.1 Wall Friction Factors

For our experimental flows, the Reynolds number Re_L

$$Re_L = \overline{U}L/\nu, \tag{6.9}$$

where $\overline{U} = 2q/H$, is about 20,000, and the boundary layers are laminar (White 1991). The maximum boundary layer thickness for sidewalls ($\approx$ 4 cm) is less than the half-width of the channel. Thus boundary layers are not fully developed, and the boundary layer theories can be used to calculate the wall friction factors. To simplify the study, the boundary layer theories of a flat plate were applied to both the sidewalls and the bottom. For the exchange flows studied, the mean velocity for each layer increases downstream for both the upper and lower layer. The Blasius theory for the development of boundary layers of a flat plate within an uniform velocity field is therefore not applicable. Instead, an integral momentum method, Thwaites method (see White 1991) needs to be used. Thwaites method studies the development of boundary layers in a flow field with a horizontal velocity gradient. The details of how Thwaites method is applied to our flows are presented in Appendix B.

The wall friction factor for the upper layer, f_w, is predicted using both Thwaites method and Blasius theory for a symmetric exchange flow, see Figure 6.2. This exchange flow is laminar, and the boundary layers are not fully developed for the sidewalls, surface and bottom. In applying Blasius theory, the averaged velocity, $U = 2q/H$, is used. The wall friction factors predicted from both methods decrease towards downstream due to the development of the boundary layers. Compared to Thwaites method, Blasius theory significantly underestimates the wall friction factor by about 50 - 100 % for this accelerating flow. Thus, for exchange flows where each layer is accelerating, Thwaites method should be used.

For the exchange flow over a sill, the flow is more complicated since the interface is no longer anti-symmetric, and the bottom of the channel is no longer flat due to the existence of the sill. But given that the sill is smooth, the bottom can still be approximated as a flat plate. Detailed assumptions and treatment in applying Thwaites method are discussed in Appendix B. In the following study, a mean wall friction factor will be used by averaging f_w over the channel to simplify the study.

The wall friction factor changes with the Reynolds number Re_L, which in turn is a function of the flow rate q for a given channel. Thwaites method predicts relatively close wall friction factors for both layers. Thus the same f_w is used for both layers. The change of f_w with Re_L for the exchange flow over a sill is presented in Figure 6.3. The wall friction factor decreases with the increase of Re_L, as expected. For the experiments with Re_L changing from 10,000 to 40,000, the predicted f_w changes from 0.024 to 0.012.

6.2.2 Interfacial Friction Factor

Unlike the wall friction factors, the interfacial friction factor is much more difficult to predict. It is determined by interfacial flow conditions which are not well understood. Various studies have been conducted to predict the interfacial friction factor from the interfacial flow parameters, but the predictions from different studies vary by one to two orders of magnitude (Cheung & Lawrence 1991). In the present study, the interfacial friction factor is determined experimentally.

Given that the internal energy is changed by friction, the interfacial friction factor can then be determined if the change in internal energy is estimated from the experimental measurements. The following equation relating the friction factors is obtained from Eqs. (6.3) and (6.4) for exchange flows:

$$a_I f_I + a_w f_w + a_s f_s = [E(x_2) - E(x_1)] / q^2, \tag{6.10}$$

where a_I, a_w, and a_s are the functions of interface positions only, and can be expressed as

$$a_I = \frac{1}{2}\int_{x_1}^{x_2} \left(\frac{1}{y_1} + \frac{1}{y_2}\right)^3 dx,$$

$$a_w = \frac{1}{2}\int_{x_1}^{x_2} \frac{1}{b}\left(\frac{2}{y_1^2} + \frac{2y_2 + b}{y_2^3}\right) dx, \tag{6.11}$$

$$a_s = \frac{1}{2}\int_{x_1}^{x_2} \frac{1}{y_1^3} dx.$$

Equation (6.10) relates f_s, f_w and f_I, when the flow rate and the interface positions are measured. f_I can then be determined when f_s and f_w are obtained. All the friction factors f_w, f_s and f_I in Eq. (6.10) are the mean values averaged throughout the channel. The use of the mean friction factors greatly simplifies the study and is justified since it can be shown that the resulting error is small.

In applying Eq. (6.10), the measurements are taken from steady maximal exchange flows. The hydrostatic component of the internal energy E_H can be easily estimated from the experimental measurements, whereas the non-hydrostatic component E_{NH} is considerably more difficult to estimate, since it involves the streamline curvature which is a function of the second derivatives of the interface profiles. To avoid this difficulty, the measured interface positions in the region between $x_1 = 0.3$ and $x_2 = 0.8$ were used, as E_{NH} was negligibly small in the region (see Section 6.3).

A typical relationship between f_w and f_I is plotted in Figure 6.4 for Exp. 2, using the measured interface positions and the flow rate, while the friction for the free surface is neglected. Using Figure 6.3 and Figure 6.4, both the wall and interfacial friction factor were predicted when the flow rate and the interface position were measured. Similarly the interfacial friction factors for different experiments were estimated, and plotted against the bulk Richardson number J, the shear Reynolds number Re, and the stability parameter or Keulegan number, $\theta^{-3} = \Delta U^3 / g'\nu = Re/J$, see Figure 6.5. A line of best fit was obtained from these measurements using the least square method, and plotted in Figure 6.5, together with the plus and minus one standard deviation lines. The interfacial friction factor f_I increases slightly when J increases from about 0.2 to 0.5. It decreases from about 0.015 to 0.005 when the shear Reynolds number increases from 1000 to 3000. f_I also decreases when the stability parameter increases. The above results should be taken with care when they are applied to other flow situations due to the limited range of the measurements.

The above estimates of f_I are subject to various sources of errors, most importantly, the errors in determining the interface position and the flow rate. The effects of these errors on the estimation of f_I are studied as follows. Using Eq. (6.10) and assuming a constant f_w, a 5 % change in the flow rate will result in about 25 % change in the estimate of f_I; and a 20 % change of the difference of the interface elevations between x_1 and x_2 (about 3 mm) will result in about 20 % change in f_I. Therefore, the combined error could be as large as 45 %. Besides, the error in determining f_w also affects the prediction of f_I. Using larger f_w will result in smaller f_I, and vice versa, (Figure 6.4). For f_w with an error of 20 %, the resultant f_I could have an error of about 10 %. As a result, there could be a possible 50 % error in estimating f_I using our experimental measurements.

The interfacial friction factors for our experiments had also been calculated using empirical or semi-empirical formulae suggested by various researchers, see Figure 6.6. The predictions of Arita and Jirka (1987) and Grubert (1989), though widely scattered, are comparable with our measurements, while those of Dermissis and Partheniades (1984) and Abraham *et al.* (1979) are relatively smaller. The diversity of the predicted interfacial friction factor might be caused by various factors. Firstly, the experimental estimates of f_I are sometimes very diverse. For example, the estimated f_I changes from 0.004 to 0.040 under the identical flow conditions for some experiments as summarized by Arita and Jirka (1987). Secondly, different flow conditions could lead to significantly different f_I, and simple parameterization methods used for predictions might not able to characterize the flow conditions. Thirdly, different methods in determining f_I, such as the force balance method (Dermissis & Partheniades 1984) or the linear shear method (Abraham & Eysink 1971), are also responsible in the difference. Therefore, given the uncertainty of the theoretical predictions, the experimentally obtained f_I needs to be used for this study of exchange flows.

Reynolds stress

The interfacial shear stress can be separated into the viscous stress and the Reynolds stress:

$$\tau_I = \mu \frac{du}{dz} - \rho \overline{u'w'} = (f_I^{(v)} + f_I^{(R)}) \tfrac{1}{2} \rho (\Delta U)^2, \tag{6.12}$$

where $f_I^{(v)}$ and $f_I^{(R)}$ are the interfacial friction factors for the viscous stress and Reynolds stress components, respectively. For the viscous stress,

$$\tau_I^{(v)} = \mu \frac{du}{dz} = \rho \nu \Delta U / \delta. \tag{6.13}$$

$f_I^{(v)}$ can be estimated as

$$f_I^{(v)} = 2\nu / (\delta \cdot \Delta U). \tag{6.14}$$

The estimates of $f_I^{(v)}$ from our experiments range from 0.001 to 0.002, given $\delta \approx 4$ cm and $\Delta U \approx 3$ cm/sec. Knowing that f_I ranges from 0.005 to 0.015 from the measurements (see Figure 6.5), the viscous stress composes only about 10 - 20 % of the total shear stress, while 80 - 90 % of the total shear stress is the Reynolds stress. Therefore, the Reynolds stress is dominant for the experimental flows even though the shear Reynolds number is relatively small, about 1000 to 2000. As the Reynolds stress is a function of interfacial flow conditions and interfacial instabilities (see, for example, Haigh 1995), the interfacial friction is therefore closely related to the interfacial instabilities.

6.3 COMPARISON WITH EXPERIMENTS

Once friction factors have been estimated, the exchange flow are predicted, and the prediction are then compared to the experimental measurements. In order to better understand the effects of friction and curvature in exchange flows, the theoretical predictions will be obtained assuming the flow is inviscid hydrostatic, viscous hydrostatic (*i.e.*, including frictional effects but not curvature effects), and viscous non-hydrostatic (*i.e.*, including both friction and curvature effects). The detailed comparison will be made for Exp. 2 for the exchange flow through a short channel with a sill of h_m = 8.0 cm. This is followed by a comparison of the flow rates for a series of experiments with different density differences.

6.3.1 Comparison with Various Theories

For Exp. 2, the friction factors were estimated from the experimental measurements as f_w = 0.017 and f_I = 0.016 (see previous section). The comparison of the predictions with the measurements was plotted in Figure 6.7.

The inviscid hydrostatic theory predicts that the internal energy remains constant throughout the channel. Given the channel is flat to the right of the sill (x = 0.25 - 1.0 L), the interface is horizontal in that region and $G^2 = 1$. The flow rate is overestimated by about 16 % compared to the measurements, see Table 6.1.

Table 6.1 Comparison of the predicted flow rate with the measurement for Exp. 2

	Inviscid hydrostatic	Viscous hydrostatic	Viscous Non-hydrostatic	Measurements
Flow rate $q*$	0.131	0.108	0.117	0.113
Compared with measurements	+ 16 %	- 4 %	+ 3 %	

When friction is included in the hydrostatic theory, the predicted flow rate is then reduced and the prediction is much improved with the predicted flow rate only 4 % smaller than the measurement. Given that the flow rate is decreased, the internal energy at the exit is increased while that at the sill crest is decreased to form sufficient energy difference to compensate for the energy loss due to friction, Figure 6.7(b). The internal energy decreases from the channel right hand exit towards left. With friction considered, the prediction of the interface position is much improved. The friction also causes the sill control to be shifted left to the point where S_f - S_0 =

0. The amount of the shift of the sill control is not significant, with $\Delta x \approx 0.006$ (0.6 cm), Figure 6.7(c). However, G^2 at the sill crest is reduced from $G^2 = 1$ to $G^2 = 0.89$. The exit control, on the other hand, still remains at the right exit of the channel.

When the curvature effects are also included, the flow rate is increased to about 3 % larger than the measurements. The internal energy is very well predicted, especially around the sill region. At the sill crest point, both $y_{xx} < 0$ and $h_{xx} < 0$, the streamline curvature causes a negative E_{NH}, (see Section 5.3). At the channel right exit region, however, E_{NH} is positive given $y_{xx} > 0$ and $h_{xx} = 0$. As a result, $E_H = E - E_{NH}$ decreases in the exit region, and increases in the sill crest region. This change of E_H enables the streamline to be smoothed and the passage of more flow. In the sill crest region, S_c is a positive value, see Figure 6.7, S_0 is then reduced to satisfy $S_f - S_0 - S_c = 0$, and the sill control is then shifted to the right, at $x \approx 0.01$ (1 cm), while G^2 at the sill crest is increased from 0.89 to 1.13. With both curvature and friction effects considered, the interface position and the internal energy were very well predicted, Figure 6.7.

The change of E_{NH} along the channel, predicted with both the friction and curvature effects considered, is plotted in Figure 6.8. The curvature effects are important in the sill region and less so in the exit region, while negligibly small in the middle of the channel. Also, the curvature effect in the exit region is relatively small compared to that in the sill region. The change of E_{NH} was also obtained from the viscous hydrostatic solution and plotted in Figure 6.8. In the exit region, the viscous hydrostatic solution has infinite interface slope when the flow approaches the exit control due to the finite S_f and zero S_0, see Eq. (6.6). This gives $E_{NH} \approx 0.08$ at the exit control, compared with $E_{NH} = 0.01$ when the curvature is considered. This large E_{NH} is not realistic since the sharp interface is smoothed by the curvature effects. This unrealistically large E_{NH} in the exit region also makes the iteration from the hydrostatic solution impossible. In the sill crest region, on the other hand, E_{NH} is relatively well approximated.

In summary, the frictional effects are important throughout the channel, while the curvature effects are important in the sill region and less so in the channel exit region, while negligibly small in the middle region of the channel. The inclusion of the frictional effects reduces the flow rate, and improves the prediction. The predictions of the interface position is also greatly improved when friction is included. The inclusion of both the friction and curvature increases the flow rate and further improves the prediction. With the frictional and curvature effects included, both the flow rate and the interface position are well predicted.

6.3.2 Comparison of Flow Rates

The effect of the Reynolds number on the flow rate was studied experimentally using different g' for the exchange flows over a sill of h_m = 8.0 cm. When g' increases, the velocity difference ΔU also increases, while the shear layer thickness δ does not change significantly since it is mainly a function of flow setup. Therefore when g' increases, both Re_L and the shear Reynolds number Re increase. This causes the wall and the interfacial friction factors to decrease, and the flow rate to increase. In Figure 6.9, the measured flow rates were plotted against g' for all the experiments with the same setup (Exp. 1 - 9). The flow rate is found to decrease when g' increases, as predicted.

Effects of different friction factors on the flow rate were studied theoretically using the hydrostatic and non-hydrostatic theories. The predicted flow rates for different friction factors, f_I and f_w, were expressed as a percentage of the inviscid hydrostatic prediction, and plotted in Figure 6.10. For friction factors ranging from 0.01 to 0.02 for the short channel with a sill, the flow rate is reduced by about 10 to 20 % when friction is considered. The flow rate is increased by about 6 % when curvature effects are considered. The amount of the increase due to the curvature effects does not change much with friction factors, since it is mainly a function of the experimental setup.

The flow rates were predicted for all the experiments and compared with the measurements in Figure 6.11. The friction factors used in the predictions were obtained experimentally: f_w was estimated from Figure 6.3 using the measured flow rate; and f_I was estimated from Figure 6.5 from the measured shear Reynolds number. The flow rates were then predicted using Figure 6.10. It is shown in Figure 6.11 that the flow rates are over-predicted when the friction and curvature effects are neglected. With friction considered, the predictions are much improved. With the curvature considered, the flow rate are increased and the predictions are further improved. Considering about 5 % error in the flow rate measurements, the predictions with both friction and curvature considered compare very well with the measurements. Note the above results are for the channel with *L/H* about 5. The flows in the field, though having much larger Reynolds number, can still have significant frictional effects since these channels usually have much larger *L/H*.

6.4 DISCUSSION

Effects of a sharp-ended channel

The channel used in our experiments has sharp ends. The advantage of this channel is that it forces the exit control to be at the channel right hand exit point by creating a sudden jump of S_0, (see Section 6.1.1). However, this channel could cause some other difficulties and its effects on the flow need to be studied. Here we will only look at the effects of the right hand exit since the left exit does not affect the maximal exchange flow.

At the channel right hand exit, the upper layer expands horizontally into the right reservoir when it flows out of the channel. There is an energy loss caused by this sudden increase of the channel width. However, this loss of the upper layer energy does not affect the controls of the exchange flows, though it requires additional energy in the right reservoir in order to drive the flow (see Section 4.2). For the lower layer, this sharp entrance causes the flow separation, and a stationary separation region is formed immediately after the flow enters the channel. The size of this region was investigated experimentally in Exp. 2, see Figure 6.12. It had a width of about 3 cm, and a length of about 16 cm, with the maximum thickness at about 6 cm from the entrance.

The effect of this separation on G^2 can be considered as follows. At the position of the maximal width of the separation, the interface height and flow rate were measured as $y^* = 0.75$ and $q^* = 0.113$. Thus $G^2 \approx 0.85$ when the effect of the separation is neglected. When the separation is considered, G^2 becomes 0.88, due to the decrease of the area of the lower layer. This change of G^2 will cause q to change by less than 2 % assuming a constant y, or will cause y to change by about 0.5 % assuming a constant q. Thus even though the size of this separation is relatively large, it has only small effect on the exchange flow. This is because in the separation region, $y_1/y_2 \approx \frac{1}{3}$, thus $F_1^2/F_2^2 \approx \frac{1}{27}$, and the dynamics of the lower layer does not affect the flow.

The sharp end and its accompanying separation also cause the lateral streamline curvature. This lateral curvature, however, only causes horizontal centrifugal forces. These forces do not contribute directly to our equations of motion which are derived from a vertical force balance. Flow separation will, however, lead to small error since the velocity variation across the channel will be less uniform. The effect will be assumed to be negligibly small and is beyond the scope of present study.

Relative importance of friction and curvature

It is of importance to be able to quantify the relative significance of friction and curvature effects for a given channel. This relative significance can be studied by considering the effects of friction and curvature on the internal energy. The change of the internal energy due to friction is in the order of $\sigma^{-\frac{1}{2}} f_w$, where f_w is chosen as the characteristic friction factor, see Eq. (6.3). The change of the internal energy due to curvature effects is E_{NH}, which has an order of

σ, see Eq. (5.29c). We can then define a parameter, γ, to quantify the relative significance of curvature and friction:

$$\gamma = \sigma^{\frac{3}{2}} / f_w, \tag{6.15}$$

When γ is much less than 1, friction is dominant; and curvature effect is dominant when γ is much larger than 1. The friction becomes more important when σ decreases, *i.e.*, the channel becomes relatively long. For our experimental flows, $\sigma \approx 0.07$, and $f_w \approx 0.015$, thus $\gamma \approx 1.2$, and friction and curvature have the same order of magnitude. This is confirmed from Exp. 2 where $E_{NH} \approx 0.04$ in the sill crest region, while $\Delta E_f \approx 0.06$ for the channel. Note however, the curvature effects are mainly localized in the sill region, while the friction effects are global along the whole channel.

Effects of friction factors

The importance of frictional effects is determined by the magnitude of friction factors, the type of the flows, and the kind of the channel. The change of the internal energy probably is the best indicator to study the effects of friction factors for a given flow and channel. Assuming a simplified flow in which $U_1 = 2U_2 = 2U$, $y_1 = y_2 = b = y$, and also $f_{w1} = f_{w2} = f_I = f_w$, except for the free surface friction ($f_s = 0$), the change of the internal energy due to friction can be expressed as

$$\Delta E = \sigma^{-\frac{1}{2}} \beta \cdot f_w \frac{U^2}{y}, \tag{6.16}$$

where $\beta = 14.9$ for exchange flows, and $\beta = 3.5$ for uni-directional two-layer flows. Now we can estimate the value of friction factor which might be important for exchange flows. Given that $E = y + \frac{1}{2}(U_2^2 - U_1^2) \approx O(y)$, a change of the internal energy which might be important is $\Delta E = 0.5$. Also the layer Froude number, U^2/y, has an order of one in the channel region. Thus an estimate for f_w can be obtained, $f_w = 0.03\ \sigma^{\frac{1}{2}}$. Any f_w larger than $0.03\ \sigma^{\frac{1}{2}}$ needs to be considered for exchange flows. For laboratory experiments of exchange flows where $\sigma^{\frac{1}{2}}$ is about 0.2, a friction factor larger than 10^{-3} has to be considered. For exchange flows in the field where $\sigma^{\frac{1}{2}}$ has an order of $O(10^{-2})$, friction is important even when f is in the order of 10^{-4}. The frictional effects are more important for small $\sigma^{\frac{1}{2}}$. For uni-directional flows, however, frictional effects are about four times less important than that for exchange flows.

Chapter 7

EXPERIMENTAL STUDIES ON HOLMBOE INSTABILITIES IN EXCHANGE FLOWS

The Holmboe instabilities observed in the experiments were discussed qualitatively in Chapter 4. Quantitative study of these Holmboe instabilities is presented in this chapter, and the results are compared with theoretical studies. The linear theory of Haigh (1995) using hyperbolic tangent functions for both the velocity and density profiles (simplified here as "the smooth profiles") is mainly used for the comparison. Haigh's theory with smooth profiles accommodates the effects of viscosity, diffusivity, and the finite thickness of the interfacial density layer. Comparison will also be made with the linear theory of Lawrence *et al.* (1991) using piece-wise linear velocity and two-layer density profiles (simplified as "the piece-wise linear profiles"). The chapter starts with a discussion of the growth rate of Holmboe instabilities in the experiments. This is followed by a presentation of the experimental measurements of the wave length and phase speed of these instabilities. The symmetric Holmboe waves are also studied, as well as the interaction of the positive and negative waves. The conditions under which Holmboe instabilities develop are examined at last.

In the following study, the parameters of experimental measurements were non-dimensionalized with respect to the shear layer thickness, δ, and the velocity, $\frac{1}{2}\Delta U$:

$$\alpha = 2\pi\delta/\lambda, \quad c^* = (c-\overline{U})/(\tfrac{1}{2}\Delta U), \quad t_s^* = t/T_s, \tag{7.1}$$

where λ is wave length, and α is non-dimensional wave number; $\overline{U}$ is mean velocity, and c is wave speed; $T_s = \delta/(\frac{1}{2}\Delta U)$ is a time scale related to the development of instabilities, and t_s^* is non-dimensional time. Parameters with stars are non-dimensional. In the following study, we are mainly concerned with non-dimensional parameters. Stars will be dropped when there is no confusion. Given typical values of $\lambda \approx 10$ cm, $\delta \approx 4$ cm, $\Delta U \approx 4$ cm/sec, the above parameters have a typical values of $\alpha \approx 2$, and $T_s \approx 2$ seconds.

7.1 GROWTH RATE OF HOLMBOE WAVES

The development of Holmboe waves was followed using wave characteristic plots, see Figure 7.1a. The initial growth of negative waves at the start of Phase II of the experiments was observed as negative waves being generated suddenly, seen as dark bands in Figure 7.1a. This large growth rate of the negative waves was due to the decrease of the interfacial density layer thickness and the existence of a large negative shift during that period, as discussed in Section 4.4. The growth of negative waves was also observed at a later period of Phase II when two existing negative waves (Wave A and B) moved apart, (Figure 7.1b). This is because the mean velocity $\overline{U}$ is smaller at A than at B, (Figure 4.8 for Exp. 4), thus Wave A has a smaller absolute speed, $c_r^- + \overline{U}$, than Wave B. As a result, the distance between the two waves increased, and a new negative wave (Wave C), is generated when that distance exceeded some critical level. This is how Holmboe waves were generated at the later stage of the experiments.

The growth rate of negative waves can be estimated by following their development. The development of a newly generated negative wave (Wave C) was shown in Figure 7.2 after removing the mean interface position. The wave amplitude (seen as negative values for the negative wave) increased with time when the wave was growing, while it was also affected by the interactions with positive waves and complicated by other interfacial disturbances. The wave grew from approximately two to seven pixels (about 0.2 to 0.7 cm) and became fully developed in $t_s^* \approx 10$ ($t \approx 20$ seconds).

The growth rate was estimated assuming the waves had exponential growth rates, as is true for the initial growth (or linear growth) of Holmboe waves, (see Lawrence *et al.* 1991 or Haigh

1995). Given the exponential growth of the amplitude a, $a = a_0 \exp(\alpha c_i (t - t_0))$, the growth rate αc_i is estimated from the measurements of the wave amplitudes at different times using

$$\ln(a) = \ln(a_0) + \alpha c_i (t - t_0). \tag{7.2}$$

In Eq. (7.2), a_0 is the amplitude of negative waves at time t_0, and the growth rate αc_i is the slope of $\ln(a)$. The initial growth rate αc_i for Exp.4 was estimated to be about 0.1 (sec^{-1}) from Figure 7.2. With $\delta \approx 4.3$ cm and $\Delta U \approx 4.2$ cm/sec, measured at the time of the instability, the time scale $T_s = \delta / (\frac{1}{2} \Delta U) \approx 2$ seconds, and the non-dimensional growth rate $\alpha c_i \approx 0.2$. The growth rate decreased gradually when wave amplitude increased. After a period of about $\Delta t_s^* \approx 10$ (20 seconds), the negative wave was fully developed. Note, however, the linear growth rate of negative waves could be different from the above measurement, since the waves may not be in their initial linear developing stage when they are observable.

Other observations also showed that the growth rates of negative waves are in the order of $O(10^{-1})$. For the negative waves in Figure 7.1a, they completed their growth in a period of $\Delta t_s^* \approx 10$ ($\approx$ 20 seconds). Given the similar developing time, this growth rate was comparable with the above measurement of $\alpha c_i \approx 0.2$. These measurements were compared with the numerical predictions of the linear theory of Haigh (1995), where the closest case to our flow is the one with $R = 8$, $Pr = 64$ and $Re = 1200$. For the flow in Figure 7.1(b), where $J \approx 0.4$ and $\varepsilon \approx 0$, a wave growth rate of 0.13 is predicted. This prediction compares well with the measurement of 0.2. The difference is mainly due to the difference in the ratio R, as $R \approx 15$ in the experimental flow. The growth rate usually increases with the R, (see Haigh 1995), and when $R = \infty$, as for the inviscid piece-wise linear profiles, the growth rate is then predicted as to be about 0.26 (Lawrence *et al.* 1991). Considering the relatively low resolution of the current measurements, the above comparison is fairly good.

Note that the waves become fully developed in a period of 10 T_s (20 seconds), which is one order less than the evolution of the flow with an order of $O(10\ T_H)$ (about 150 seconds), given

$T_H \approx 7.5\ T_s$ in Exp. 4. Thus the flow conditions can be assumed as steady during submaximal exchange, and the temporal unsteadiness of the flow is not important in this study of interfacial instabilities.

Besides the unsteadiness, the flow conditions also changed with location in the experiments. Since waves could originate in one region and propagate into another where the flow conditions were different, the study of the interfacial waves could be very difficult. For negative waves, the effects of this change of the channel conditions were small since these waves were mainly generated in the middle region where the change of the flow conditions was gradual. These waves also propagated very slowly relative to the channel (see Section 4.4). Besides, these waves had a large growth rate and responded quickly to the local flow conditions given $\varepsilon < 0$ (see Figure 4.5). Therefore, the negative waves could be regarded as locally generated. The positive waves, however, were generated in the sill region and propagated into the middle region. In the middle region, where $\varepsilon < 0$, the growth rate for positive waves was small, thus the positive waves were less affected by the local flow conditions. Later in the experiments, the shift approached zero, and the positive waves could be affected and finally determined by the local flow conditions. As the positive waves might be non-local and the growth rate was relatively small, the initial linear growth rate of the positive waves was difficult to obtain and are not discussed in this study.

During the experimental process, the flow conditions changed, so did the growth rate of interfacial instabilities. When J increased or Re decreased, the growth rate gradually decreased. Unlike the prediction of inviscid theory where Holmboe waves can be observed no matter how large J is, the waves were stabilized and the interface became stable when J exceeded certain value due to viscous forces. This happened at later period (Phase III) of the experiments.

7.2 WAVE LENGTH AND WAVE SPEED OF HOLMBOE WAVES

The wave length and wave speed for both the positive and negative waves were measured from the wave characteristic plots. The wave speed was relatively stable and could be easily determined. The determination of the wave length, however, poses some difficulties, due to various interfacial disturbances. In case of difficulties, FFT analysis was also used. The measurements were compared with the predictions for the waves with fastest growth rate using the linear theory of Haigh (1995).

7.2.1 Negative Waves

The wave numbers, α, of the negative waves were measured for Exp. 2 and Exp. 4, and plotted against time and the Richardson number J in Figure 7.3. The wave number was relatively constant in the maximal exchange region ($t^* < 22$). It then increased as J increased in sub-maximal exchange. Given that the shift changed from about - 0.25 to 0 during the experiments, (see Figure 4.5), the predictions of the waves having the fastest growth rate were also made using the linear theory of Haigh (1995) for the flow with $\varepsilon = -0.25$ and 0. These predictions, together with the predictions of the stability boundaries were plotted on the α - J plot, and compared with the experimental measurements, Figure 7.3. Given the change of the shift, the predicted wave number changed from the line for $\varepsilon = -0.25$ gradually to the line for $\varepsilon = 0$. In general, the comparison was quite good, with all the measurements well within the unstable region predicted by the linear theory. All the measurements, except those at Phase III ($t^* > 50$), were very well predicted by the linear theory. The measurements from Phase III ($t^* > 50$) showed that the wave numbers were larger than the predictions. This is probably caused by the dominant viscous effects at this stage, which stabilized the waves.

In the above predictions, $R = 8$ was used, instead of $R \approx 15$ as measured in the experiments. The effects of this different R needs to be studied. Nishida & Yoshida (1990) computed the wave numbers for the fastest growth waves for inviscid flow with $R = \infty$ and $\varepsilon = 0$. Their results are also plotted in Figure 7.3. It is seen from the figure that when R increases, the predicted wave number gets larger. Nevertheless, the difference was relatively small, and the effects of R (when $R > 8$) on wave speed and wave length are not significant.

The measured wave speeds of negative waves, c_r^-, were plotted against time and the Richardson number in Figure 7.4. The wave speeds were affected by the change of both the shift and the Richardson number during the experiments. Linear stability theory predicts that negative waves speed up when ε changes from - 0.25 to 0 or J increases, (Haigh 1995). The predicted wave speeds fall in the region bounded by two predicted lines for $\varepsilon = -0.25$ and $\varepsilon = 0$, with wave speeds gradually approaching the line for $\varepsilon = 0$ as ε approaches zero with the experimental process. The measurements were generally in agreement with the predictions, with the wave speed c_r^- changing from about - 0.3 to - 0.4. But the difference was also noticeable, as the negative waves propagated slower than the linear predictions by about 0.1 to 0.2.

7.2.2 Positive Waves

The measured wave number for positive waves was plotted with time and the Richardson number in Figure 7.5. Linear predictions of Haigh (1995) were also plotted for the wave number with the fastest growth rate for the flow with $\varepsilon = -0.25$ and $\varepsilon = 0$. Also plotted in Figure 7.5 were the stability boundaries for the flow with $\varepsilon = 0$. The measured wave numbers were well within the predicted unstable region. However, it was found that the measurements of the early period of the experiments fell out of the region bounded by the predicted lines for $\varepsilon = -0.25$ and $\varepsilon = 0$, with the measured wave numbers smaller than the predictions. This is because the growth rate for the positive waves in the middle region was small due to $\varepsilon < 0$ during the initial period of the experiments. Thus the positive waves originated in the sill region were not affected significantly by the flow in the middle region where the flow conditions were measured. At the later period of Phase II, (t^* > 40), the shift was relatively small, and the growth rate of the positive waves increased. In this period the positive waves were affected and gradually determined by the local flow conditions, and the stability theory can be used to predict the flow using the measured flow conditions. This is confirmed as the measured wave number at the later period compared well with the linear prediction. Note at the this stage, the viscous effects were becoming important, and thus could also affect the waves.

In order to understand these non-locally generated positive waves observed in the early period of the experiments, the flow conditions in the sill region were measured. In the sill region, the shear remained strong during the early period of the experiments, with J increasing only slightly with time from 0.2 to 0.3, see Figure 4.6. The observed positive waves were generated in the sill region and their wave numbers were generally maintained when they propagated into the middle region. With this considered, the measured points for the early period of the experiments in Figure 7.5(b) should be lowered to J about 0.2 to 0.3. Thus the fact that measured wave number for the positive waves was smaller than the prediction is explained. The fact that the wave number for the positive waves was relatively constant for a longer period ($10 < t^* < 40$), Figure 7.5, than that for the maximal exchange flow ($10 < t^* < 22$) is also due to relative stable J in the sill region and the fact that positive waves were generated in that region and little affected by the flow in the middle region. The detailed study of this non-locally generated waves is beyond the scope of this study.

The measured wave speed for the positive waves decreased with time, (Figure 7.6), even though J increased meantime which would suggest otherwise (Haigh 1995). This is because the shift decreased and slowed down the wave speed significantly. The predicted wave speed of positive waves for different J were plotted in Figure 7.6 for $\varepsilon = -0.25$ and $\varepsilon = 0$, using the linear stability theory (Haigh 1995). The predicted wave speed changes from 0.65 to 0.45 when ε changes from -0.25 to 0 while $J = 0.2 \sim 0.7$. In general, the measurements compared well with the linear predictions, with the wave speed decreasing from about 0.65 to 0.4. At the later stage when $\varepsilon \approx 0$, the predicted wave speeds were smaller than the measurements by about 0.1. Similar findings were also obtained for the wave speed for negative waves.

Effects of the boundaries of the flow field

In the experiments, the upper layer was about twice as thick as the shear layer δ, while the lower layer was about four times as thick. It had been shown that limited layer thickness increases the growth rate of waves with small wave number, while suppresses those with large wave number, (see, for examples, Hazel (1972) and Haigh (1995)). Thus, the positive waves with smaller wave number are amplified. This might be responsible for the observation that wave number is slightly smaller than the linear prediction. Nevertheless, for our experimental flows where the upper layer thickness is reasonably large ($y_1 \approx 2\ \delta$), this effect is not significant. For the lower layer ($y_1 \approx 4\ \delta$), the wave number of the negative waves was less affected.

7.2.3 Relationship Between the Shift and Wave Speed

The wave speeds for the positive and negative waves are directly related to the amount of the shift of the density interface from the shear center. A simple explanation for this is shown in Figure 7.7. When $\varepsilon = 0$, the critical layers, *i.e.*, $u(z) = c_r^{\pm}$, happen at symmetric points (points A and B) and $|c_r^+| = |c_r^-|$. When the density interface moves upwards, *i.e.*, $\varepsilon < 0$, the critical layer in the upper layer is pushed upwards, while the critical layer in the lower layer is raised, (from points A to A' and B to B', respectively), thus $|c_r^+| > |c_r^-|$. Therefore the shift is related to the relative speed of the positive and negative waves. Lawrence *et al.* (1991) showed that for piece-wise linear velocity and two-layer density profiles, the contour lines for c_r^+ and $-(c_r^- + \varepsilon)$ coincide on stability diagrams, (see Figure 2.7). Given this relationship, a rough estimate of the shift could be made using

$$\varepsilon = -(c_r^+ + c_r^-). \tag{7.3}$$

An estimate of ε for Exp. 2 using the measured wave speeds was compared and plotted in Figure 7.8. The fact that $\varepsilon < 0$ is well predicted from the fact that the positive waves were moving faster than the negative waves, *i.e.*, $c_r^+ + c_r^- > 0$. The decrease of the shift in the experiment is also well predicted with the wave speeds for the positive and negative waves approaching each other. Given the simplicity of Eq. (7.3) and many assumptions involved, the above prediction is surprisingly good.

Some of the shortcomings of Eq. (7.3) need to be commented. For given flow conditions, *i.e.*, J and ε, the predicted wave speeds for the positive and negative waves with the fastest growth rate could fall on different contour lines, see Figure 2.7. Thus Eq. (7.3) is only an approximation. Furthermore, Eq. (7.3) is obtained from the linear stability theory with piece-wise linear profiles, and based on the assumption that the waves with the fastest growth rate are most likely to be observed. Nevertheless Eq. (7.3) proved to work well.

7.3 SYMMETRIC HOLMBOE WAVES AND WAVE INTERACTION

Symmetric Holmboe waves

For Exp. 9, the shift decreased to zero when $t^* > 40$. Thus, the growth rate of the positive waves increased and both the positive and negative waves had the same growth rate. With the symmetric flow conditions, *i.e.*, $\varepsilon = 0$, symmetric Holmboe waves are expected where the positive and negative waves have the same growth rate and propagate at about same speeds in opposite directions. These symmetric Holmboe waves were indeed observed in the experiments. A clear realization of this symmetric Holmboe wave was shown in Figure 4.8(b). This realization of symmetric Holmboe waves is important because it is often very difficult to obtain the symmetric flow conditions, (Lawrence *et al.* 1991). The detailed measurements for these Holmboe waves were presented in Table 7.1, and compared with the prediction of the linear theory with smooth profiles (Haigh 1995). Also presented in bracket are the predictions using the theory with piece-wise linear profiles (Lawrence *et al.* 1991).

Table 7.1 Comparison of Measurements and Predictions for Symmetric Holmboe Waves

	Wave Number		Wave Speed		Shift
	Positive	Negative	Positive	Negative	
Prediction	2.6 (2.2)	2.6 (2.2)	0.48 (0.47)	-0.48 (-0.47)	0
Measurements	2.2 - 3.1	2.2 - 2.9	≈ 0.3	≈ -0.3	0

The measurements of Holmboe waves were taken from Exp. 9 at $t^* \approx 40$. The flow conditions are as follows: $R \approx 15$, $g' = 1.6$ cm/s^2, $\overline{U} \approx 0.4$ cm^2/s, $\Delta U \approx 4.2$ cm/s, $\delta \approx 5.0$ cm, thus $J = 0.45$ and $Re = 1800$. Predictions were obtained using the linear theory of Haigh (1995), and linear theory of Lawrence *et al.* (1991). The later are shown in bracket.

From Table 7.1, we see both the positive and negative waves had approximately equal wave length and equal wave speed with respect to the flow mean velocity. The fact that $\varepsilon \approx 0$ is also well predicted. The measured wave length was very well predicted by the linear theories, for both the positive and negative waves. The wave speed, however, was over-predicted by the linear theories, as was reported in Section 7.2 for Exp. 2 and Exp. 4. The difference in the predictions of the two theories were found to be small, though the theory with the piece-wise linear profiles predicts smaller wave number.

Wave interactions

One of the interesting phenomena of Holmboe waves is that wave speeds tend to vary when positive and negative waves pass through each other: waves speed up when they approach each other and slow down when they are far apart. This is first predicted by Holmboe (1962). This wave interaction has also been confirmed in linear and non-linear simulations (Smyth *et al.*

1988; Haigh 1995). The laboratory observation of this phenomena has not been reported so far. In the present experimental studies, this wave interaction was observed for the negative waves, see Figure 7.9. The wave speed fluctuated from about - 0.4 to - 0.2 around its mean value of - 0.3. The speed was fastest when the negative waves were further away from the positive waves, and slowest when they were passing through the positive waves. Unlike the negative waves, the wave speed for the positive waves remained quite constant and were less subject to the wave interaction.

The magnitude of the speed variations for negative waves also changed with the flow conditions. This speed variations were found to be more significant for the flow with $\varepsilon = 0$, and less so for the flows with $\varepsilon \neq 0$. These are probably due to the fact that the positive and negative waves originated at different places. When the flow was non-symmetric with $\varepsilon < 0$, the growth rate for the positive waves in the middle region was small. The positive and negative waves then had different wave characteristics, and were relatively independent from each other. When the shift decreased to zero, both the positive and negative waves had similar wave characteristics. Thus the interaction of the wave speed was observed. The reason that the wave speed of the positive waves was less variable is not clear, though it is conjectured that the origin of the positive waves might be partially responsible.

7.4 FLOW CONDITIONS FOR HOLMBOE INSTABILITIES

It is of interest to study the flow conditions for Holmboe instabilities. In the present study, the effects of J and Re on Holmboe instabilities are studied. The flow conditions for Holmboe instabilities were plotted on a (Re, J) plot for all the experiments, (Figure 7.10). There is a minimum value of Richardson number (J_{min}), for all the measured J, being about 0.3 to 0.4. This minimum value was related to the experimental setup since the forcing in our experiments was generated by the density difference, with $(\Delta U)^2 \propto g'$, thus $J = g'\delta/(\Delta U)^2 \propto \delta$. Thus J_{min}

is mainly a function of the experimental setup. For each experiment, the Reynolds number decreased and J increased during the experimental process. The flow finally became stable and wave activity decayed after J exceeded a certain value (J_{max}) for a given Re. An upper boundary for the instabilities was found from these measurements. This boundary changed with both J and Re: the flow was stabilized when J was larger than a critical value or Re is smaller than a critical value. From Figure 7.10, J_{max} was found to increase slightly from 0.7 - 0.85 (with an error of $\pm$ 0.1) when Re increased from about 1000 to 5000. This can be explained by the fact that viscous effects are more important when Re is small, thus stronger shear or smaller J_{max} is required to generate Holmboe waves.

The effects of viscosity on the Holmboe instabilities were studied numerically by Nishida & Yoshida (1987) using hyperbolic-tangent velocity profile and two-layer density profile. They found that the flow is stable when J exceeds a critical value of about 0.6 to 0.75 for the flow with a shear Reynolds number ranging from 200 to 4000. Their results are comparable to the experimental measurements of the present study, and the existence of a maximum value of J for Holmboe waves is confirmed for viscous flows. Aside from its effects on stability region, viscosity has little effects on the fastest growing waves when Re is larger than 1000, as has been shown by Nishida & Yoshida (1987) and Smyth *et al.* (1988).

The effects of Prandtl number on Holmboe instabilities were also studied using an experiment with thermally stratified flows (Exp. 5), *i.e.*, warm water and cold water. The interface was observed as diffused and stable to short wave instabilities (*i.e.*, no K-H or Holmboe instabilities), in contrast to the wavy interface of Exp. 4, (see Figure 7.11). Both experiments had similar ranges of Richardson number and Reynolds number, (for Exp. 4: $J \approx 0.32$ and $Re \approx 1800$, while for Exp. 5: $J \approx 0.32$ and $Re \approx 2100$, see Table 3.1), with the difference only in the thickness of the interfacial density layer. The Prandtl number for thermal diffusion ($Pr \approx 8$) (Haigh 1995) is much smaller than that for salinity diffusion ($Pr \approx 700$). The resulting R ($R \approx 2$) for Exp. 5 is therefore much smaller due to significant thermal diffusion. For such small R, Hazel (1972) and Haigh (1995) showed that Holmboe instability does not exist. Thus Holmboe instabilities were not observed for thermal stratified flows even though the flow conditions were comparable to those of salinity stratified flows. The shear stress in Exp. 5 is also not strong enough to generate K-H waves. Similar observations on thermally stratified flows were also reported in other studies, (Delisi & Coros 1973).

Stability conditions were studied using the Keulegan number, $K = (\Delta U)^3 / g' \nu = Re/J$, in some previous studies (Keulegan 1949; Grubert 1990). The onset of instabilities for a laminar flow, (as judged by the appearance of waves on the interface) was shown to depend mainly on K, and occurred when K exceeds a critical value of about 500 (Keulegan 1949). Here the Keulegan number is examined for the Holmboe instabilities observed in the present study. Given the J_{max} changed only slightly from about 0.7 to 0.85 when Re increased from about 1000 to 4000, the critical K then increased from about 1200 to 4000. Therefore there is no single critical K value for this instability study. Besides, the mixing layer thickness also affects the interfacial instabilities, thus the Keulegan number may not be an appropriate parameter for this study.

7.5 DISCUSSION

7.5.1 Effects of Non-linearity and Wave Deformation

The waves observed in the experiments were of finite size and are almost certainly non-linear. Thus the non-linear effects may need to be studied. The experimental observations showed that there was no noticeable difference between the fully developed and newly developing negative waves, in terms of wave speed and wave length, as seen from the wave characteristic plots, Figure 7.1. Thus non-linearity may not have significant effects on wave speed and wave length. This finding conforms with the non-linear simulation of Haigh (1995) where the wave speed is found to increase only slightly when waves are non-linear. No other theoretical studies are available for the non-linear development of wave length and growth rate. The experimental measurements of Lawrence *et al.* (1991) and Pouliquen *et al.* (1994) show that the observed wave length and wave speed compare well with the linear theories. Therefore linear theories can be applied even though the observed instabilities are no longer linear.

The fully developed Holmboe waves in our experiments have a typical amplitude of 0.5 to 0.7 cm with a typical wave length of about 10 cm, such as these observed at $t^* \approx 40$ in Exp. 9 where $J = 0.4$ and $Re = 1500$. Under certain conditions, some of these positive waves roll up while they are propagating, (see Figure 7.12). Even though they roll up like K-H waves, the Richardson number for the flow is still significantly large, about 0.3 to 0.5, much larger than that required for the generation of K-H waves ($J \approx 0.07$). Eventually, these waves break down. The observation of this wave deformation is important since these wave deformation is not expected for the flow with such strong stratification, and it significantly enhances interfacial mixing. Also shown in Figure 7.12 is the existence of two wave systems with different wave speeds. The reason for that is unclear.

7.5.2 Sources of Shift

The shift of the density interface from the shear center was found in many experimental studies. Keulegan (1949) observed the one-sided interfacial wave. Koop & Browand (1979), Lawrence *et al.* (1991) and Guez & Lawrence (1995) found that the shift was generated by a splitter plate. In the saline wedge flow, Yonemitsu (1991) showed that the shift was caused by secondary flows. More recently, the surface tension between two immiscible fluids was found to be the reason for the shift (Pouliquen *et al.* 1994). Due to the existence of the shift, the realization of pure Holmboe waves was found to be difficult.

Efforts have been made to find a way to predict the shift. Based on the development of boundary layers for two-layer shear flow, Lock (1951) found that the shift is possible when the two layers have different velocities. However, Lock's theory predicts a small shift of $\varepsilon \approx 0.1$ for the flow of Koop & Browand where the shift was measured to be about 0.5. Koop & Browand (1979) suggested that the shift might directly be related to the relative speed of two layers, with $\varepsilon > 0$ when flow has a faster moving upper layer. However, for our experimental flows, $\varepsilon < 0$ is found even though the flow has a faster moving upper layer. Thus, to relate the shift solely to the relative speed of two layers is probably over-simplifying the problem.

The cause for the initial significant shift is not clear so far, though it is believed to be related to the experimental setup and general flow conditions. For our experiments, the existence of the sill might break the symmetry of the flow and cause the shift. Though there are not enough measurements to study the effects of the sill size on the shift, we postulate that a larger sill will cause stronger asymmetry of the velocity field and thus lead to larger shift. The shift decreases with the experimental process as the flow gradually adjusts itself. In the late stage of experiments, the interface drops and the velocity difference between the two layers decreases. Thus the mean velocity decreases to zero, and the asymmetry of the flow velocity also reduces, as does the shift.

Chapter 8

TWO-LAYER FLOWS OF CONCERN TO CIVIL AND ENVIRONMENTAL ENGINEERS

The study of two-layer flows is important in the understanding of the environmental impact of human activities and engineering works. One example is the intrusion of excessive salinity into the Sacramento-San Joaquin Delta in California resulting from the decreased river outflow following massive river diversions and extensive fresh water usage (Conomos 1979). An engineering initiative to reduce the saline intrusion by building an underwater sill is studied in Section 1. Section 2 discusses the factors affecting the dispersion and diffusion of pollutants in estuaries, namely, saline wedges and interfacial mixing. Section 3 presents further examples where exchange flows are important in pollution remediation and engineering works.

8.1 EXCHANGE FLOWS THROUGH CARQUINEZ STRAIT

The increased usage of fresh water and massive river diversions from the upper Sacramento and San Joaquin River systems have resulted in an excessive saline invasion into the Sacramento-San Joaquin Delta, Figure 8.1, (Conomos 1979). In an effort to arrest landward salt-water intrusion, an underwater sill was proposed to be built in the Carquinez Strait (US Army Corps of Engineers 1980). The sill would inhibit the intrusion of salt water allowing more fresh water to be diverted to the dry region of southern California without the harmful effects of increased saline intrusion. The Carquinez Strait has a relatively constant width along its length, and the width only increases at both ends when the strait joins the more saline San Pablo Bay to the west and the fresher Suisun Bay to the east. The depth of the strait at both ends is about 13 to 14 m, while it deepens to a maximum of 27 m within the channel. The fluids in both bays are generally well mixed, and the density difference is of order of $15\sigma_t$, where ρ in kg/m^3 is 1000 + σ_t. Depending on the magnitude of river runoff and on the tide, a two-layer exchange flow can form in the Carquinez Strait.

The exchange flow through the Carquinez Strait is studied here by assuming a rectangular cross-section of 900 x 13 m, and a length of 8700 m. Some assumptions are made to simplify the problem, since we are interested in the basic dynamics of the flow. We assume the flow is quasi-steady, and the effects of the bending of the strait is negligible. We also assume the effect of depth variation is small. The later is partially justified as the flow is actually determined by the two controls at both ends, where the depth is about 13 ~ 14 m. The deep part can be considered to form a dead water body, and does not affect the dynamics of exchange. The non-hydrostatic effects are also neglected as they are small for a straight channel with a constant depth (Zhu & Lawrence 1996b). In the following, we will first study the effects of friction on the exchange flow. We then investigate the effects of different sizes of the sill.

8.1.1 Effects of Friction

For a straight channel with a flat bottom, the internal energy is conserved along the channel when friction is neglected, and $G^2 = 1$ everywhere. Thus the interface is horizontal and located at $H/2$, where H is the channel depth, and the non-dimensional flow rate $q^* = q/\sqrt{g'H^3}$ = 0.25. However, friction could significantly reduce this rate of exchange (see Section 6.3). Here we incorporate both wall and interfacial friction in the prediction of the exchange.

The wall friction factor for the Carquinez Strait is estimated using Manning's equation with n = 0.025 for a clean straight river channel (Henderson 1966). It is also estimated using the boundary layer theory for the turbulent shear flow passing a plate with a roughness of k = 0.2 m (White 1991). These predictions are compared with the suggested values for other channels or straits in Table 8.1. An averaged wall friction factor, f_w = 0.005, is then chosen for this study. Given this friction factor, the Carquinez Strait is a long channel as $f_w L / H = O(1)$ (see Pratt 1986), and the effect of friction must be considered.

Table 8.1 Estimates of bottom friction factor f_w for the Carquinez Strait

	f_w (x 10^{-3})	Note
Pratt (1986)	2.0	Strait of Gibraltar
White (1991)*	4.0	Carquinez Strait
Oguz *et al.* (1990)	4.6	Bosphorus Strait
Smith & McLean (1977):	5.2 ~ 6.0	Columbia River
Geyer (1985)	6.0	Fraser River
Hamblin & Lawrence (1990)	6.0	Burlington Ship Canal
Henderson (1966)**	6.6	Carquinez Strait
Grant et al. (1984)	8.8	California shelf

*: Estimated at the middle of the Carquinez Strait, with Q = 663 m^3/s (averaged flow rate) and k = 0.2 m. See P. 434 of White (1991).
**: Estimated using Manning coefficient n = 0.025.

The maximal exchange through the Carquinez Strait with two exit controls is predicted for different interfacial friction factors while keeping f_w = 0.005, see Figure 8.2a. The interfacial friction factor f_I is predicted using various proposed methods, and the results are plotted in Figure 8.2a. For different predictions of f_I, the flow rate changes significantly. For example, when f_I changes from 0.0002 to 0.0024, the flow rate is reduced by about 40 % from 0.124 to 0.074. The effects of interfacial friction is thus important, and a better prediction of the interfacial friction factor is desired.

With f_w = 0.005, and f_I = 0.0012, (the mean value from the various predictions shown in Figure 8.2a), the predicted flow rate for the maximal exchange is then q^* = 0.091. This is much larger than the averaged river runoff of q^* = 0.041 (663 m^3/s), obtained from an annual discharge of 19.0 x10^9 m^3 (Conomos 1979). The river discharge changes from about 100 m^3/s in the dry season to more than 10,000 m^3/s in flood flow. During the dry season, the river runoff is not sufficient to maintain the control at the east exit. Under these conditions the flow is submaximal exchange, and during this time the saline intrusion is at its maximum. One way of restricting this saline intrusion is to build an underwater sill in the strait. With such a sill, the amount of fresh water needed for maximal exchange flow is reduced and the excessive saline intrusion is restricted.

8.1.2 Effects of Different Sizes of the Sill

We now study the effects of building an underwater sill in the strait. The sill site is proposed at the east exit region of the channel at the Suisun Bay side. With the distance between the sill and another control (the west exit) being the furthest, the effect of friction is at its most in reducing the flow rate. Besides, the strait is shallow at this site with a depth of about 13 m, the construction is relatively easy with small amount of earth work involved. A sill with a shape of $h = h_m \cos^2(x / 2h_m)$ with $|x / 2h_m| \le \frac{\pi}{2}$ is used in the following prediction. Such a shape is smooth for a relative short length: for a sill with a height of h_m, it has a total length of about $6h_m$, (see Section 3.1).

Assuming the friction factors to be $f_w = 0.005$ and $f_I = 0.0012$, the flow rates for maximal exchange are predicted for different sizes of the sill, Figure 8.2b. The flow rate is reduced when the sill height increases. For a sill of $h^* = 0.5$ ($h_m = 6.5$ m), the flow rate is reduced by about 50 % to $q^* \approx 0.04$. Such a sill might be most suitable to reduce the intrusion as it reduces the flow rate for maximal exchange to the same level as the averaged river runoff $q^* = 0.041$. With the exchange flow being maximal most of the time, the saline intrusion is most effectively restricted.

The flow rate for the maximal exchange can also be reduced by narrowing the width of the channel at the exit. While this option needs to be explored further, it is less effective in reducing the saline intrusion than using a bottom sill. Detailed environmental studies of this proposed work are needed, especially on the hydrographic and ecological conditions in San

Francisco Bay and the Sacramento-San Joaquin Delta due to the reduction of the fresh water runoff. The effects of jet flow formed down the proposed sill on fish migration and other biological communities in the Delta area also need to be considered. These studies also require a better understanding of two-layer exchange flows.

8.2 SALINITY INTRUSION IN THE FRASER RIVER

Salinity intrusion is of obvious importance in the study of estuaries, as it affects the intake of fresh water for municipal, industrial and agriculture uses. The understanding of salinity intrusion is also important in many environmental engineering problems, such as the design of sewage treatment plants. The dispersion and diffusion of pollutants such as discharged sewage are usually affected by saline wedges and the interfacial mixing between the fresh and saline water (Hodgins 1974). The effects of the saline wedge in the low reach of the Fraser River, British Columbia, on sewage discharge is being studied for the upgrade of the Annacis Island sewage treatment plant (Hodgins & Mak 1995).

The main unknown in determining the intrusion length of a saline wedge is the interfacial friction factor. Using a simple one-dimensional model, the maximum intrusion length of an arrested saline wedge is inversely proportional to the interfacial friction factor (Sargent & Jirka 1987). Despite its importance, the prediction of the interfacial friction factor remains difficult. As shown in Figure 8.2a, the predictions of f_I can vary by about ten times, resulting a ten times difference in the intrusion length. The uncertainty in predicting f_I mainly comes from a poor understanding of the interfacial flow conditions and interfacial instabilities. Our experimental studies show that interfacial instabilities increase the interfacial friction factor by about ten times compared with that for laminar flows (see Section 6.3). Thus a better understanding of interfacial instabilities is desired in order to provide better predictions of interfacial friction factor.

Interfacial mixing is also important in the dispersion of pollutants. Experimental studies show that mixing is significantly enhanced by interfacial shear instabilities, with the vertical transport rate increasing by one to two orders compared with the molecular diffusion (Moore & Long 1971). Some field studies of shear instabilities were conducted by Seim and Gregg (1994) in Admiralty Inlet, a 30 km long, 70 m deep tidal channel connecting the fjord-like estuary of Puget Sound to the Strait of Juan de Fuca. Owing to considerable river runoff into Puget Sound, a strong mean two-layer exchange flow exists in Admiralty Inlet. Shear instabilities were observed near the hydraulic control at a contraction in the width. The flow experiences a rapid acceleration as it passes by the contraction, and large scale Kelvin-Helmholtz billows with a wavelength of 70 m and height of 10 m were observed. These billows eventually break down and cause significant turbulent mixing. Interfacial instabilities were also observed in the Fraser River (Geyer 1985), and the Strait of Gibraltar (Armer & Farmer 1988).

Besides the K-H waves, one-sided Holmboe waves with sharp cusps were also observed by Seim and Gregg (1994). The shift of the density interface from the shear center was measured and this shift is believed to be the reason for the one-sided Holmboe instabilities. The measurements made by Yoshida *et al.* (1995) in a strongly stratified estuary rivers also reveal the displacement of the velocity and density interface. This displacement resulted in the one-sided Holmboe waves observed in their study.

Though there are only limited field studies on interfacial instabilities due to measuring difficulties, the important role these instabilities play in generating turbulence and vertical mixing is obvious. The understanding of the mixing due to interfacial instabilities is also important in many other engineering problems, such as the safe disposal of mine tailings in aquatic systems, the vertical transport of mine tailing in pit-lakes (Stevens *et al.* 1995), and the entrainment of the mud in the fluid-mud and water interface (Mehta & Srinivas 1993).

The study presented in this thesis will contribute towards a better estimate of interfacial friction of two-layer flows. Using the numerical schemes developed in this study, two-layer flows can be predicted with the effects of friction and channel topography considered. Hence better estimates of flow rate and/or intrusion length can be obtained.

8.3 OTHER EXCHANGE FLOW PROBLEMS

The remediation of the pollution of Hamilton Harbor requires a better understanding of the exchange flows between the harbor and Lake Ontario. Exchange flows also need to be studied in building a bridge and tunnel system across the Great Belt in Denmark, and a rail tunnel across the Bosphorus in Turkey, in order to prevent the adverse effects on the environment.

8.3.1 Exchange Flow Through Burlington Ship Canal

The heavy polluted Hamilton Harbor is connected to Lake Ontario through Burlington Ship Canal (Hamblin & Lawrence 1990). Understanding of the exchange through the canal is important in the remediation of Hamilton Harbor. The canal has a dimensions of 836 x 89 x 9.55 m. In the summer time, exchange flows form through the canal with warmer Harbor water in the surface layer, and cool Lake Ontario water in the bottom layer. The exchange is controlled by the exits at each end. With a relative large *L/H* ratio, friction is important in predicting the flow rate. For example, with the typical summer temperature in Hamilton Harbor and Lake Ontario being 20 °C and 10 °C respectively, compared to the inviscid case the flow rate is reduced by about 40 % when $f_w = 0.005$ and $f_I = 0.002$ are chosen. The uncertainly in predicting f_I also causes significant differences in the flow rate. The predicted flow rate changes from 60.0 m^3/s to 48.2 m^3/s when two possible values of f_I, 0.0002 and 0.0028 are used while $f_w = 0.005$. This difference in flow rate is more than the total Harbor inflow of about 8 m^3/s from tributaries and municipal sewage.

8.3.2 The Great Belt Link

The Great Belt is a broad and shallow strait approximately 18 km wide in Denmark (Moller *et al.* 1994). It is the largest of the three straits linking the fresher Baltic to the saline North Sea. A major construction project (the Great Belt Link) is now underway to build a rail and tunnel system across the Great Belt. Changes in the flow conditions due to the Link will influence the hydrography of the Baltic Sea. The aquatic environment of the Baltic Sea is a sensitive brackish ecosystem which is strongly dependent on the supply of oxygen rich, saline water from the North Sea through the Danish straits. Environmental concerns prompted the Danish government to decree that the construction of the Link should not block the exchange flow between the North Sea and the Baltic Sea. An understanding of the hydraulics of exchange flows is then essential in the design of the Great Belt Link in Denmark to avoid a reduction of the exchange flow (Ottesen-Hansen & Moeller 1990).

The Link is chosen at a shallow narrow section of the Great Belt. The exchange flow can be modelled as the flow over an underwater sill, and is sensitive to the cross-section area of the channel. For economic reasons, causeways are built in areas of water depth less than 6 m, while a bridge and a tunnel are built in deep areas. The blockage of these causeways and bridge piers shall be compensated by increasing the flow cross section of the link by dredging. Thorough hydrodynamic investigations of this exchange flow over a sill with a contraction needs to be conducted before the location and the amount of dredging can be determined in order to achieving high hydraulic efficiency.

8.3.3 Exchange Flow Through the Bosphorus

The Bosphorus is a strait in Turkey, connecting the Black Sea and the Marmara Sea. It is a narrow shallow channel, with a length of about 31 km, an averaged width of 1.3 km, and a depth ranging from 30 to 100 m. The water in the Marmara is more saline than that in the Black Sea by about $20\sigma_t$. A two-layer exchange flow forms within the strait with a heavy salty layer flowing from the Marmara to the Black Sea and lighter more brackish layer flowing in the reverse direction. This two-layer flow in the Bosphorus is controlled by the critical sections at both ends (Oguz *et al.* 1990). With a ratio of *L/H* being about 1000, the Bosphorus is classified as long with friction being important.

A railway tunnel is to be build across the Bosphorus. The proposed location of the tunnel is in the narrowest section of the strait, which coincides with the critical section at the southern entrance. The building of the railway tunnel may significantly affect the flow system of the Bosphorus. Among them, the most important influence may be on blocking phenomena. The effects of the reduction of the cross-section on the exchange need to be studied.

The understanding of interfacial instabilities and mixing of the exchange flow is also important in the design of marine outfall, as there is speculations that the pollutants discharged through the Istanbul Sewerage Systems into the lower layer would be mixed with the flow of the upper layer and transported back to the Sea of Marmara. The study of the Bosphorus can also applied to other sea straits, such as the Dardanelles Strait, which connects the Aegean Sea and the Marmara Sea (Oguz & Sur 1989).

Chapter 9

SUMMARY AND CONCLUSIONS

Exchange flows through a channel of constant width with a smooth two-dimensional underwater sill were studied theoretically and experimentally. The flow considered has gentle streamline curvature with $\sigma = (H/L)^2 << 1$, and the density difference is small. Hydraulic theory was extended to incorporate the effects of streamline curvature and the friction due to the channel sidewall, bottom and, the density interface. The Holmboe instabilities observed on the density interface were also studied experimentally.

9.1 EVOLUTION OF EXPERIMENTS

Evolution of the mean flow

Experiments of exchange flows through a channel with an underwater sill were conducted. The mean flow evolved through different regimes. After a short initial start-up period, the flow was maximal exchange with two controls: the sill control and the exit control. When the exit control was submerged due to the change of reservoir conditions, the flow then became submaximal and was controlled by the remaining sill control and the reservoir condition. The reservoir conditions to maintain the sill and/or exit control were studied with the energy loss due to the channel exit considered. When both controls were submerged, the flow was then uncontrolled.

Evolution of interfacial disturbances

On the interface between the two layers, Holmboe instabilities were observed. The velocity profiles of the mean flow can be very well approximated by a hyperbolic-tangent function. The interfacial density layer was thick initially, with $R \approx 2$, due to initial mixing. It then decreased quickly with $R \approx 10 \sim 15$ during the majority of the experiments. The shear Reynolds number decreased from a couple thousand at the start of the experiment to about 1000. Holmboe instabilities were only observed when R was significantly large, $R >> 2$, while J was less than a critical value of about 0.8.

The mean velocity, $\overline{U} = \frac{1}{2}(U_1 + U_2)$, of the exchange flow changed along the length of the channel, and affected the propagation of interfacial waves. Based on the wave propagation, the channel could be divided into three regions: the sill region (x = 0 - 0.3 L), the middle region (0.3 - 0.8 L), and the exit region (0.8 - 1.0 L). The negative waves generated in both the sill and exit region were prevented from propagating into the middle region. Thus the negative waves observed in the middle region were locally generated. The positive waves, however, were mainly generated in the sill region, where the shear was stronger, and propagated towards the right. In the present study, the Holmboe instabilities observed in the middle region were studied.

The density interface was found to be shifted from the shear center. Significant negative shift ($\varepsilon \approx$ - 0.25) was measured in the early period of the experiments. This negative shift gave the negative waves much larger growth rate. The growth rate of the positive waves in the middle of the channel was relatively small. As a result, the negative waves were more visible. As the experiments progressed the shift decreased gradually to zero, and the symmetric Holmboe waves were observed.

9.2 EFFECTS OF CURVATURE

Steady multi-layered flows over a smooth two-dimensional sill are considered. The flow considered has gentle streamline curvature with $\sigma = (H/L)^2 << 1$, and the density difference between layers is small. Hydraulic theory is extended to incorporate the effects of streamline curvature. While the hydraulic theory gives the first order accurate $O(\sigma)$ pressure and layer energy, the extended theory gives the second order accurate $O(\sigma^2)$ pressure and layer mechanical energy. Unlike some other studies, no restriction is placed on the size or shape of the sill as long as the sill is smooth. This approach is applicable to finite size sills and to flow problems with any number of layers.

For single-layer flow, the extended theory reproduces the results of Naghdi & Vongsarnpigoon (1986). Unlike their method which is not readily expandable to multi-layer flows, the extended theory can be applied to the problems with any number of layers. Naghdi & Vongsarnpigoon also failed to predict the flow due to numerical instability. We successful solved the problem by treating the problem as a boundary value problem (BVP). The predictions of the bottom pressure and the interface position compared very well with the experimental measurements of Sivakumaran *et al.* (1983).

The extended theory is also applied to two-layer approach-controlled flows. Hydraulic theory fails to predict approach-controlled flows since the curvature effects are too important to be neglected. Predictions of the extended theory compare well with the experimental measurements of Lawrence (1993).

9.3 EFFECTS OF CURVATURE AND FRICTION IN EXCHANGE FLOWS

Given frictional effects are also important in exchange flows, hydraulic theory is extended to include the effects of both the friction and curvature.

Wall and interfacial friction factors

For our experimental exchange flows, the flow in both the upper and lower layers accelerated in the downstream direction, and the boundary layers for the walls and the bottom were not fully developed. Hence Thwaites method was used to estimate the friction factors. The friction factors for such accelerating flows were significantly larger than those for non-accelerating flows by more than 50 %, with f_w ranging from about 0.01 to 0.02 where $Re_L = UL/\nu = O(10^3)$.

Interfacial friction factors, f_I, estimated from the experimental measurements, were found to decrease with increasing shear Reynolds number and Richardson number. f_I obtained from various experiments decreased from about 0.015 to 0.005, when the shear Reynolds number increased from about 1000 to 4000. The Reynolds stress was found to be the dominant component, composing about 80 - 90 % of the total interfacial shear stress, whereas the viscous part with responsible for the remaining 10 - 20 %.

Comparison with experiments

The maximal exchange flow was studied using the hydrostatic and non-hydrostatic theory with frictional effects. The flow was determined by controls at the sill crest and the channel right exit for inviscid hydrostatic flows. The location of the sill control was shifted when the effects of curvature and/or friction are considered. Its exact location depended on the flow conditions, the friction factors, and the sill shape. The amount of the shift of the sill control from the sill crest was not significant, but G^2 at the sill crest point changed significantly. This change in G^2 affected the prediction of the flow rate. The exit control, however, was forced to be at the channel exit for a constant width channel with a sharp end.

When friction was considered while curvature effects were ignored, the flow rate was reduced by about 20 % compared with the inviscid hydrostatic prediction. The internal energy was reduced monotonically from the channel right exit, and the interface profile became steep. The predictions were much improved with the flow rate and interface slope agreement in general with the measurements.

When the effects of both curvature and friction are considered, the internal energy is accurately predicted. The flow streamline curvature is smoothed, and the predicted flow rate is increased. The friction is important along the whole channel. The curvature effects are important in the sill region, less so in the exit region, and negligibly small in the middle of the channel. With both the curvature and frictional effects considered, there is excellent agreement between measurements and predictions.

9.4 HOLMBOE INSTABILITIES IN EXCHANGE FLOWS

Wave growth rate

Holmboe instabilities were studied experimentally for the exchange flows over a sill. The growth rate of Holmboe instabilities was measured by tracking the development of the negative waves in exchange flow experiments. The negative waves had an initial growth rate of $\alpha c_i \approx 0.2$. This growth rate compared well with $\alpha c_i \approx 1.3$, predicted using the linear stability theory of Haigh (1995). The difference is mainly due to the different R utilized in the theory and in the experiments. With such a significant growth rate, the waves became fully developed quickly.

Wave length and wave speed

Both symmetric and non-symmetric Holmboe waves were observed in the experiments. The wave length for the positive and negative waves compared well with the linear theory of Haigh (1995). The non-dimensional wave speed was in general agreement with that predicted using the linear theory, but they were consistently smaller than the linear prediction by about 0.1 - 0.2.

The wave speeds and the amount of the shift were directly related. When the shift was negative, *i.e.*, the shear center was lower than the density interface, the positive waves propagated faster than the negative waves. A simple relation, $\varepsilon = -(c_r^+ + c_r^-)$, suggested by Lawrence *et al.* (1991) was found to be consistent with the experimental measurements.

The variations of the wave speeds when waves passing through each other was observed in our experiments. Waves speeded up when they approached each other and slowed down when they were far apart, in consistent with theoretical predictions. While the wave speeds of the negative waves varied significantly, the wave speeds of the positive waves remained quite constant and were less subject to this wave interaction. Also the wave interaction was more significant in the flows with $\varepsilon \approx 0$, and less so for other flow conditions.

Flow conditions for Holmboe instabilities

The flow conditions for Holmboe instabilities were studied experimentally using a (Re, J) plot. The flow was stabilized when J exceeded some critical value, J_{max}, of about 0.7 ~ 0.85. J_{max} decreased slightly when Re increased from about 500 to 2000. The effects of the Reynolds number on Holmboe instabilities are not important when the Reynolds number is reasonably large, say, $Re > 1000$. Examined using the experimental measurements, the use of Keulegan number as a stability criteria was found to be unsuitable. Instead, the Richardson number provides a much better criteria for the generation of Holmboe instabilities.

The effects of Prandtl number on Holmboe instabilities were examined using a thermally stratified flow. The density interface was found to be stable without Holmboe instabilities. This is due to the large density diffusion and small Pr (thus small R) in the flow, which prevented the generation of Holmboe waves.

9.5 TWO-LAYER FLOWS IN NATURE

Some two-layer flows of concern to civil and environmental engineers were discussed. The importance of friction, especially the interfacial friction, was demonstrated, and the effects of a bottom sill was investigated. Some field observations of interfacial instabilities were reported. Further studies on the interfacial instabilities are needed in order to quantify the interfacial friction and interfacial mixing.

BIBLIOGRAPHY

Abraham, G. and Eysink, W.D. 1971 Magnitude of interfacial shear in exchange flow. *J. Hydraulic Research*, **9**(22), 125-151.

Abraham, G., Karelse, M. and van Os, A.G. 1979 On the magnitude of interfacial shear of subcritical stratified flows in relation with interfacial stability. *J. Hydraulic Research*, **17**, 273-287.

Anati, D.A., Assaf, G. and Thompson, R.O.R.Y. 1977 Laboratory models of sea straits. *J. Fluid Mech.*, **81**, 341-351.

Arita, M. and Jirka, G.H. 1987a Two-layer model of saline wedge I: Entrainment and interfacial friction. *J. Hydraulic Eng.*, **113**, 1229-1248.

Arita, M. and Jirka, G.H. 1987b Two-layer model of saline wedge II: Prediction of mean properties. *J. Hydraulic Eng.*, **113**, 1249-1263.

Armi, L. 1986 The hydraulics of two flowing layers with different densities. *J. Fluid Mech.*, **163**, 27-58.

Armi, L. and Farmer, D.M. 1986 Maximal two-layer exchange through a contraction with barotropic net flow. *J. Fluid Mech.*, **164**, 27-51.

Armi, L. and Farmer, D.M. 1988 The flow of Mediterranean water through the Strait of Gibraltar. *Progress in Oceanography*, **21**, 1-105.

Ascher, U., Christiansen, J., and Russell, R.D. 1981 Collocation software for boundary-value ODEs. *ACM Transactions on Mathematical Software*, **7**(2), 209-222.

Assaf, G. and Hecht A. 1974 Sea straits: a dynamically model. *Deep Sea Research*, **21**, 947-958.

Baines, P.G. 1984 A unified description of two-layer flow over topography. *J. Fluid Mech.*, **146**, 127-167.

Baines, P.G. 1988 A general method for determining upstream effects in stratified flow of finite depth over long two-dimensional obstacles. *J. Fluid Mech.*, **188**, 1-22.

Balsa, T.F. 1987 On the spatial instability of piecewise linear free shear layers. *J. Fluid Mech.*, **174**, 553-563.

Betchov, R. and Criminale, W.O. 1967 *Stability of parallel flows.* Academic Press, London.

Bo Pederson, Fl. 1986 Environmental hydraulics: stratified flows. Lecture notes on coastal and estuarine studies No. 18, Springer Verlag, 1986.

Bo Pederson, Fl. 1990 Friction in a shallow two-layer flow in a rotating ocean. *The physical Oceanography of Sea Straits*, L.J. Pratt (ed.), Kluwer Academic Publishers. 545-557.

Bormans, M. and Garrett C. 1989 The effects of non-rectangular cross section, friction, and barotropic fluctuations. *J. Physical Oceanography*, **19**(10), 1543-1557.

Browand, F.K. and Winant, C.D. 1973 Laboratory observations of shear-layer instability in a stratified fluid. *Boundary-Layer Meteorology,* **5**, 67-77.

Browand, R.K. and Wang, Y.H. 1972 An experiment on the growth of small disturbances at the interface between two streams of different densities and velocities. *Int. Sym. Stratified Flows*, Novosibirsk, USSR, ASCE Publications. N.Y., 491-498.

Cheung, E.A. and Lawrence, G.A. 1995 Two-layer exchange flow through a contraction with frictional effects. Submitted to *J. Hydraulic Eng.*

Conomos, T.J. 1979 San Francisco Bay: the urbanized estuary, Pacific Division American Association for the Advancement of Science.

Dalziel, S.B. 1988 Two-layer hydraulics: Maximal exchange flows. Ph.D. thesis, DAMTP, Univ. of Cambridge, Cambridge, England.

Dalziel, S.B. 1991 Two-layer hydraulics: a functional approach. *J. Fluid Mech.,* **223**, 135.

Delisi, D. and Corcos, G. 1973 A study of internal waves in a wind tunnel. *Boundary-Layer Meteorology*, **5**, 121-137.

Defant, A. 1961 *Physical Oceanography*, Vol. 1, Pergamon Press.

Denton, R.A. 1987 Locating and identifying hydraulic controls for layered flow through an obstruction. *J. Hydraulic Research,* **25**(3), 281-299.

Denton, R.A. 1990 Classification of unidirectional three-layer flow over a hump. *J. Hydraulic Research*, **28**, 215-233.

Dermissis, V. and Partheniades, E. 1984 Interfacial resistance in stratified flow. *J. Waterworks, Port, Coastal and Ocean Eng.,* **110**(2), 231-250.

Dermissis, V. and Partheniades, E. 1985 Dominant shear stress in arrested saline wedges. *J. Waterworks, Port, Coastal and Ocean Eng.* **111**(4), 733-752.

Drazin, P.G. and Reid, W.H. 1981 *Hydrodynamic Stability*. Cambridge University Press.

Dressler, R.F. 1978 New nonlinear shallow-flow equations with curvature. *J. Hydraulic Research*, **16**, 205-222.

Eides, G. 1986 Interfacial mixing in stationary, pressure-driven flow. ASCE, 322-334.

Farmer, D.M. and Armi, L. 1986 Maximal two-layer exchange over a sill and through the combination of a sill and contraction with barotropic flow. *J. Fluid Mech.,* **164**, 53-76.

Farmer, D.M. and Armi, L. 1989 The flow of Atlantic water through the Strait of Gibraltar. *Progress in Oceanography*, **21**, 1-105.

Farmer, D.M. and Freeland, H.J. 1983 The physical oceanography of fjords. *Progress in Oceanography*, **12**, 147-220.

Farmer, D.M. and Smith, J.D. 1980 Tidal interaction of stratified flow with a sill in Knight Inlet. *Deep-Sea Research*, **17**, 239-254.

Farmer, D.M. and Denton, R.A. 1985 Hydraulic control of flow over the sill in Observatory Inlet. *J. of Geophysical Research*, **90**, No. C5, 9051-9068.

Forbes, L.K. 1988 Critical free-surface flow over a semi-circular obstruction. *J. Eng. Math.*, **22**, 3-13.

Forbes, L.K. 1989 Two-layer critical flow over a semi-circular obstruction. *J. Eng. Math.*, **23**, 325-342.

Gage, K.S. 1972 Viscous stability theory for thermally stratified flow: discontinuous jets and shear layers. *Phys. Fluids*, **15**(4), 526-538.

Gage, K.S. 1973 Linear viscous stability theory of stable stratified shear flow: a review. *Boundary-Layer Meteorology*, **5**, 3-17.

Garrett, C., Bormans, M., and Thompson, K. 1990 Is the exchange through the Strait of Gibraltar maximal or submaximal? *The Physical Oceanography of Sea Straits*, L.J. Pratt (ed.), NATO/ASI, Kluwer, Dordrecht, 271-294.

Georgiev, B.V. 1990 On the interface phenomena in two-layer stratified flow. *Proc. of the Intl. Conf. on Physical modeling of Transport and Dispersion*, IAHR/ASCE, E.E. Adams & G.E. Hecker (ed.), MIT, August, 4B, 7-12.

Geyer, W.R. 1985 The Time-dependent Dynamics of a Salt Wedge. Special report No. 101, School of Oceanography, University of Washington.

Geyer, W.R. 1990 Time-dependent, two-layer flow over a sill. *The physical Oceanography of Sea Straits*, L.J. Pratt (ed.), Kluwer Academic Publishers.421-432.

Goldstein, S. 1931 On the stability of superposed streams of fluids of different densities. *Proc. of the Royal Society of London*, A **132**, 524-548.

Grant, W.D., Williams, A.J. and Glenn, S.M. 1984. Bottom stress estimates and their prediction on the northern California continental shelf during CODE-1: The importance of wave-current interaction. *J. of Physical Oceanography*, **14**, 489-648.

Grubert, J.P. 1980 Experiments on arrested saline wedge. *J. Hydraulic Division*, ASCE, **106**, HY6, 945-960.

Grubert, J.P. 1989 Interfacial mixing in stratified channel flows. *J. Hydraulic Eng.*, **115**(7), 887-905.

Grubert, J.P. 1989 Interfacial stability in stratified channel flows. *J. Hydraulic Eng.*, **115**(9), 1185-1203.

Grubert, J.P. 1990 Interfacial mixing in estuaries and fjords. *J. Hydraulic Eng.*, **116**(2), 176-195.

Guez, L.G. and Lawrence, G.A. 1995 Hydrogen bubble tracking and the determination of velocity and vorticity fields in a stratified mixing layer. Submitted to *Experiments in Fluids*.

Haigh, S.P. 1995 Non-symmetric Holmboe waves. Ph.D. thesis, Dept. of Mathematics, Univ. of British Columbia.

Hamblin, P.F. and Lawrence, G.A. 1990 Exchange flows between Hamilton Harbour and Lake Ontario. *Proc. of 1990 Annual Conf. of Canadian Society for Civil Eng.*, **V**: 140-148.

Hazel, P. 1972 Numerical studies of the stability of inviscid stratified shear flows. *J. Fluid Mech.*, **51**, 39-61.

Head, M. 1983 Ph.D. thesis, University of Southern California.

Helfrich, K.R. 1994 Time-dependent two-layer hydrauilc exchange flows, *J. of Physical Oceanography*, **24**, in press.

Helmholtz, H. von 1871 On discontinuous movements of fluids, *The London, Edinburge, and Dublin Philosophical Magazine and Journal of Science*, **36**, 337-346.

Henderson, F.M. 1966 *Open Channel Flow*, MacMillan.

Hodgins, D.O. 1974 Salinity Intrusion in the Fraser River, British Columbia. Ph.D. thesis, University of British Columbia.

Hodgins, D.O. and Mak, R.Y. 1995 Dispersion Analysis of Annacis Island Sewage Treatment Plant Effluent in the Fraser River. Prepared for B.C. Ministry of Environment, Lands and Parks by Seaconsult Marine Research Ltd., Vancouver, B.C.

Holmboe, J. 1962 On the behavior of symmetric waves in stratified shear layers. *Geofysiske Publikasjoner*, **24**, 67-113.

Jameel, M.I. 1991 Modelling of two-layer flow over an obstacle. Ph.D. thesis, Dept. of Mech. Eng., Univ. of Calgary.

Kelvin, L. 1871 Hydrokinetic solutions and observations. *The London, Edinburge, and Dublin Philosophical Magazine and Journal of Science,* **42**, 362-377.

Keulegan, G.H. 1949 Interfacial instability and mixing in stratified flows. Res. Paper RP2040, U.S. Nat. Bureau of Standards, **43**, 487-500.

Knauss, J.A. 1978 *Introduction to Physical Oceanography*, Prentice-Hall.

Koop, C.G. and Browand, F.K. 1979 Instability and turbulence in a stratified fluid with shear. *J. Fluid Mech.*, **93**, 135-159.

Koppel, D. 1964 On the stability of flow of a thermally stratified fluid under the action of gravity. *J. Math. Phys.*, **5**, 963-982.

Lai, K.K. and Wood, I.R. 1975 A two-layer flow through a contraction. *J. Hydraulic Research,* IAHR, 13, 19-34.

Lawrence, G.A. 1985 The hydraulics and mixing of two-layer flow over an obstacle. Ph.D. thesis, Dept. of Civil Eng., Univ. of California, Berkeley.

Lawrence, G.A. 1990 On the hydraulics of Boussinesq and non-Boussinesq two-layer flows. *J. Fluid Mech.*, **215**, 457-480.

Lawrence, G.A. 1993 The hydraulics of steady two-layer flow over a fixed obstacle. *J. Fluid Mech.*, **254**, 605-633.

Lawrence, G.A., Browand, F.K. and Redekopp, L.G. 1991 The stability of a sheared density interface. *Physics of Fluids A*, **3**(10), 2360-2370.

Lawrence, G.A., Haigh, S.P. and Zhu, Z. 1995 In search of Holmboe instabilities, *Symposium on Physical Limnology*, IUTAM, Broome, Western Australia, 445-452.

Lock, R.C. 1951 The velocity distribution in the laminar boundary layer between parallel streams. *Quart. J. Appl. Math.*, **4**, 42-63.

Long, R.R. 1954 Some aspects of the flow of stratified fluids II: Experiments with two-fluids. *Tellus*, **6**, 97-115.

Long, R.R. 1970 Blocking effects in flow over obstacles. *Tellus*, **22**, 471-480.

Long, R.R. 1974 Some experimental observations of upstream disturbances in a two-fluid system. *Tellus*, **26**, 313-317.

Maslowe, S.A. 1973 Finite-amplitude Kelvin-Helmholtz billows. *Boundary-Layer Meteorology*, **5**, 43-52.

Maslowe, S.A. and Thompson, J.M. 1971 Stability of a stratified free shear layer. *Physics of Fluids,* **14**, 453-458.

Melville, W.K. and Helfrich, K.R. 1987 Transcritical two-layer flow over topography. *J. Fluid Mech.,* **178**, 31-52.

Merzkirch, W. 1987 *Flow Visualization*, Academic Press.

Mehta, A.J. and Srinivas, R. 1993 Observations on the entrainment of fluid mud by shear flow. *Nearshore and Estuarine Cohesive Sediment Transport*, A.J. Mehta, ed. American Geophysical Union.

Miles, J.W. 1961 On the stability of heterogeneous flows. *J. Fluid Mech.,* **10**, 496-508.

Miller, J.R. and Gage, K.S. 1972 Prandtl number dependence of the stability of a stratified free shear layer. *Physics of Fluids,* **15**, 723-725.

Moore, M.J. and Long, R.R. 1971 An experimental investigation of turbulent stratified shearing flow. *J. Fluid Mech.,* **49**(4), 635-655.

Naghdi, P.M. and Vongsarnpigoon, L. 1986 The downstream flow beyond an obstacle. *J. Fluid Mech.,* **162**, 223-236.

Nishida, S. and Yoshida, S. 1987 Stability and eigen functions of disturbances in stratified two-layer shear flows. *Proc. of Third Intl. Symposium on Stratified Flows*, Pasadena, California, 3-5 February 1987, 28-34.

Nishida, S. and Yoshida, S. 1990 Influence of the density and velocity profiles on calculated instability characteristics in an inviscid two-layer shear flow. *J. Hydroscience and Hydraulic Eng.,* **7**, 61-58.

Pouliquen, O., Chomaz, J.M., and Huerre, P 1994 Propagating Holmboe waves at the interface between two immiscible fluid. *J. Fluid Mech.,* **266**, 277-302.

Oguz, T., Ozsoy, E., Latif, M.A., Sur, H.I. and Unluata, U. 1990 Modeling of hydraulically controlled exchange flow in the Bosphorus Strait, *J. of Physical Oceanography*, **20**, 945-965.

Oguz, T. and Sur, H.I. 1989 A two-layer model of water exchange through the Dardanelles Strait, *Oceanol. Acta*, **12**, 23-31.

Ottesen-Hansen, N.E., Moller, J.S. 1990 Zero blocking solution for the Great Belt Link, *The physical Oceanography of Sea Straits*, L.J. Pratt (ed.), Kluwer Academic Publishers. 153-170.

Pratt, L.J. 1984 Nonlinear flow over several obstacles. *J. Atmospheric Sciences*, **4**, 1212-1225.

Pratt, L.J. 1986 Hydraulic control of sill flow with bottom friction. *J. Physical Oceanography*, **16**,1970-1980.

Rignot, E.J.M. and Spedding, G.R. 1988 Performance analysis of automated image processing and grid interpolation techniques for fluid flows. USCAE 143, Dept. of Aerospace Eng., Univ. of Southern California.

Rottman, J.W. and Smith, R.B. 1989 Tow-tank simulations of the severe downslope wind, *Proc. of Third Intl. Symposium on Stratified Flows*, Pasadena, California, 3-5 February 1987, 717-725.

Sargent, F.E. and Jirka, G.H. 1987 Experiments on saline wedge. *J. Hydraulic Eng.,* **113**(10), 1307-1324.

Schijf, J.B. and Schonfeld, J.C. 1953 The practical considerations on the motion of salt and fresh water. *Proc. of the Minn. Intl Hyd. Conv. Joint meeting of the IAHR and Hyd. Div.*, ASCE, 321-333.

Schlichting, H. 1986 *Boundary layer theory.* 6th ed., McGraw Hill, New York.

Scott, R.S. and Corcos, G.M. 1972 An experiment on the stability of small disturbances in a stratified free shear layer. *J. Fluid Mech.,* **52**, 499-528.

Seim, H.E. and Gregg, M.C. 1994 Detailed observations of a naturally occurring shear instability. *J. Geophysical Research*, **99**, No. C5, 10049-10073.

Shen, S.P., Shen, M.C., and Sun, S.M. 1989 A model equation for steady surface waves over a bump. *J. Eng. Math.,* **23**, 315-323.

Shen, S.S. 1992 Forced solitary waves and hydraulic falls in two-layer flows. *J. Fluid Mech.,* **234**, 583-612.

Sherenkov, I.A., Netjukhailo, A.P., and Teleshkin, E.D. 1971 Research in transfer process in two-dimensional stratified flow. Proc., 14 th Congress of Int. Assoc. of Hydr. Res., 1, Paris, France, A26/1-9.

Sherman, F.S., Imberger, J. and Corcos, G.M. 1978 Turbulence and mixing in stably stratified fluids. *Ann. Rev. Fluid Mech.,* **10**, 267-288.

Sivakumaran, N.S., Hosking, R.J., and Tingsanchali, T. 1981 Steady shallow flow over a spillway. *J. Fluid Mech.,* **111**, 411-420.

Sivakumaran, N.S., Tingsanchali, T. and Hosking, R.J. 1983 Steady shallow flow over curved beds. *J. Fluid Mech.,* **128**, 469-487.

Smyth, W.D., Klaassen, G.P. and Peltier, W.R. 1988 Finite amplitude Holmboe waves. *Geophys. Astrophys. Fluid Dynamics,* **43**, 181-222.

Smyth, W.D., Klaassen, G.P. and Peltier, W.R. 1991 Instability and transition in finite-amplitude Kelvin-Helmholtz and Holmboe waves. *J. Fluid Mech.,* **228**, 387-415.

Smyth, W.D., Peltier, W.R. 1989 The transition between Kelvin-Helmholtz and Holmboe instability; An investigation of the over reflection hypothesis. *J. Atmospheric Sciences,* **46**(24), 3698-3720.

Smyth, W.D., Peltier, W.R. 1990 Three-dimensional primary instabilities of a stratified, dissipative, parallel flow. *Geophys. Astrophys. Fluid Dynamics,* **52**(4), 249-261.

Squire, H.B. 1933 On the stability for three-dimensional disturbances of viscous fluid flow between parallel walls. *Proc. of the Royal Society A*, **142**, 621-628.

Standard Methods 1989 17th Edition, APHA, AWWA, WPCF, Washington, DC.

Stevens, C.L. and Coates, M.J. 1994 Application of a maximised cross correlation technique for resolving velocity fields in laboratory experiments. *J. Hydraulic Research,* **32**(2), 195-212.

Stommel, H. and Farmer, H.G. 1953 Control of salinity in and estuary by a transition. *J. Marine Research,* **12**,13-20.

Taylor, G.I. 1931 Effect of variation in density on the stability of superposed streams of fluids. *Proc. of the Royal Society of London, A* **132**, 499-523.

Thorpe, S.A. 1968 A method of producing a shear flow in a stratified flow. *J. Fluid Mech.,* **32**, 693-704.

Thorpe, S.A. 1971 Experiments on the stability of stratified shear flows; miscible fluids. *J. Fluid Mech.,* **46**, 299-320.

Thorpe, S.A. 1973a Experiments on instability and turbulence in a stratified shear flow. *J. Fluid Mech.,* **61**, 731-751.

Thorpe, S.A. 1973b Turbulence in stably stratified fluids: a review of laboratory experiments *Boundary-Layer Meteorology,* **5**, 95-119.

Thorpe, S.A. 1984 A laboratory study of stratified accelerating shear flow over a rough boundary. *J. Fluid Mech.,* **138**, 185-196.

Thorpe, S.A. 1987 Transitional phenomena and the development of turbulence in stratified fluids: A Review. *J. Geophys. Research,* **92**, 5231-5248.

Tritton, D.J. and Davies, P.A. 1985 Instabilities in geophysical fluid dynamics. *Hydrodynamic Instabilities and the Transition to Turbulence*, Springer-Verlag.

Turner, J.S. 1973 *Buoyancy effects in fluids.* Cambridge University Press.

US Army Corps of Engineers 1980 Hydraulic model study for the John F. Baldwin ship channel - Incremental Improvements with/without fluid submerged barriers. Department of the Army, San Francisco District, Corps of Engineers, San Francisco, CA, July 1980.

Vanden-Broeck, Jean-Marc 1987 Free-surface flow over an obstruction in a channel. *Phys. Fluids,* **30**(8), 2315.

White, F.M. 1991 Viscous fluid flow. McGraw-Hill, Inc.

Whitham, G.B. 1974 *Linear and nonlinear waves.* Wiley-interscience.

Wilkinson, D.L. and Wood, I.R. 1971 A rapidly varied flow phenomenon in a two-layer flow. *J. Fluid Mech.,* **47**(2), 241-256.

Wilkinson, D.R. and Wood, I.R. 1983 The formation of an intermediate layer by horizontal convection in a two-layer shear flow. *J. Fluid Mech.,* **136**, 167-187.

Wood, I.R. 1968 Selective withdrawal from a stably stratified fluid. *J. Fluid Mech.,* **32**(2), 209-223.

Wood, I.R. 1970 A lock exchange flow. *J. Fluid Mech.*, **42**, 671-687.

Wood, I.R. and Lai, K.K. 1972 Flow of layered fluid over broad crested weir. *J. Hydr. Div. ASCE* **98**, 87-104.

Yin, D.S. 1969 A class of solutions for steady stratified flows. *J. Fluid Mech.,* **140**, 329-342.

Yonemitsu, N. 1991 The stability and interfacial phenomena of a salt wedge flow. Ph.D. thesis, Dept. of Civil Eng., Univ. of Alberta.

Yonemitsu, N., Swaters, G.E., Rajaratnam, N., and Lawrence, G.A. 1996 Shear instabilities in arrested salt-wedge flows. *Dynamics of Atmospheres and Oceans,* **24**, 173-182.

Yoshida S., Ohtani, M., Nishida, S., and Linden, P.F. 1995 Mixing at the density interface of the shear layer in a highly stratified two-layer flow in the vicinity of a river mouth. *Symposium on Physical Limnology*, IUTAM, Broome, Western Australia.

Zhu, Z. and Lawrence, G.A. 1996a Exchange flow through a channel with an underwater sill. *Dynamics of Atmospheres and Oceans*, **24**, 153-161.

Zhu, Z. and Lawrence, G.A. 1996b Curvature effects in exchange flows, in preparation.

Appendix A
NUMERICAL TECHNIQUES

Three types of problems are discussed and solved in this thesis: (1) uni-directional flows with curvature effects but not friction; (2) exchange flows with frictional effects but not curvature; (3) exchange flow with both friction and curvature. Numerical methods for solving these problems are detailed below. Table A.1 shows a summary of the main features of these problems.

Table A.1 Numerical Methods for Solving Three Types of Problems

	Unknown	Equation	Control conditions	Method	Notes
<u>curvature / no friction</u> *e.g.* one-layer flows or uni-directional two-layer flows	E, y	Eq. (5.21) or (5.31) (2nd order ODE)	(1) sill control $S_0+S_c = 0$	BVP with trial and error	Same for one- or uni-directional two-layer flows.
<u>no curvature / friction</u> *e.g.* exchange flows	E, q, y	Eq. (6.3) (1st order ODE)	(1) Sill control: $S_0+S_f = 0$ (2) Exit control: at the exit	SHOOTING with trial and error	
<u>curvature / friction</u> *e.g.* exchange flows	E, q, y	Eq. (6.3) & (6.5) (3rd order ODE)	(1) Sill control: $S_0+S_f+S_c = 0$ (2) Exit control: at the exit	BVP with trial and error	

A.1 UNI-DIRECTIONAL FLOWS WITH CURVATURE EFFECTS

For uni-directional two-layer flows, the procedure is similar to that for single-layer flows and will not be discussed separately. Here the single-layer flows with curvature effects are considered. For the single-layer flow over a sill, we will only consider crest-controlled flow, *i.e.*, the flow is critical at the sill crest point. We write Eq. (4.21) in the following form:

$$y_{xx} - \tfrac{1}{2}y^{-1}y_x^2 + \tfrac{3}{2}(h_x^2 + \sigma^{-1})y^{-1} + 3\sigma^{-1}(-E + h + y)q^{-2}y + \tfrac{3}{2}h_{xx} = 0, \tag{A.1}$$

where y is the interface position, h is the shape of the sill, q and E are the flow rate and the total energy, respectively; σ measures the relative depth of the flow, with $\sigma = (H/L)^2 << 1$. q and h are known, whereas E needs to be determined from the sill control condition.

Equation (A.1) is a non-linear second order ordinary differential equation (ODE) with a small parameter σ. There is difficulty in solving the equation using shooting method, as has been discussed in Section 5.2. The equation can be solved as a boundary value problem (BVP) using a general-purpose code, COLNEW, developed by Ascher *et al.* (1981). The COLNEW is capable of solving mixed-order systems of boundary-value problems in ordinary differential equations. In order to apply the code, two boundary conditions, y_A and y_B, as well as E, need to be given, where A and B are the far upstream and downstream of the sill, respectively. The flow is subcritical at A and supercritical at B. The flow streamline curvature is negligibly small at both A and B since they are far away from the sill. Thus $E = (E_H)_B = (E_H)_A$. The equation can be solved using the sill control condition. The detailed calculation procedure is as follows: (1) guess an initial y_B for the given flow rate q and the sill shape; (2) compute the energy $E = (E_H)_B$ assuming negligible streamline curvature at far upstream, and calculate y_A from $(E)_A = E$; (3) use BVP solver to calculate for the surface position, check the results and adjust the guessed y_B until the solution is steady and without short waves.

The reason for the wavy solution can be explained as follows: The flow is governed by the conservation of the total energy E. When the upstream and downstream layer thickness are given, the hydrostatic part of the energy at both ends is given, but not the total energy, which is determined by the control condition. The code then tries to find the specific surface profile to satisfy the total energy requirement. This will result a prediction of wavy surface when the initial guess is off.

This wave phenomena can also be explained from another point of view: For steady flows, the surface profile should be smooth and without short waves. The upstream and downstream layer thickness are also uniquely determined. When the layer thickness at either end is forced to be some other value, the flow has to adjust to the new condition by forming and propagating waves. Knowing the steady state of the flow is free of short waves, the solution of the equation can then be found by adjusting the initial guess y_B.

A.2 EXCHANGE FLOWS WITH FRICTION EFFECTS

For steady viscous hydrostatic exchange flows without barotropic forces, Eq. (A.2) together with two control conditions can be used to solve for three unknowns: the flow rate q, the interface positions at the sill crest y_s and at the exit y_e. For our exchange flows, the controls are the sill and exit control. The exit control is forced at the channel right hand exit given the sudden increase of the channel width, whereas the sill control is shifted towards left to the point where $S_f = S_0$ due to friction. The exact location of the sill control is unknown and depending on the flow conditions. The composite Froude number at the sill crest, G_s^2, is now less than one. By guessing a set of G_s^2 and y_s at the sill crest, q can be calculated, and the calculation can be started towards upstream to the sill control and downstream to the exit control using (A.2). Adjust both G_s^2 and y_s until both the sill and exit controls are satisfied.

$$y_x = \frac{S_f - S_0}{1 - G^2}. \tag{A.2}$$

The above method requires the initial guessing of two parameters, G_s^2 and y_s. This is not as formidable as it seems since the sill control is sensitive to the value of G_s^2 and thus G_s^2 could be easily determined. This computing method starting from the sill crest where $G_s^2 \neq 1$ also avoids the difficulty of computing the flow with a singular point within the domain.

A.3 EXCHANGE FLOWS WITH FRICTION AND CURVATURE EFFECTS

The exchange flows with the effects of friction and curvature considered are governed by Eq. (6.3) and Eq. (6.5). Here these two equations are renamed to Eq. (A.3) and Eq. (A.4).

$$\frac{dE}{dx} = S_f, \tag{A.3}$$

$$\sigma y_{xx} = \frac{3y_1 y_2}{y_1 + y_2}\left\{\frac{E-y}{q^2} - \frac{1}{2}\left(\frac{1}{y_2^2} - \frac{1}{y_1^2}\right) - \sigma\left(\frac{h_{xx}}{6y_2} + \frac{h_x^2}{2y_2^2} - \frac{y_{2x}^2}{6y_2^2} + \frac{y_x^2}{6y_1^2}\right)\right\}, \tag{A.4}$$

where $y_1 = 1 - y$, $y_2 = y - h$, and $\sigma = (H/L)^2 << 1$.

Equation (A.4) is a second order ODE with a small parameter σ. The equation is similar to Eq. (A.1), except that E is no longer a constant here. Similarly, the shooting method does not work for this problem. Also the iteration method fails for the exchange flow problems, (see Section 6.3 for more details). We solve the equations as a boundary value problem (BVP) using the COLNEW code developed by Ascher et al. (1981), same as that discussed in Section A.1. Equations (A.3) and (A.4) combined with two control conditions are used to solve the flow.

The computation cannot be started from the sill control, since E is unknown due to significant curvature effects there, also the exact location of the control is unknown. Therefore, the sill control is avoid and the point to the left of the sill (A) is used as one of the computation boundaries, see Figure A.1. Another boundary is chosen as the channel right hand exit (B). However, E is difficult to determine at Point B since the streamline curvature is unknown. The curvature effect is negligibly small at Point A. But since the flow is strongly supercritical, a small change in y_A will result in significant change in $(E)_A$, and the computation is very unstable.

Thus Point A is also avoided. As a result, Point C in the middle of the channel is chosen, where the curvature effects is very small, thus $(E)_C \approx (E_H)_C$. Therefore, we separate the whole computation domain into two sections, Section A-C, (the sill region) and Section C-B (the channel region). These two regions are connected at point C, and can be computed separately.

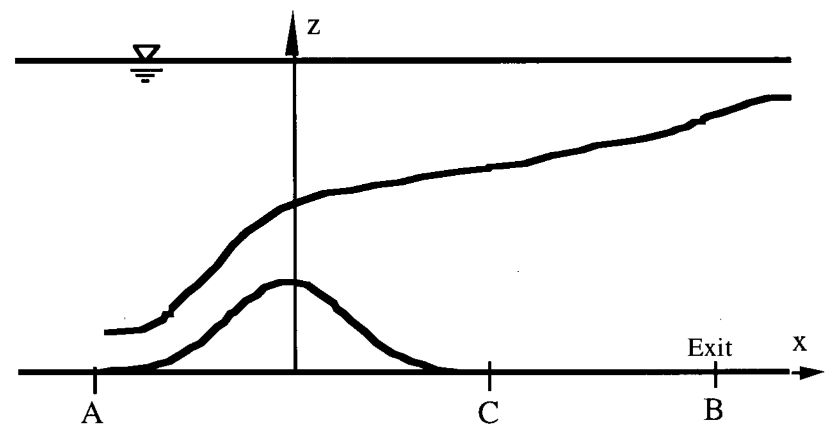

Figure A.1 Computing domain of exchange flows.

For the sill region (Section A-C), in order to start the BVP code, we need to supply the flow rate q, the guessed values of y_A and y_C, as well as $(E)_C$. $(E)_C$ can be obtained from y_C since $(E)_C \approx (E_H)_C$. Using $(E)_C$ as one of the initial conditions has significant advantage since it is less sensitive to the initial guess y_C given the flow is subcritical there. Interestingly, when y_C is used as the main boundary condition, the solution is not sensitive to y_A. Therefore, for any given q, y_C can be uniquely determined by satisfying the sill control condition, and the relationship between q and y_C can be obtained. The real solution for the interface profiles should not contain short waves or interfacial fluctuations, as discussed in Section A.1.

We now calculate the flow in the channel region (Section C-B). For a given q, y_C is obtained from the sill region computation, and $(E)_C = (E_H)_C$. Adjust y_B until the equations can be solved for Section C-B. If the solution does not satisfy the control condition, try another q and repeat the process. When the flow rate q and y_B are found, the flow is then solved for the whole channel.

The above procedure can be summarized as follows: (1) Specify the friction factors, f_I and f_w, (2) obtain the frictional hydrostatic prediction, which provides an initial guess for the computation with the curvature effects, (3) divide the computation domain into two regions, and compute the sill region and obtain the relationship between q and y_C, (4) compute the channel region to determine both q and y_B.

The above approach of separating the computation domains into two regions reduces the number of unknowns for each sub-domain, and thus greatly simplify the computation, which, at the beginning, has four unknowns, q, y_A and y_B, $(E)_A$ or $(E)_B$. The choosing of the middle point to start the computation also avoid the sensitivity of the flow in the supercritical region. However, for some cases, the solution is hard to obtained due to the characteristics of the Eq. (A.4).

APPENDIX B

DETERMINATION OF WALL FRICTION FACTORS

Accurate determination of the friction factors for the sidewalls and bottom is important in order to quantify the frictional effects on exchange flows. For our experimental flows, the boundary layers of the sidewalls and the bottom are not fully developed. Thus, boundary layer theories are used to predict the friction factors. To simplify the study, the sidewalls and the bottom are treated as flat plates to calculate the friction factors. For the friction caused by a flat plate within an infinite uniform flow, Blasius flat plate theory can be used. The actual flows, however, are much more complicated. A typical exchange flow has the layer thickness and thus the layer averaged velocity changing over the channel. The friction of a flat plate on a flow with a velocity gradient is studied using an integral momentum methods; here Thwaites method (White 1991) is used.

B.1 THWAITES METHOD

The development of the boundary layer of a flat plate within an infinite uniform velocity field of U was first studied by Blasius. The friction factor f_w at any position x for one side of the plate is given as (see, for example, White 1991):

$$f_w = \frac{2\tau_w}{\rho U^2} = \frac{0.664}{\sqrt{\mathrm{Re}_x}}, \tag{B.1}$$

where $Re_x = Ux/\nu$ with x starting from the edge of the plate. The averaged friction factor over the length from x_0 to x be obtained

$$\bar{f}_w = \frac{1}{(x - x_0)} \int_{x_0}^{x} f_w(x) dx. \tag{B.2}$$

The above equations are applicable to laminar flows, with $Re_x \leq 5 \times 10^5$ for flat plates within parallel flows, or $Re_x \leq 54,000$ for flat plates within non-parallel flows (White 1991).

The development of the boundary layer of a flat plate in a flow field with changing free stream velocity can be described by the boundary-layer integral equation. For steady two-dimensional incompressible flow with an impermeable wall, the integral equation, known as the Karman momentum relation, can be written as (see White 1991)

$$\frac{f_w}{2} = \frac{\tau_w}{\rho U^2} = \theta_x + (2 + H^*)\frac{\theta}{U}U_x \ , \quad H^* = \frac{\delta^*}{\theta}, \tag{B.3}$$

where H^* is the shape factor, δ^* is the displacement thickness, and θ is momentum thickness. Subscript x denotes the differentiation with respect to x.

Instead of using guessed velocity profiles, Thwaites used empirical correlation among the integral parameters to solve Eq.(B.3) (White 1991). This method is later called Thwaites method, and the detailed procedure is presented below. The accuracy of Thwaites method is about ± 5 % for positive or slightly negative velocity gradients.

Introducing a parameter λ, where $\lambda = \theta^2 U_x / \nu$, θ can be predicted accurately (± 3 percent) for all types of laminar boundary layers, by the simple quadrature

$$\theta^2 \approx \frac{0.45\nu}{U^6}\int_0^x U^5 dx, \tag{B.4}$$

where $x = 0$ is the point where the boundary starts to develop.

The friction factor f_w and the displacement thickness δ^* can then be determined:

$$f_w = \frac{2\nu}{U\theta}S(\lambda) \ , \tag{B.5}$$

$$\delta^* = \theta H^*(\lambda), \tag{B.6}$$

In Eqs. (B.5) and (B.6), the shear function $S(\lambda)$ and the shape-factor function $H^*(\lambda)$ are determined from the simple correlation suggested by Thwaites:

$$S(\lambda) \approx (\lambda + 0.09)^{0.62}, \tag{B.7}$$

$$H^*(\lambda) \approx 2.0 + 4.14z - 83.5z^2 + 854z^3 - 3337z^4 + 4576z^5, \tag{B.8}$$

where $z = 0.25 - \lambda$.

B.2 WALL FRICTION FACTORS FOR EXCHANGE FLOWS OVER A SILL

For the exchange flows between the sill and the channel right hand exit, the flow accelerates towards downstream for both the upper and lower layer. Thus Thwaites method has to be used. To apply Thwaites method, some simplifications are made: (1) The bottom of the channel is treated as a flat plate since the sill is smooth. (2) The boundary layers develop independently for the sidewalls and the bottom, thus can be treated separately as flat plates without significant interaction. (3) The interface has a similar displacement thickness as that of the sidewalls. (4) The free stream velocity (the velocity outside the boundary layers) is only a function of x, *i.e.*, no vertical or lateral variations. (5) The flow is uniform when it enters the channel. (6) The friction for the free surface is negligible. In the exchange flows, the boundary layers for the front panel and the bottom develop further upstream than the edge of the channel, while that of the rear panel develops from the edge of the channel. Therefore, the boundary layers for the lower layer are approximated as developing from the position $x \approx 1.1$ (103+8 cm), while that of the upper layer developing from $x \approx -0.2$ (- 20 cm).

Based on the above assumptions, the friction factor for the bottom is the same as that for the two sidewalls for the lower layer. The sidewall friction factors for the upper and lower layer, however, can be different due to the different boundary layer development. The errors due to the above simplifications are not significant. The above procedures, though, mainly used for the exchange flow over a sill, is also applicable for the exchange flow through a flat channel.

With these assumptions, the friction factors can be calculated using Thwaites method. Since the friction affects the prediction of the exchange flow (both flow rate and interface positions), while the friction is also determined by the flow, iteration is needed. The iteration can be started by predicting the flow assuming no friction. Estimates of the friction factors can then be obtained using Thwaites method, and the flow can be predicted using the newly obtained friction factors. This iteration can be continued, but normally is not necessary since the friction factor converges very fast.

(a)

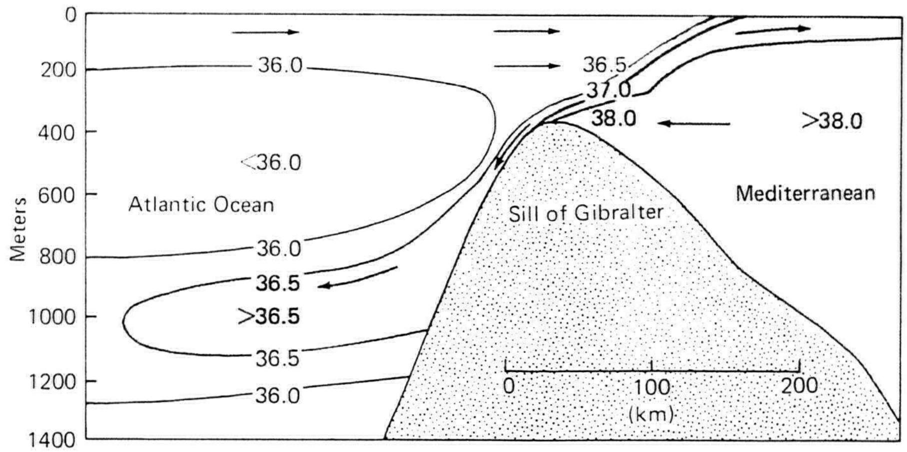

(b)

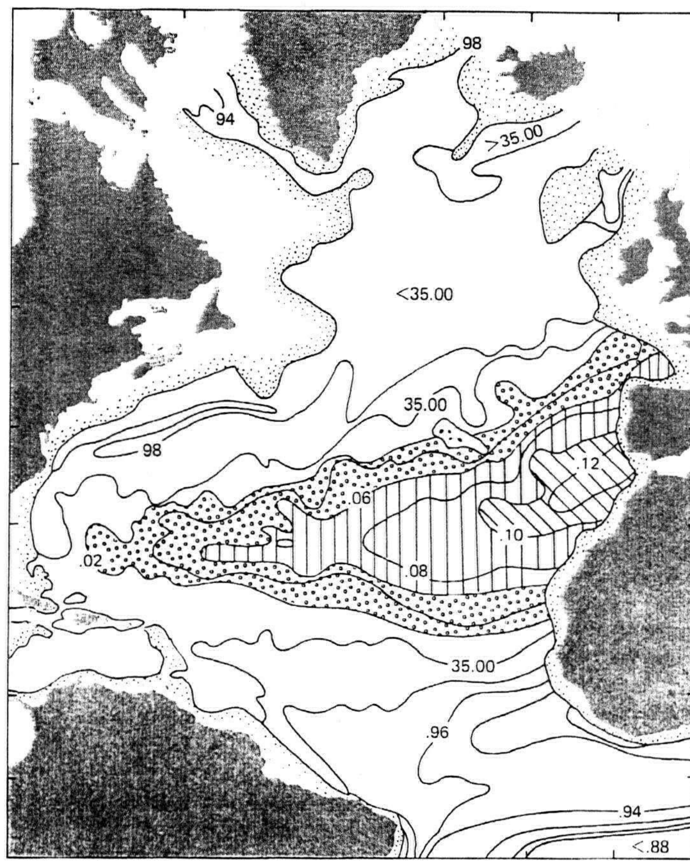

Figure 1.1 Exchange flow through the Strait of Gibraltar. Contours show the salinity of sea water. (a) Dense, highly saline water of the Mediterranean flows into the North Atlantic over the sill at the Strait of Gibraltar. (b) Spreading of the high-saline Mediterranean water can be traced across the entire Atlantic. (From Figures 9.2 and 9.3 of Knauss 1978).

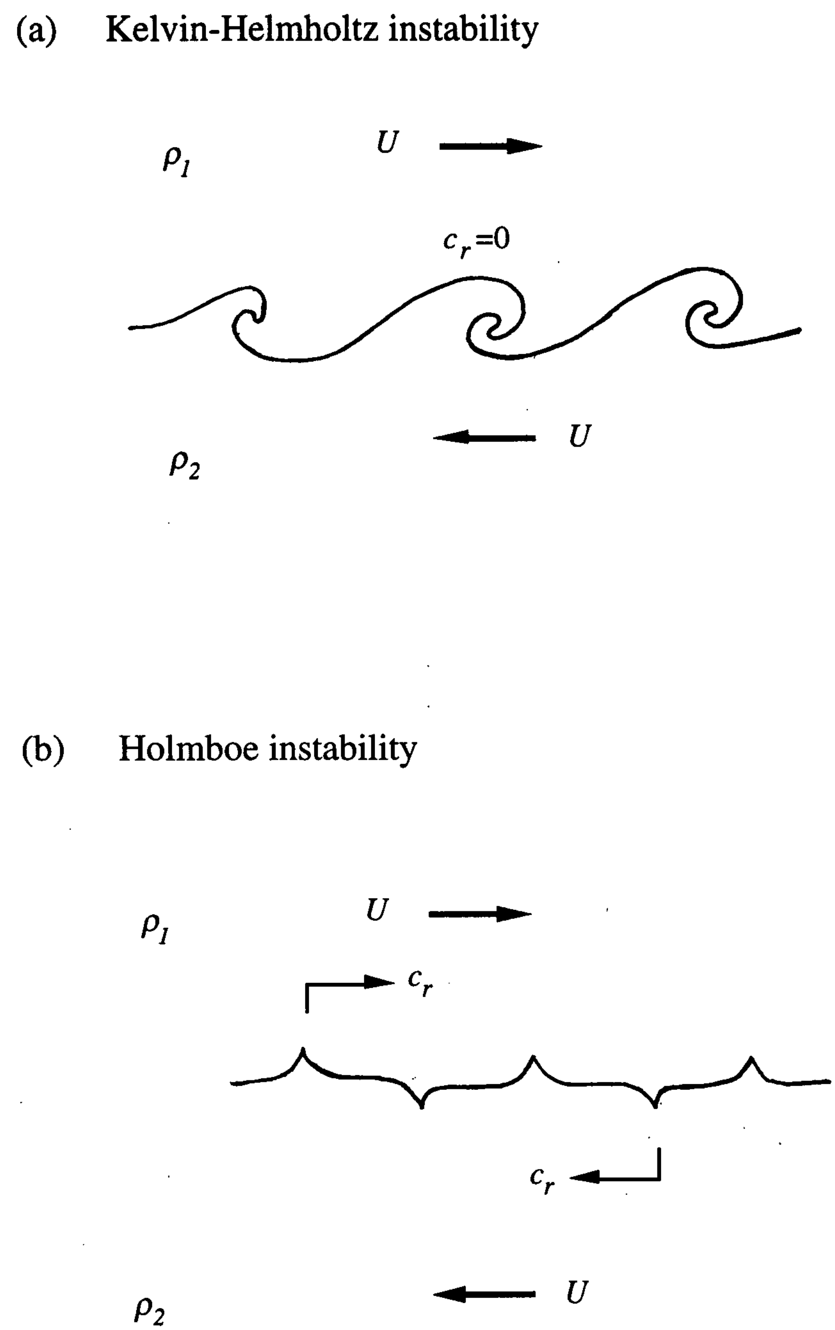

Figure 1.2 Types of interfacial instabilities in two-layer flows. (a) Kelvin-Helmholtz instabilities: waves roll over and have zero propagating speed with respect to the mean flow, (b) Holmboe instabilities: two sets of symmetric waves protruding into the upper or lower layer, propagating in opposite directions at the same speed with respect to the mean flow.

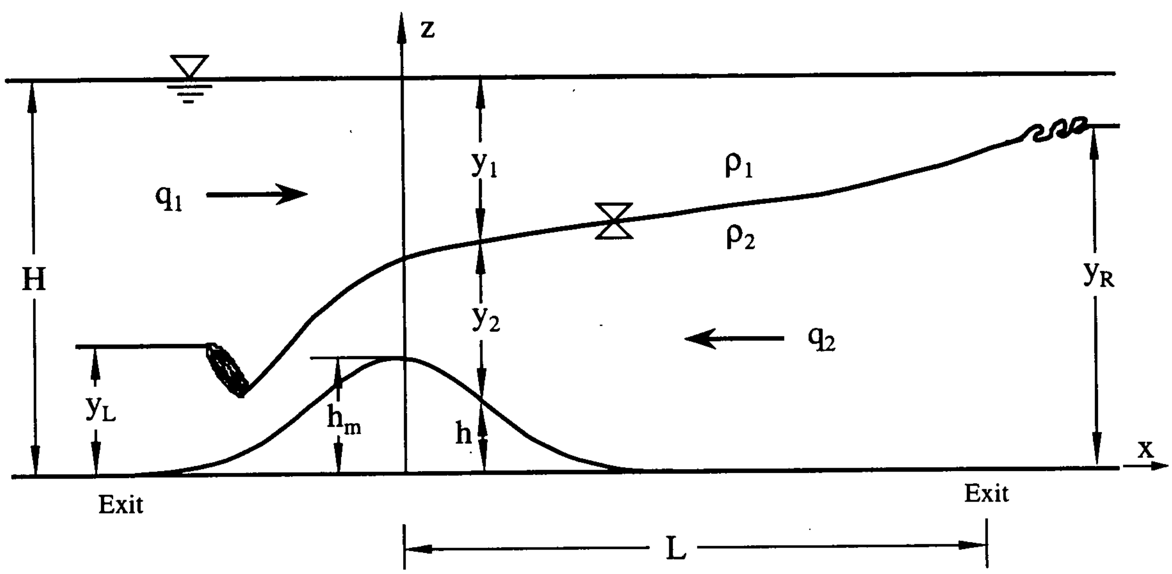

Figure 2.1 Definition diagram of a two-layer exchange flow through a channel with an underwater sill.

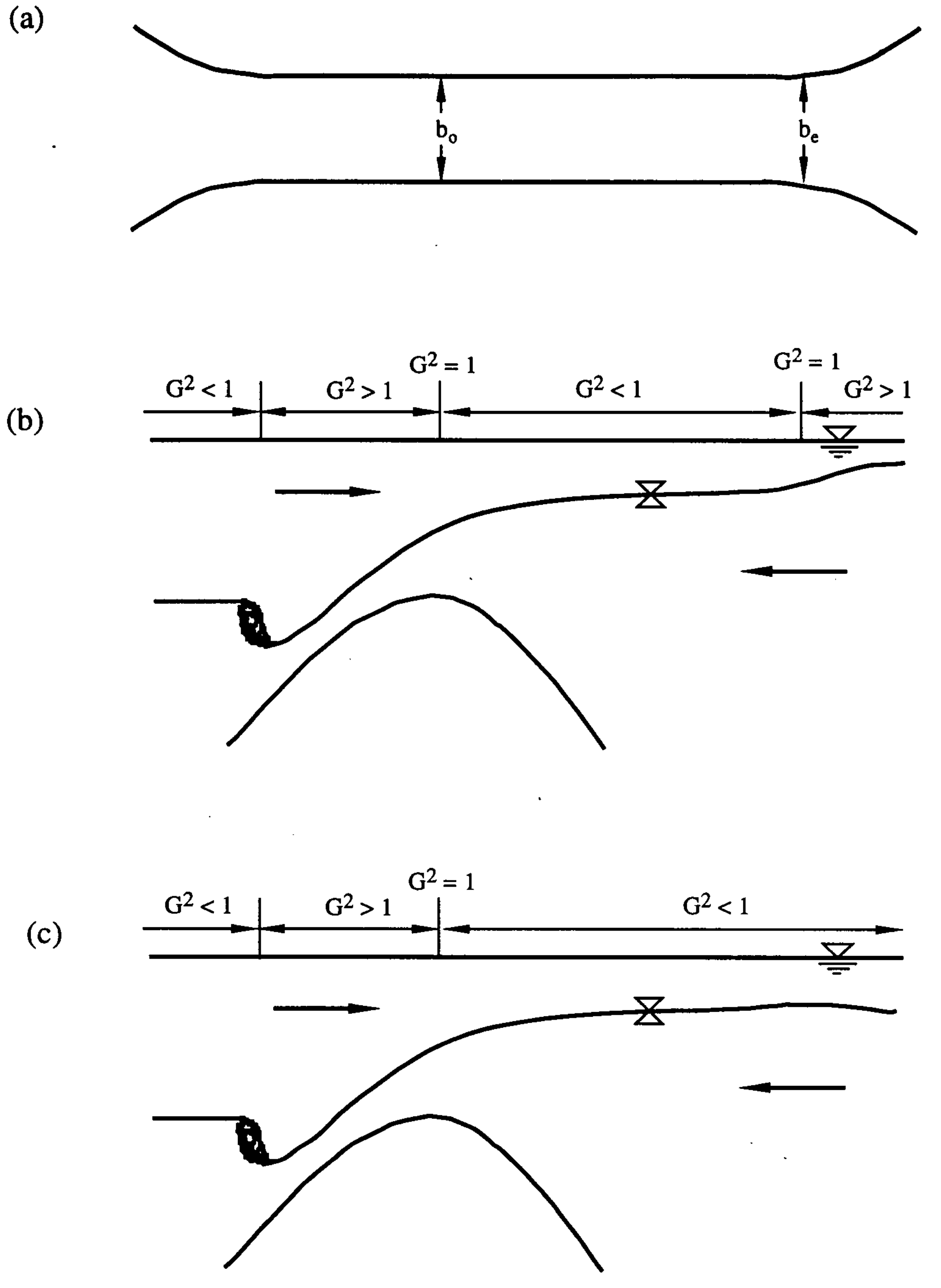

Figure 2.2 Exchange flow through a channel with a sill, (a) plan view, (b) maximal exchange, (c) submaximal exchange. Adopted from Farmer and Armi (1986).

(a)

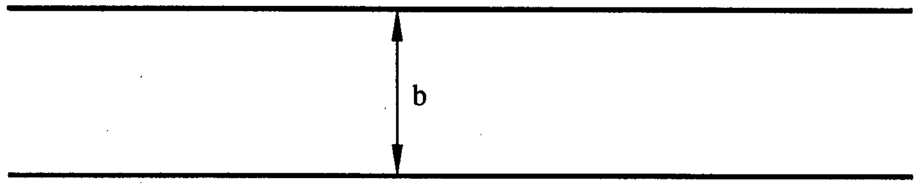

(b)

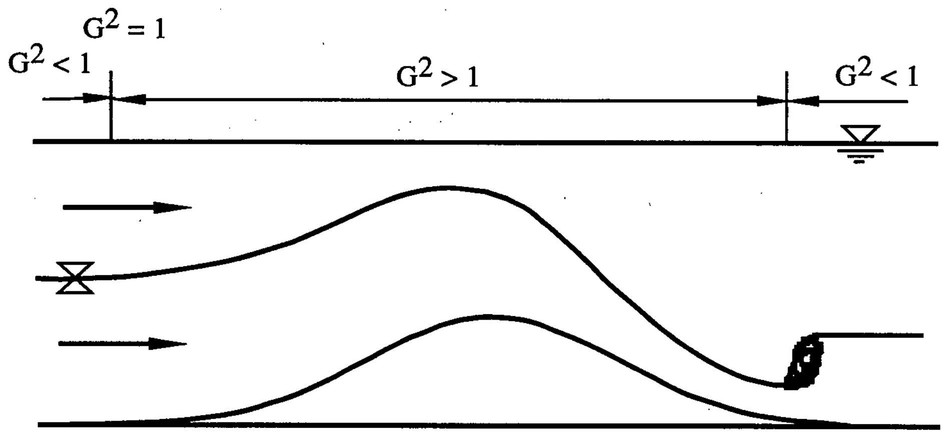

Figure 2.3 Two-layer approach-controlled flow: (a) plan view, (b) side view. The flow is subcritical upstream of the sill, critical near the foot of the sill, and supercritical over the sill. An internal hydraulic jump occurs in the downstream of the sill.

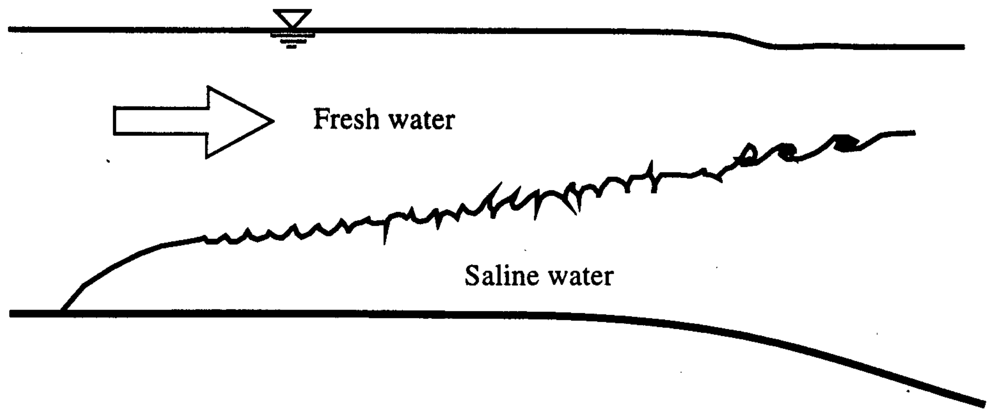

Figure 2.4 Arrested saline wedge flow with interfacial instabilities. Adopted from Yonemitsu (1996).

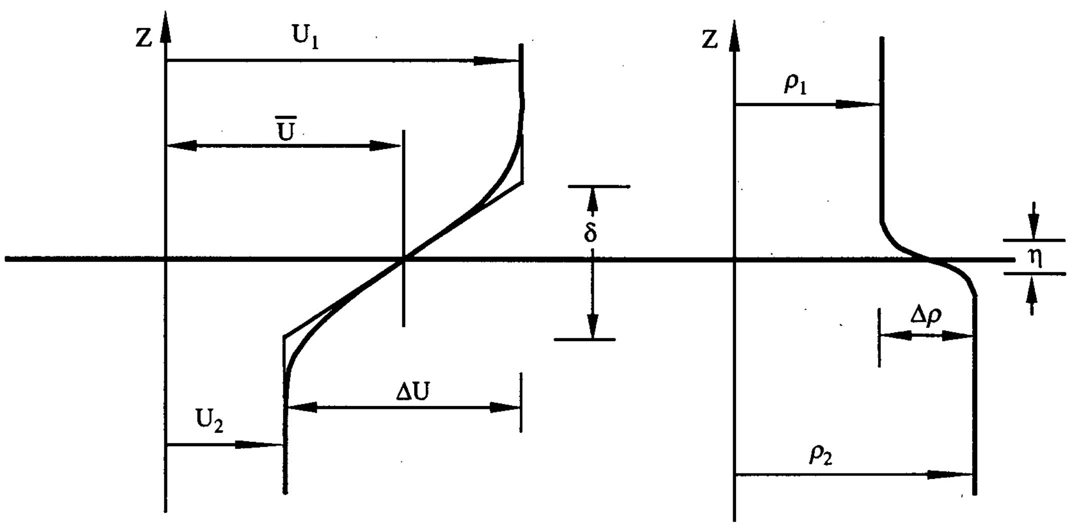

Figure 2.5 Interfacial shear and density layers in two-layer flows. δ and η are the thickness of the shear layer and density layer respectively, with $\delta = \Delta U/(du/dz)_{max}$ and $\eta = \Delta\rho/(d\rho/dz)_{max}$.

(a)

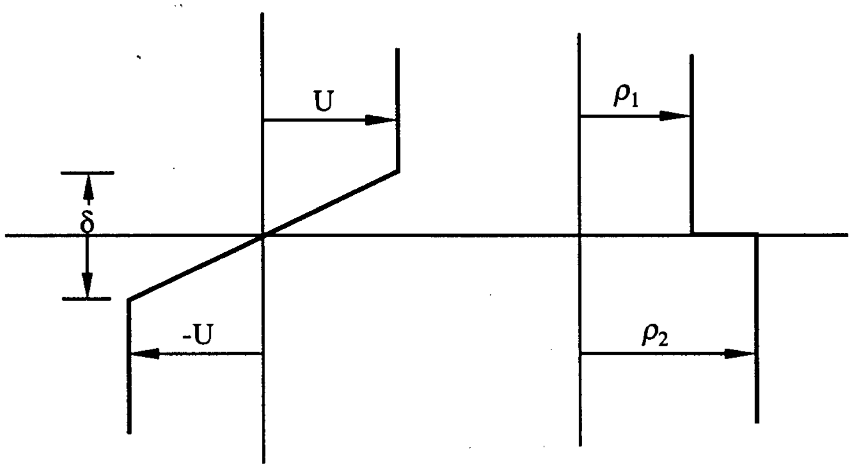

(b)

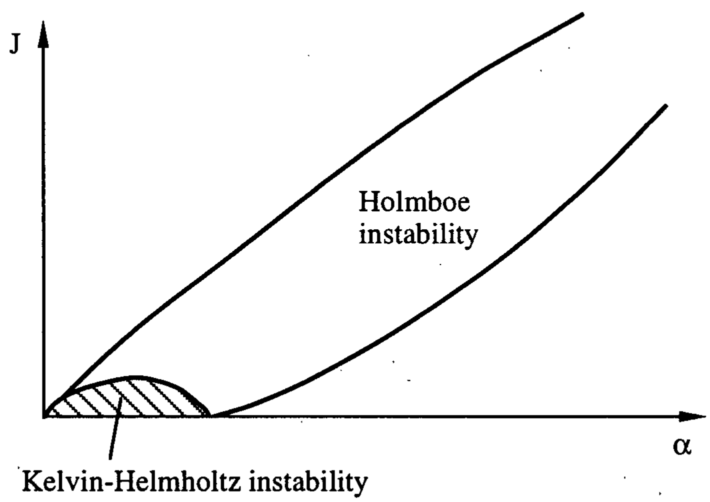

Figure 2.6 Holmboe's stability diagrams: (a) background velocity and density profiles, (b) stability diagram with K-H instability at small J and Holmboe instability at large J.

(a)

(b)

(c)

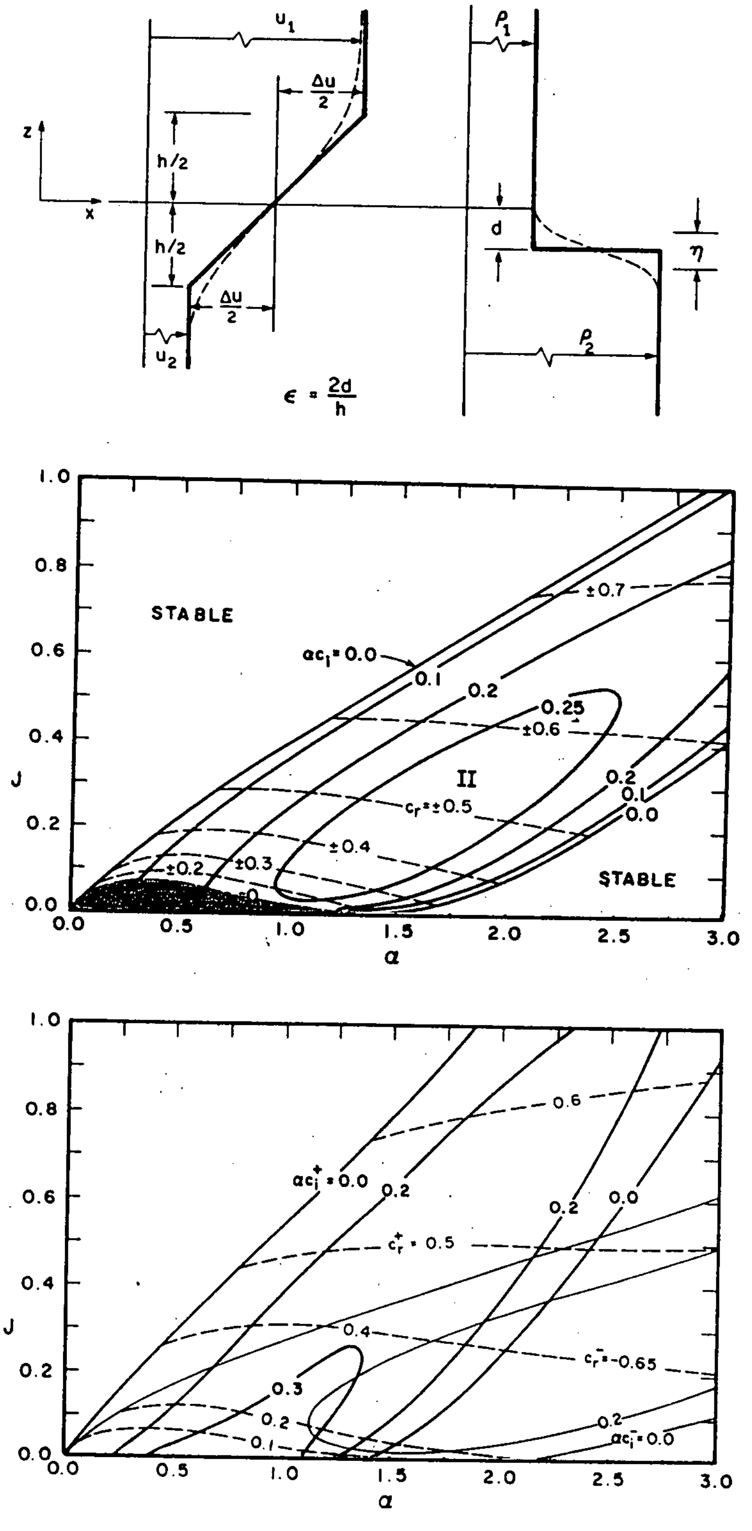

Figure 2.7 Stability diagrams for two-layer flows with piecewise linear velocity profile and two-layer density structure. (a) Definition diagram, (*h* here is the shear layer thickness), (b) stability diagrams for $\varepsilon = 0$, and (c) for $\varepsilon = -0.25$. Solid lines are contours of wave growth rate, and dash lines are contours of wave speed. (From Figs. 1, 2 and 3 of Lawrence *et al.* 1991.)

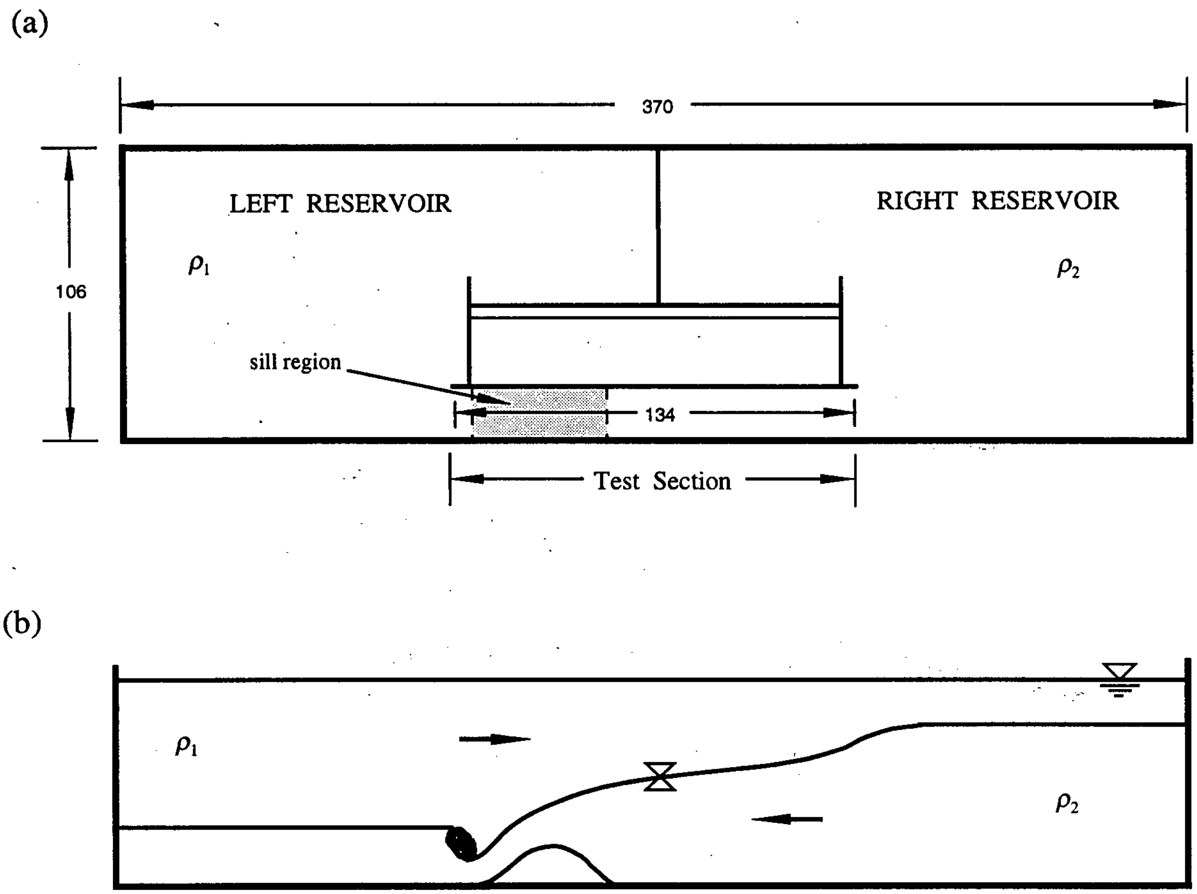

Figure 3.1 Experimental setup, (a) plan view, (b) side view. All dimensions are in centimeters. The sill is centered 31 cm from the left hand end and 103 cm from the right hand end of the channel.

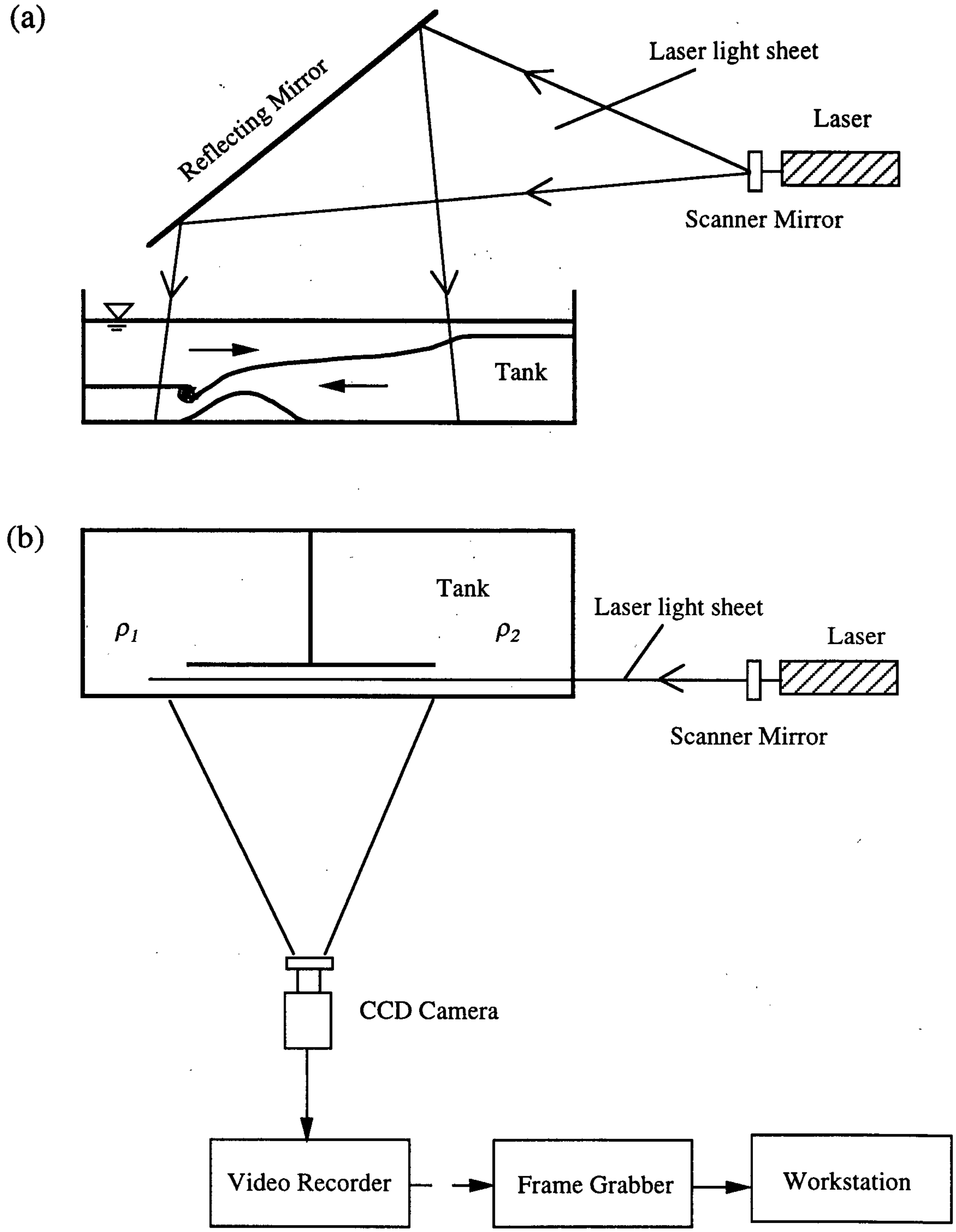

Figure 3.2 Sketch of the optical setup and data acquisition system for experiments. (a) Side view, (b) plan view.

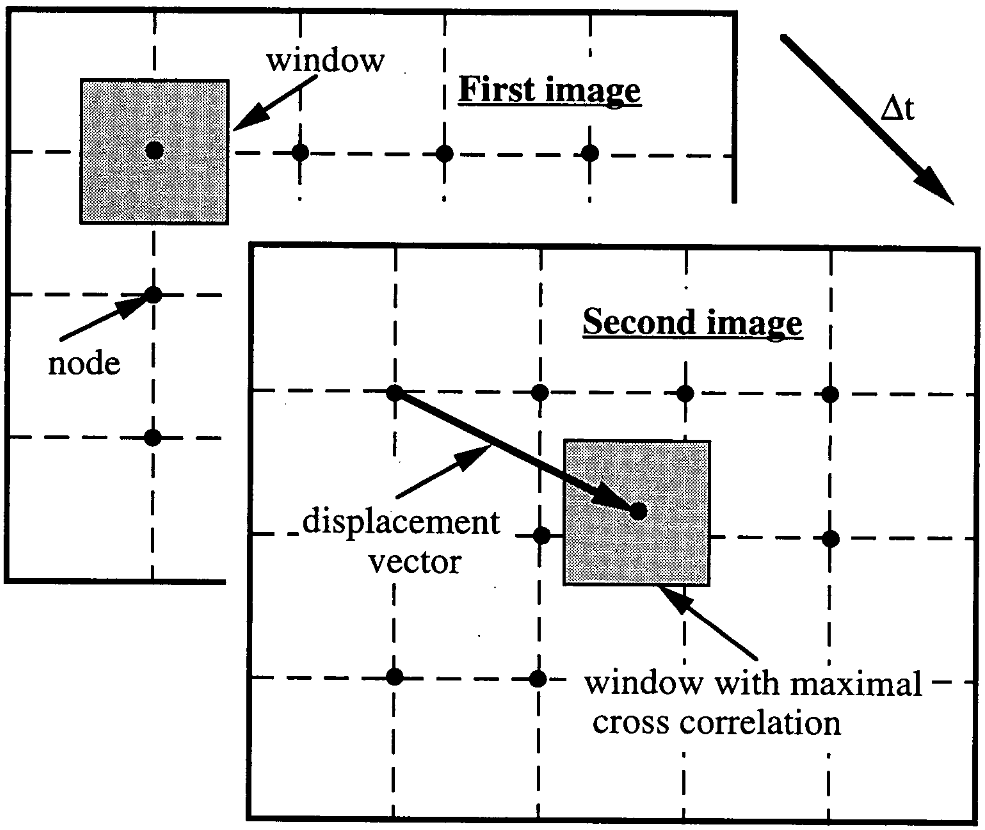

Figure 3.3 Illustration diagram of the particle tracking method. Two images are taken at Δt seconds apart. The velocity is determined for each node by searching a window with maximal cross correlation. Adopted from Stevens & Coates (1994).

(a)

(b)

(c)

(d)

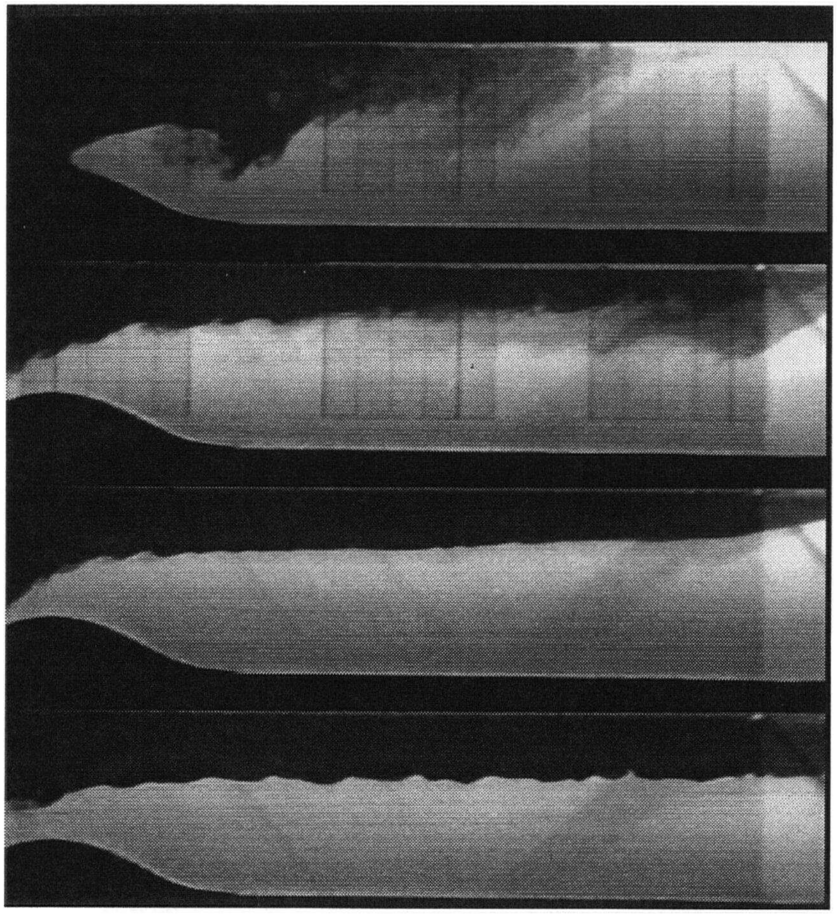

(e)

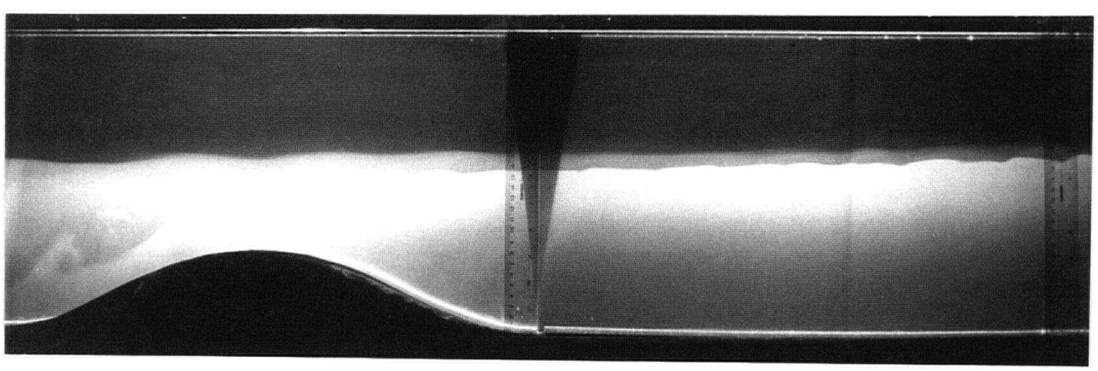

Figure 4.1 Video images showing the flow evolution in Exp. 2. (a) Gravity current, (b) unsteady exchange, (c) maximal exchange, (d) submaximal exchange, (e) exchange flow at later stage with an intermediate layer. The upper layer moves from left to right, while the lower layer from right to left. The grids in (a) and (b) are 5 cm apart.

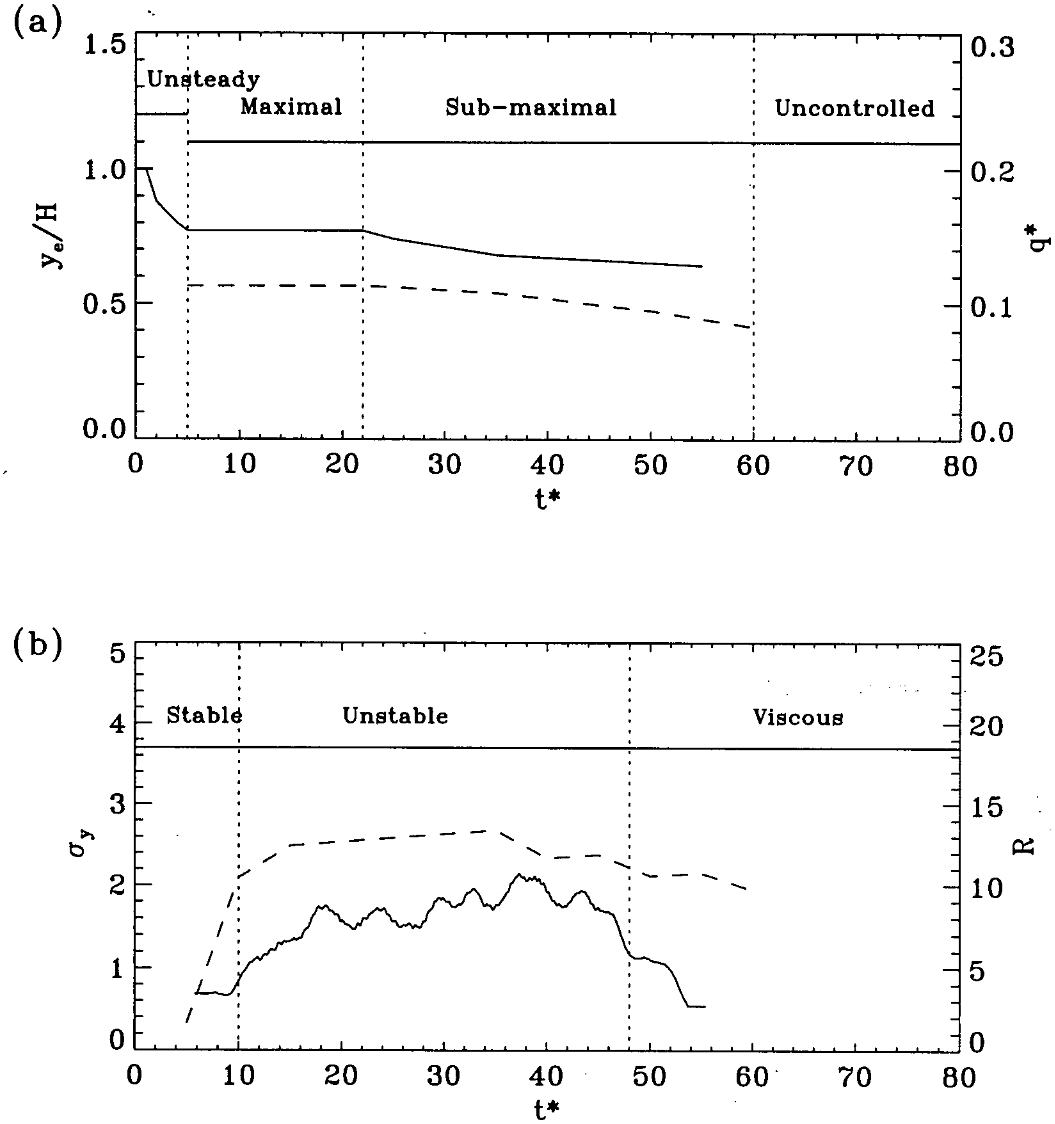

Figure 4.2 Evolution of the mean flow and interfacial wave activities in Exp. 2. (a) Evolution of the mean flow. ———, interface height at the channel right hand exit (y_e^*); – – – – , flow rate q^*. (b) Evolution of interfacial wave activities. ———, standard deviation (σ_y) of the amplitude of Holmboe waves observed in the region $x = 0.5\ L - 0.8\ L$; – – – –, the thickness ratio R. (Note: parameters are smoothed.)

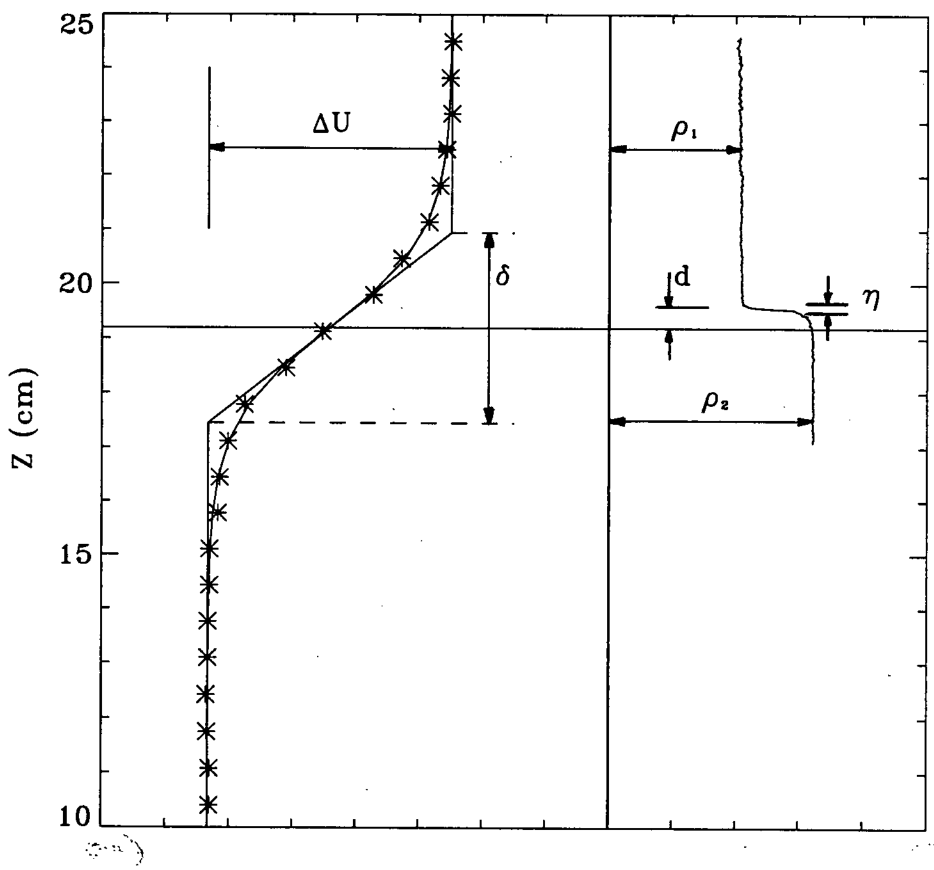

Figure 4.3 Measured velocity and density profiles in Exp. 2 at $x = 0.4\ L$ and $t^* = 16$. *, velocity measurements; ———, the fitted hyperbolic-tangent function.

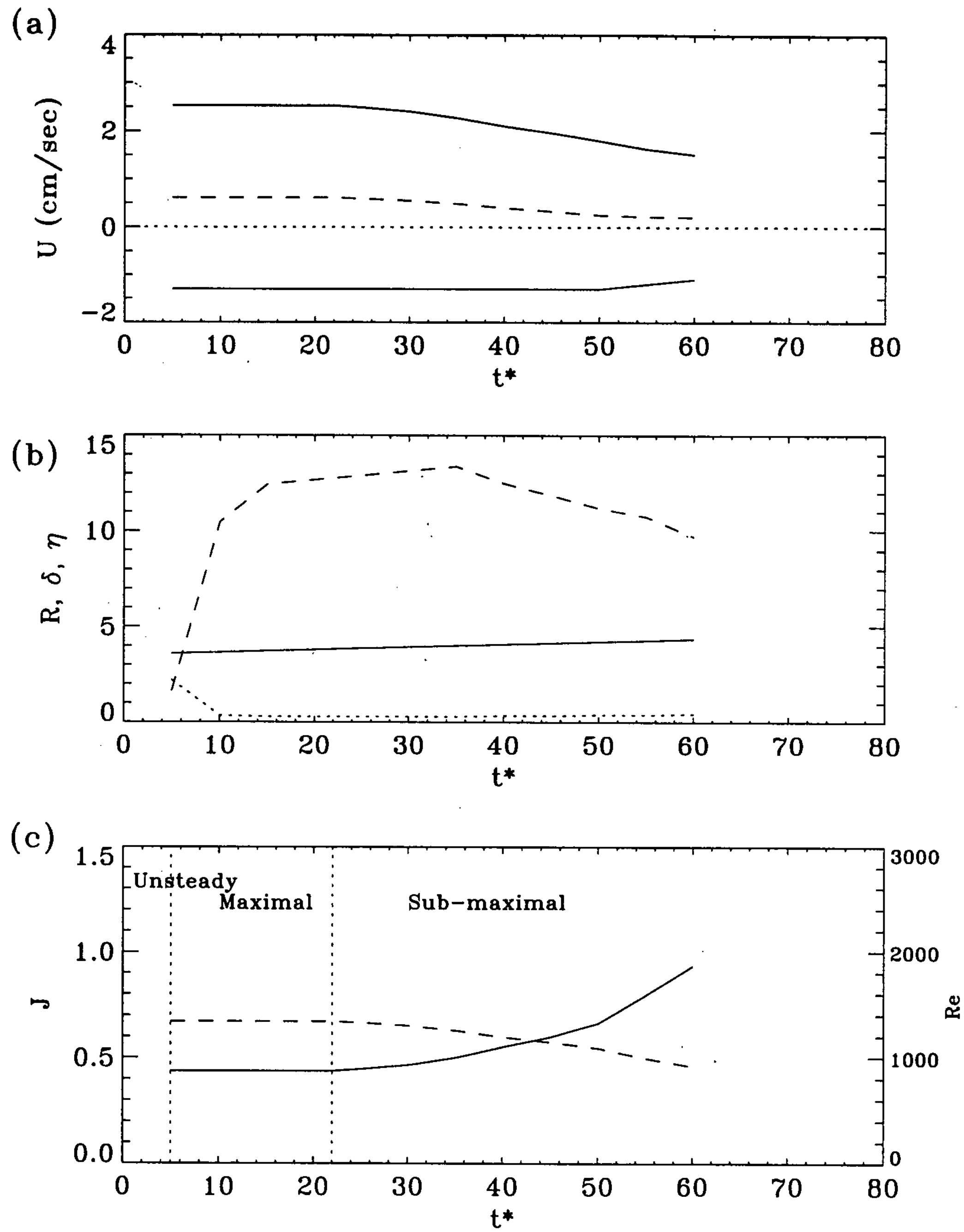

Figure 4.4 Change of flow parameters with time in Exp. 2 at $x = 0.4\ L$. (a) ——, U_1 and U_2; – – – –, $\overline{U}$. (b) ——, δ; ··········, η; – – – –, R. (c) ——, J; – – – –, Re. (Note: parameters are smoothed.)

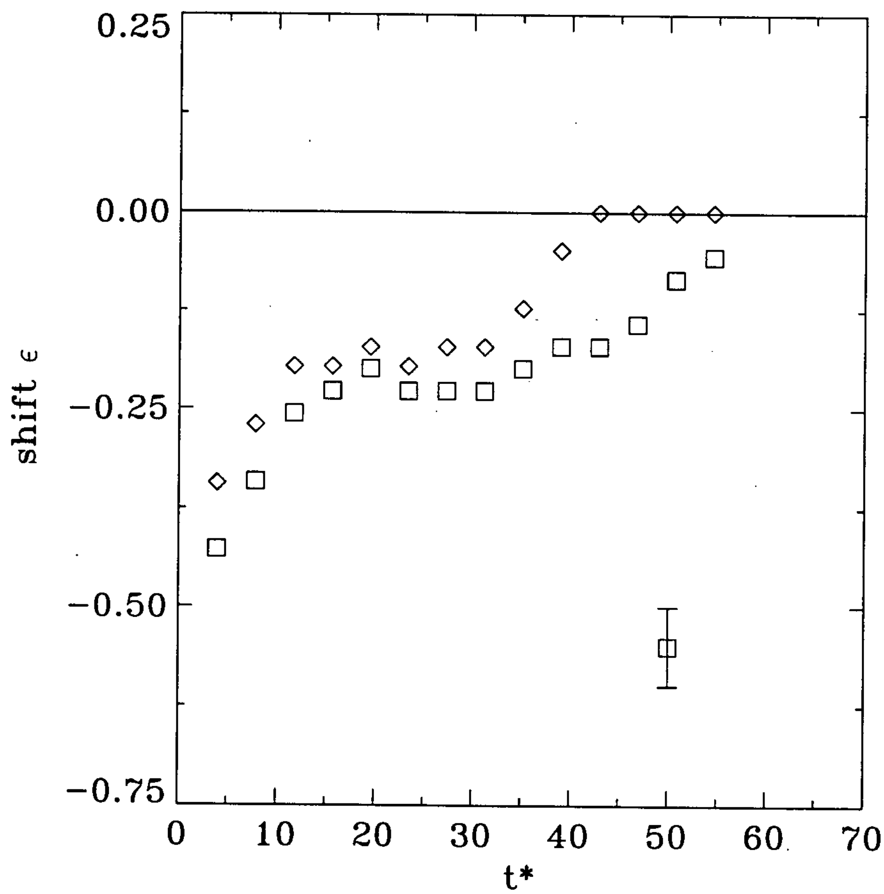

Figure 4.5 Change of the shift ε, ($\varepsilon = 2d / \delta$), with time: □ - in Exp. 2, ◊ - in Exp. 9.

(a)

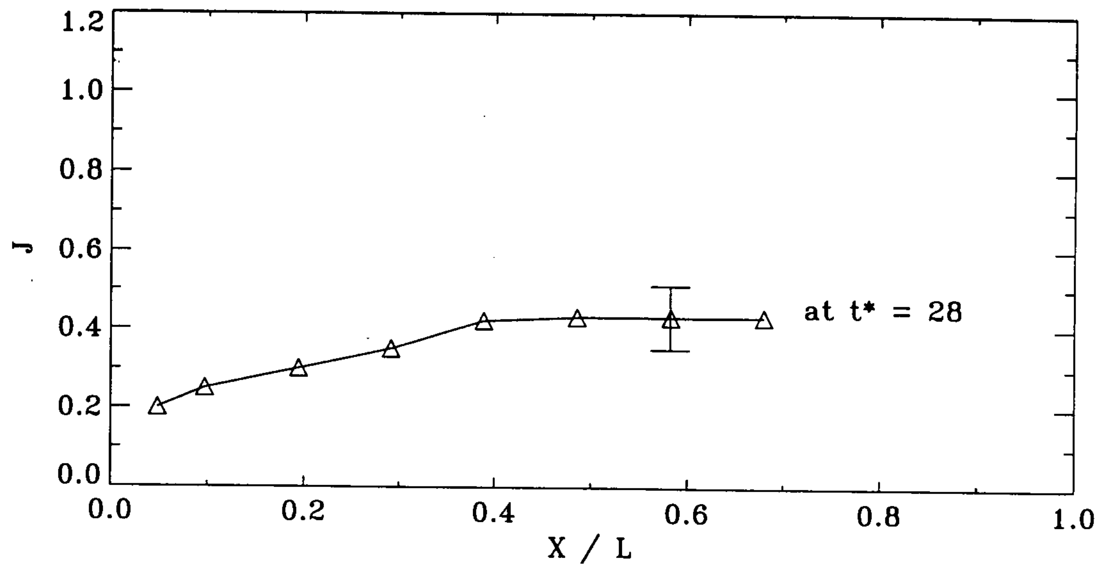

(b)

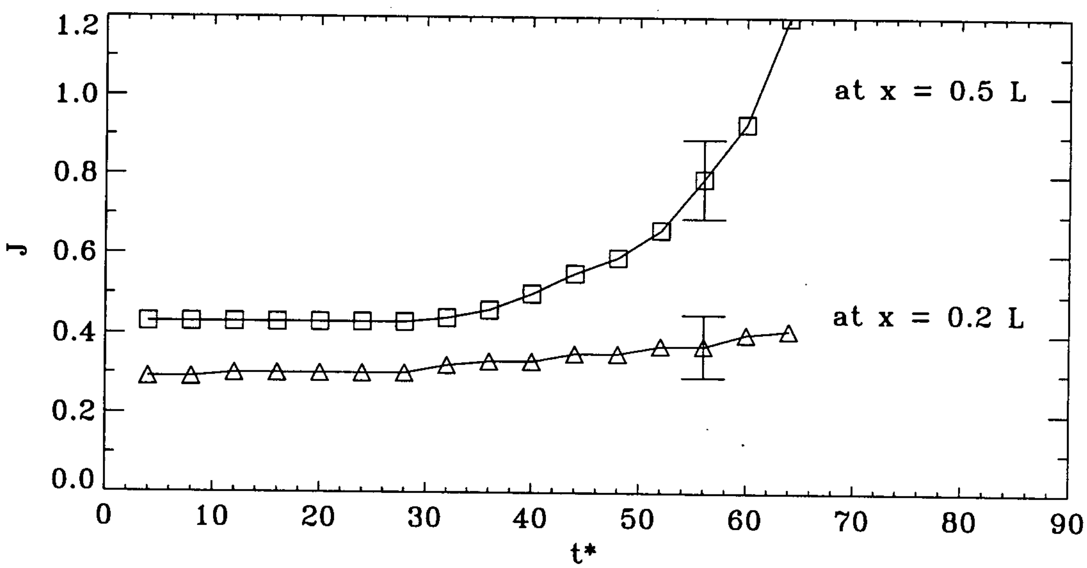

Figure 4.6 Change of J (a) with x at t^* = 28, (b) with t^* at $x = 0.2\,L$ and $x = 0.5\,L$ in Exp. 2.

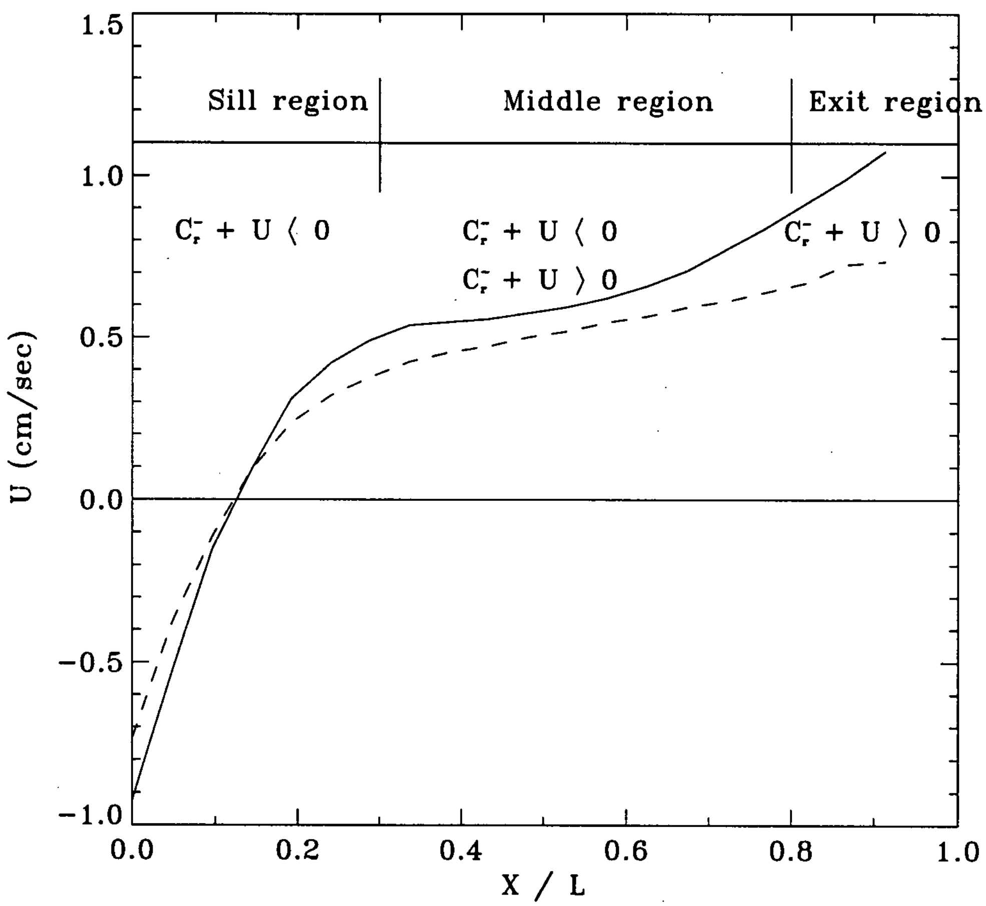

Figure 4.7 Change of the mean velocity $\overline{U}$ along the channel: ——, for maximal exchange at $t^* = 12$; – – – – , for submaximal exchange at $t^* = 30$. The whole channel can be divided into three regions: the sill region (x = 0 - 0.3 L), the middle region (x = 0.3 - 0.8 L), and the exit region (x = 0.8 - 1.0 L). Negative waves are prevented from propagating into the middle region. Positive waves can propagate towards right.

(a)

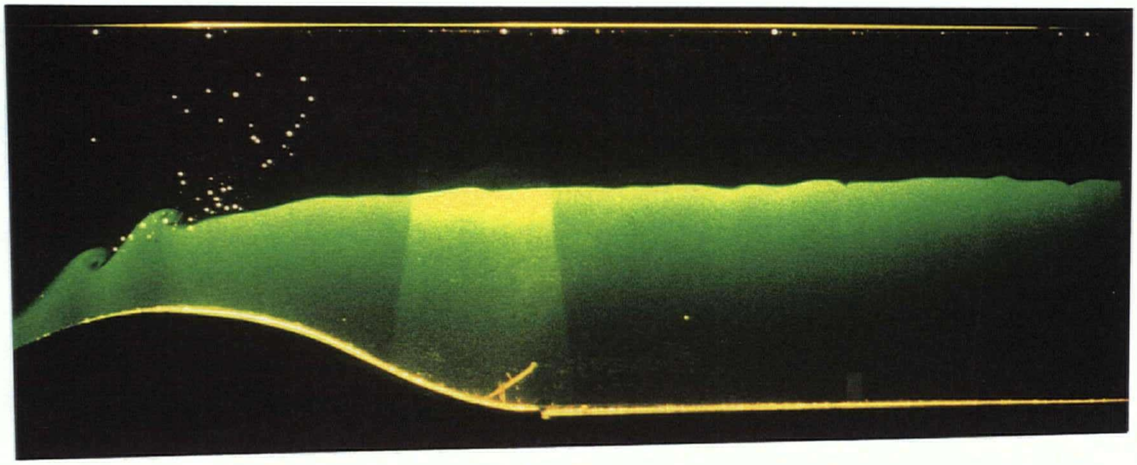

(b)

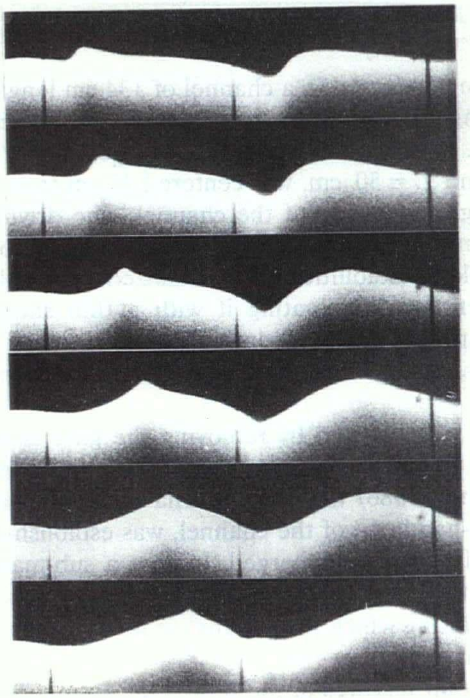

Figure 4.8 Photos showing interfacial instabilities in exchange flow over a sill. (a) Kelvin-Helmholtz instabilities are observed to the left of the sill crest, and Holmboe instabilities are observed in the right part of the photo. (b) Series of photos showing Holmboe instabilities: $J \approx 0.4$, and $\overline{U} \approx 0.4$ cm/sec. The grid markings are 5 cm apart, and the photographs were taken at 0.5 second intervals.

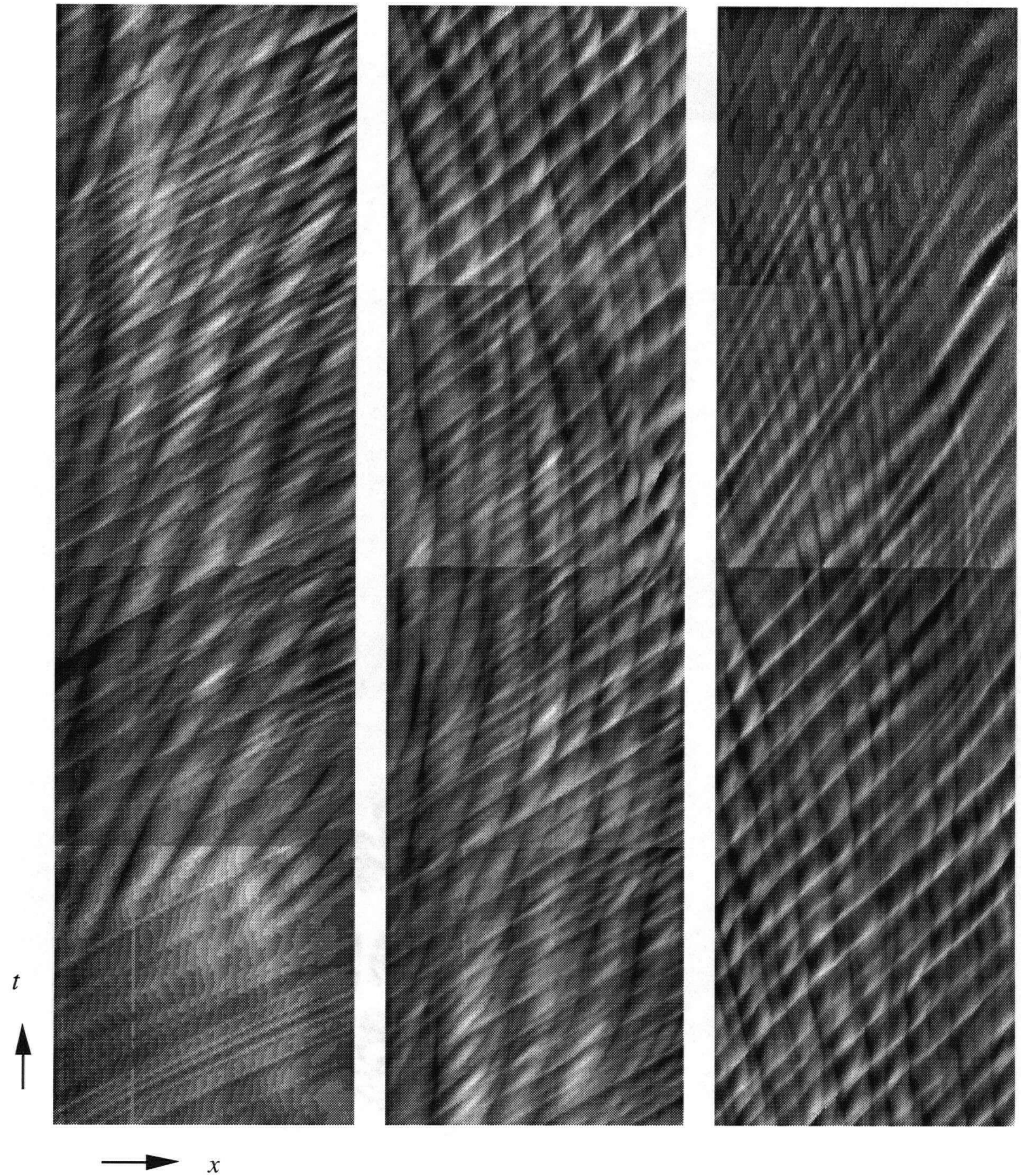

Figure 4.9 Characteristics of Holmboe waves for Exp. 9 in the region $x = 0.5L \sim 1.0L$ during the period $t^* = 8 \sim 56$. The left, middle and right strip evolves from $t^* = 8 \sim 24$, $24 \sim 40$, $40 \sim 56$, respectively. Each strip contains 240 rows, with each row representing the interface position along the channel. The intensity is a measure of the height of the interface: brighter shading stands for higher interface. Oblique bands of dark and light show the propagation of positive and negative waves.

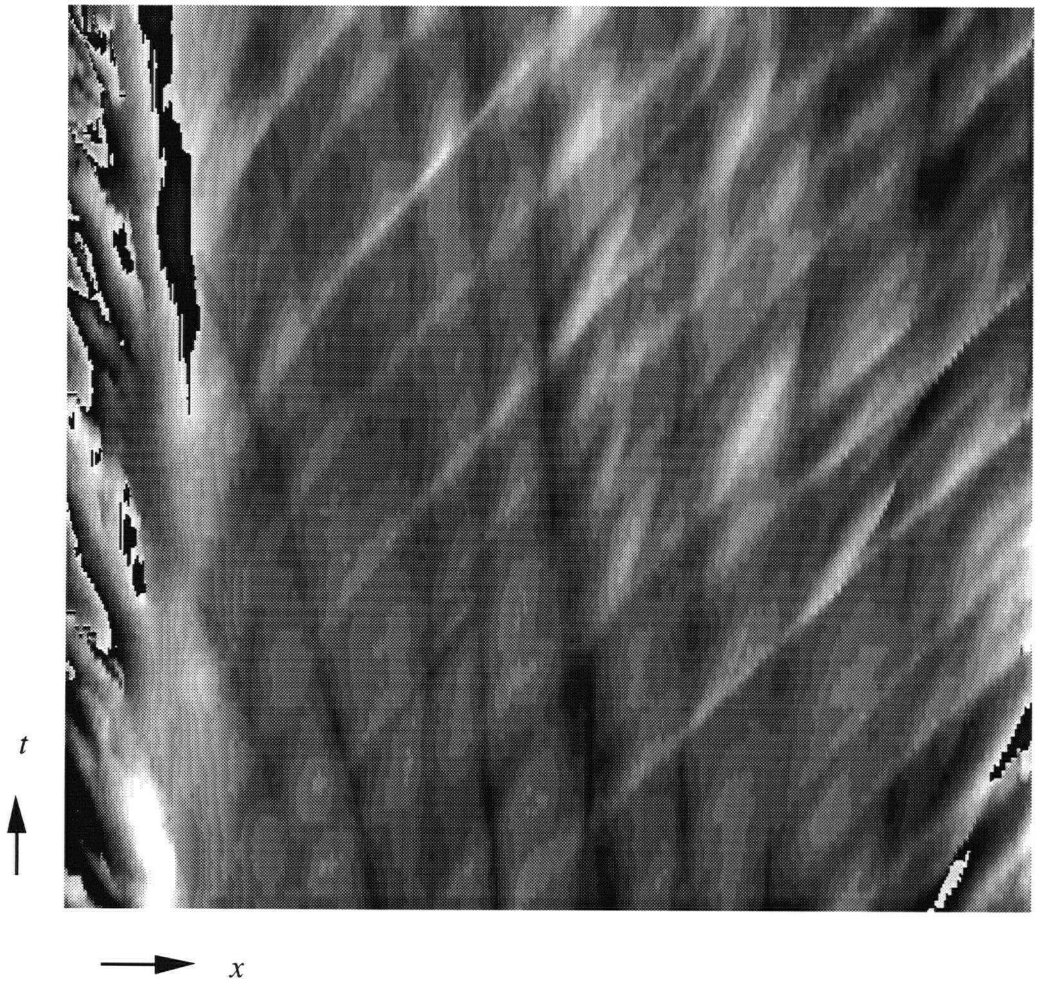

Figure 4.10 Characteristics of Holmboe waves for Exp. 2 in the region $x = -0.1L \sim 1.1L$ during the period $t^* = 36 \sim 40$. The positive and negative waves are seen as bright and dark bands. The positive waves can be traced to the sill region, while negative waves are locally grown.

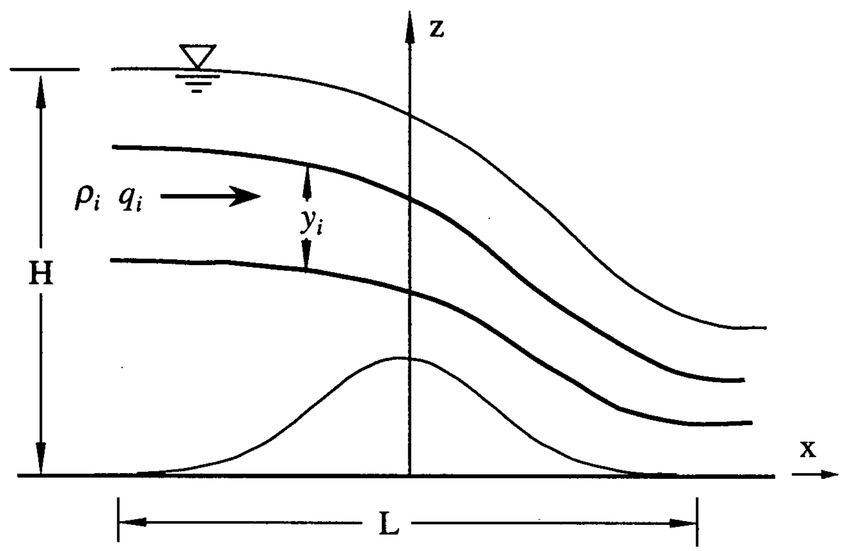

Figure 5.1 Schematic diagram of a multi-layer flow over a sill.

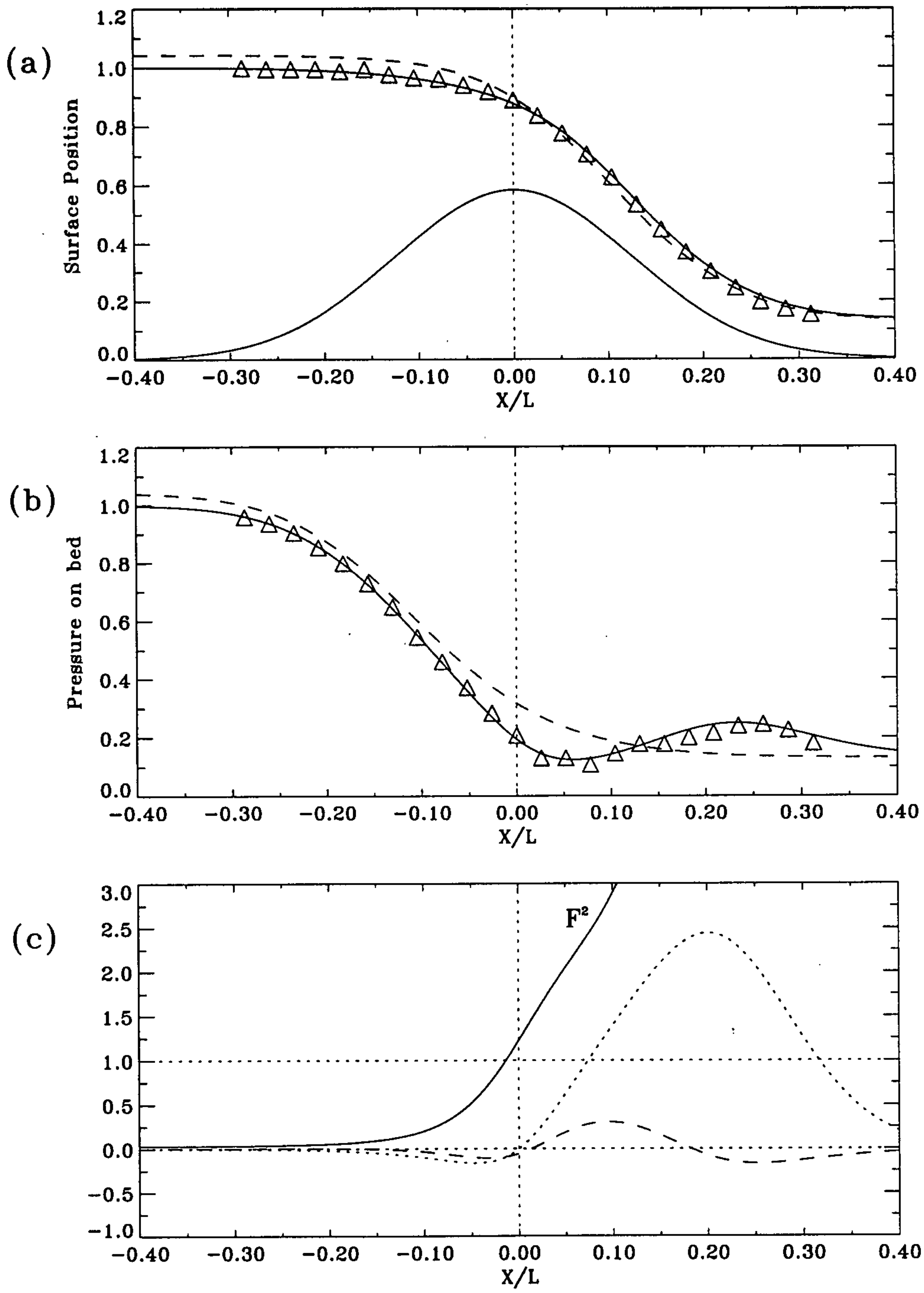

Figure 5.2 Comparison of the predictions of the extended theory with the experiment of Sivakumaran *et al.* (1983) with q = 1119.7 cm^2/s and E = 34.8 cm. (a) Surface position, (b) bottom pressure. ———, the extended theory; – – – –, hydrostatic prediction; Δ, measurements. (c) Change of F^2, S_c and S_0 from the prediction of the extended theory. ———, F^2; – – – –, S_c; ········, $(-S_0)$

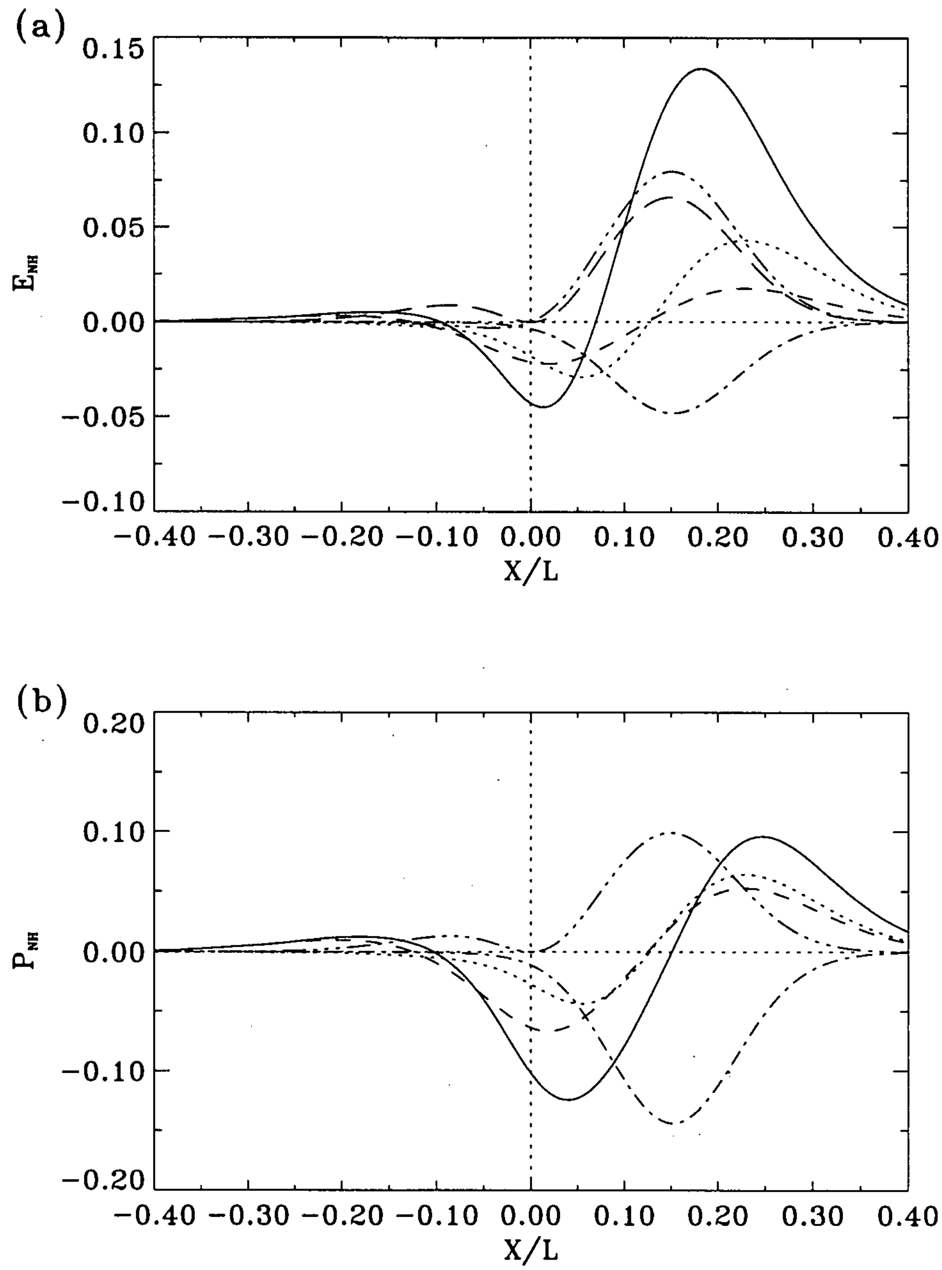

Figure 5.3 Various components in E_{NH} and P_{NH} predicted using the extended theory for the experiment of Sivakumaran *et al.* (1983). (a) E_{NH}, (b) P_{NH}. ———, total; ········, term due to s_{xx}; – – – –, term due to h_{xx}; — — —, term due to h_x, – · – · – · –, term due to s_x; —···— ···—, term due to $s_x h_x$.

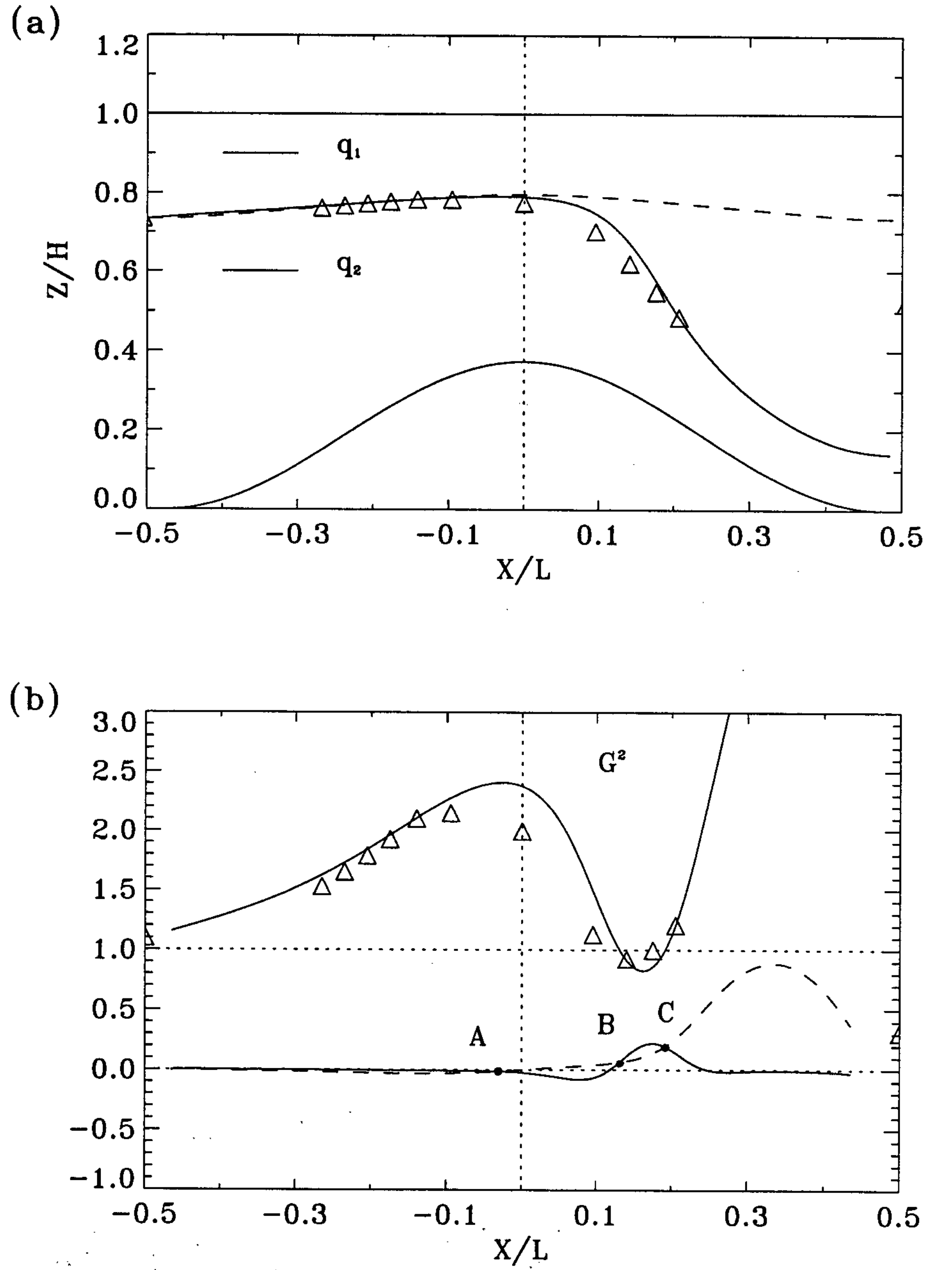

Figure 5.4 Comparison of the predictions of the extended theory with Exp. 17 of Lawrence (1993). (a) Interface position: ———, prediction of the extended theory; − − − −, hydrostatic prediction, Δ, measurements. (b) G^2, S_0 and S_c predicted using the extended theory. ———, G^2; — — —, S_c; ·······, ($-S_0$); Δ, measurements.

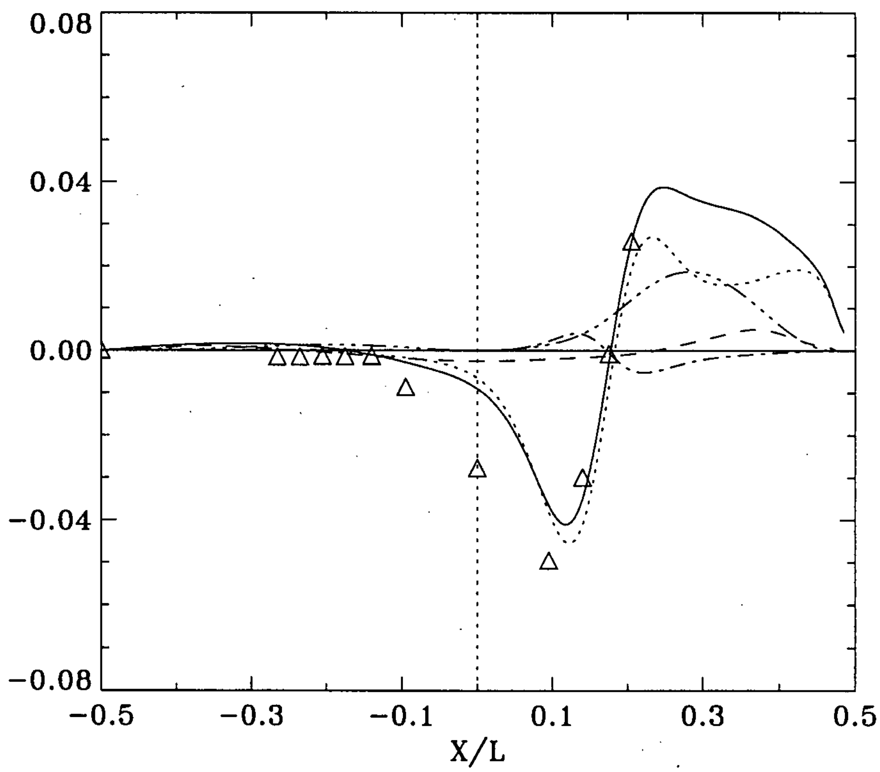

Figure 5.5 Various components in E_{NH} predicted using the extended theory for Exp. 17 of Lawrence (1993). ———, total; ·········, term due to y_{xx}; − − − −, term due to h_{xx}; − · − · − · −, term due to y_x; —·· — ··—, term due to h_x. Δ, measurements.

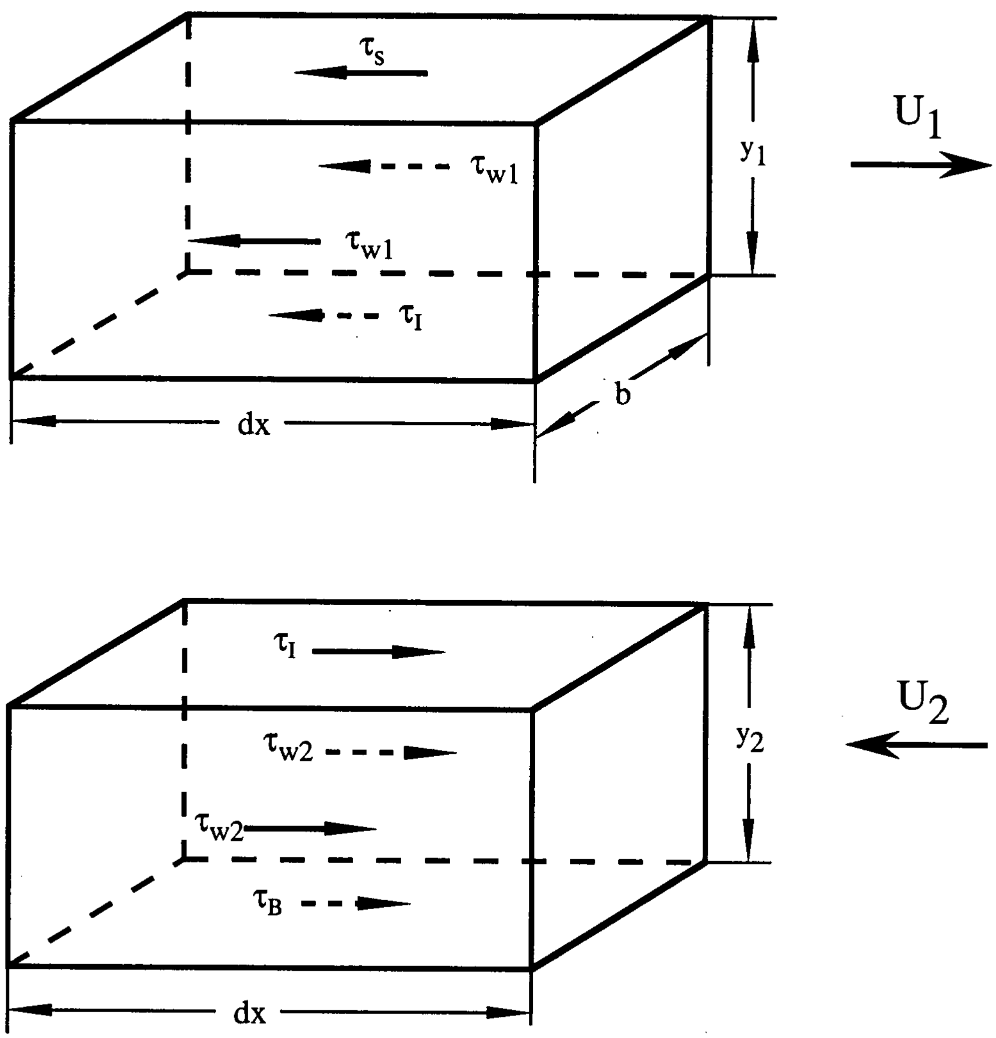

Figure 6.1 Definition sketch of the shear stresses acting on an exchange flow.

(a)

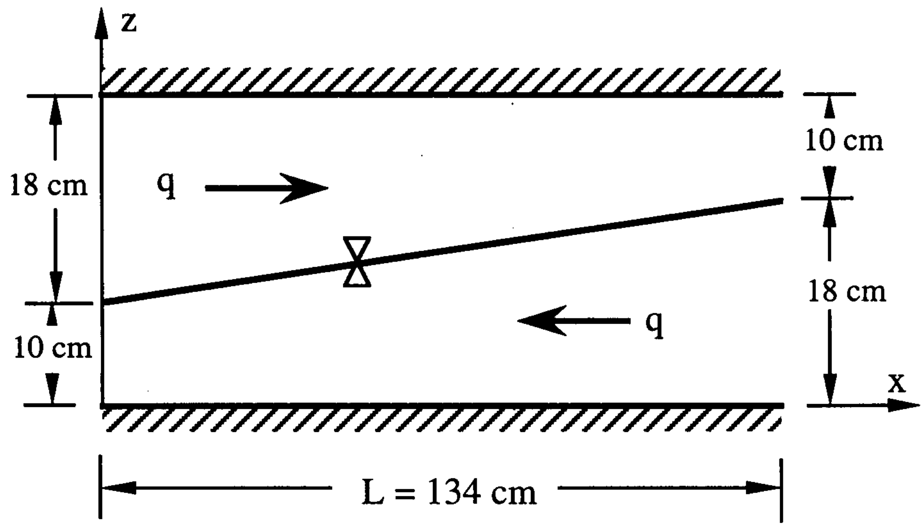

(b)

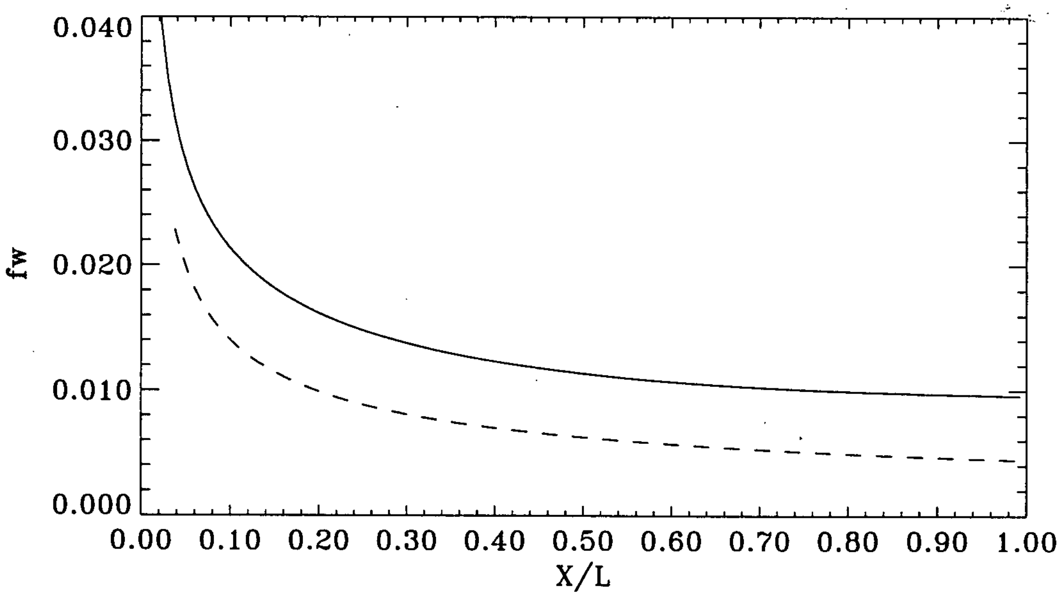

Figure 6.2 Wall friction factor for an exchange flow with a surface lid and constant interface slope. The flow has q = 27 cm^2/sec and b = 10 cm. (a) Schematic diagram of the flow, (b) predictions of the wall friction factor f_w for the upper layer: ———, Thwaites method; – – – –, Blasius theory.

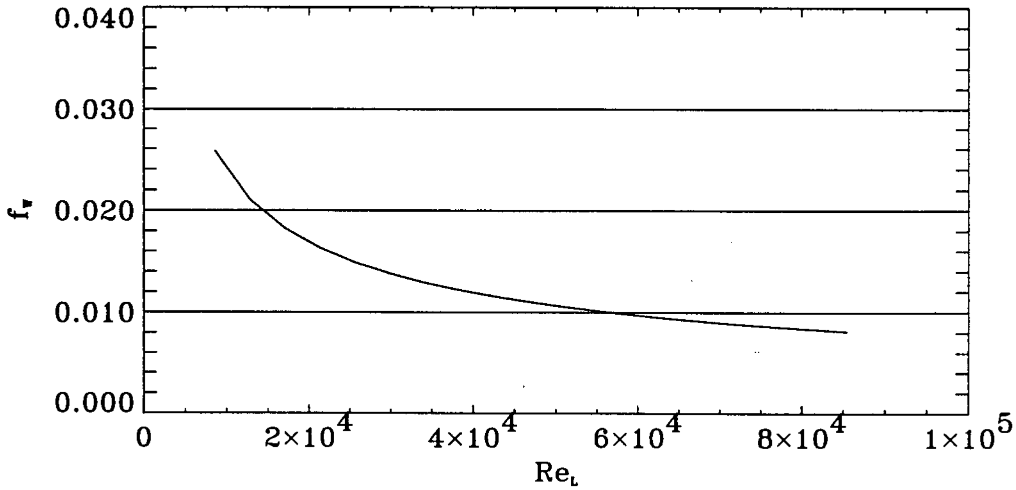

Figure 6.3 Change of the wall friction factor with Reynolds number Re_L for exchange flows with a sill of h_m = 8.0 cm, predicted using Thwaites method. $Re_L = (2q/H)L / \nu$, with $H = 28$ cm, and $L = 103$ cm.

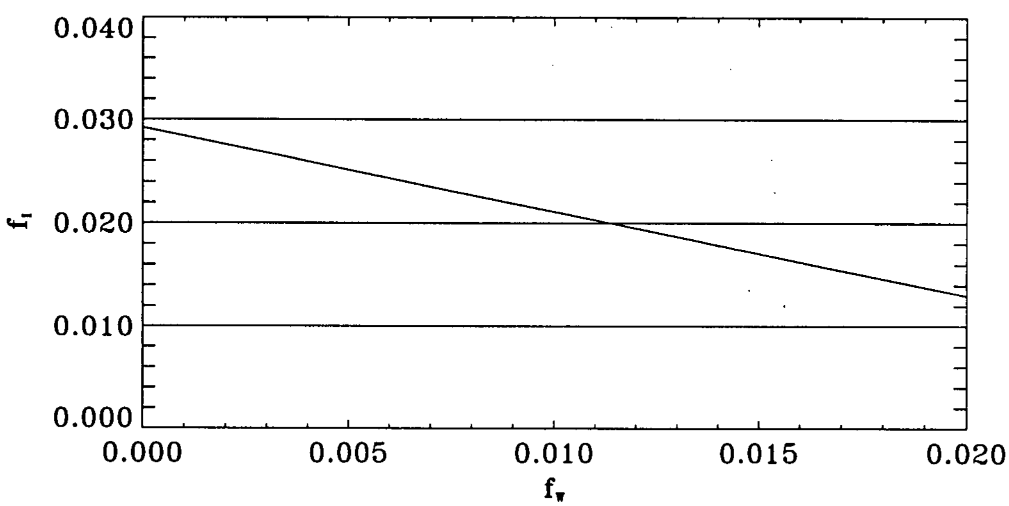

Figure 6.4 Relationship of f_w and f_I for the measured change of the internal energy in Exp. 2.

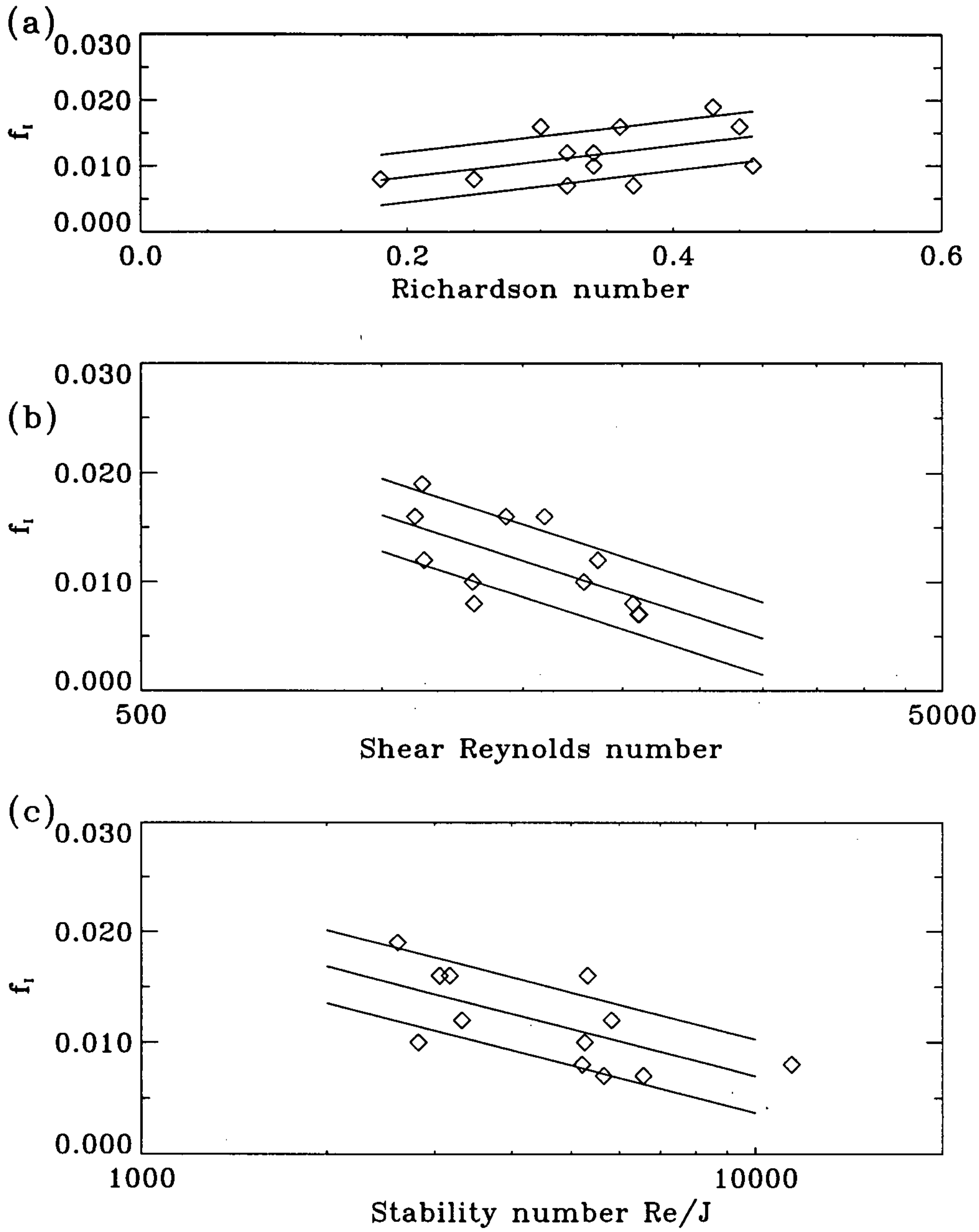

Figure 6.5 Change of the measured interfacial friction factors with interfacial flow parameters, (a) Richardson number J, (b) shear Reynolds number Re, and (c) Keulegan number $K = Re/J$. ◊, measurements; ———, the best fit and plus or minus one standard deviation.

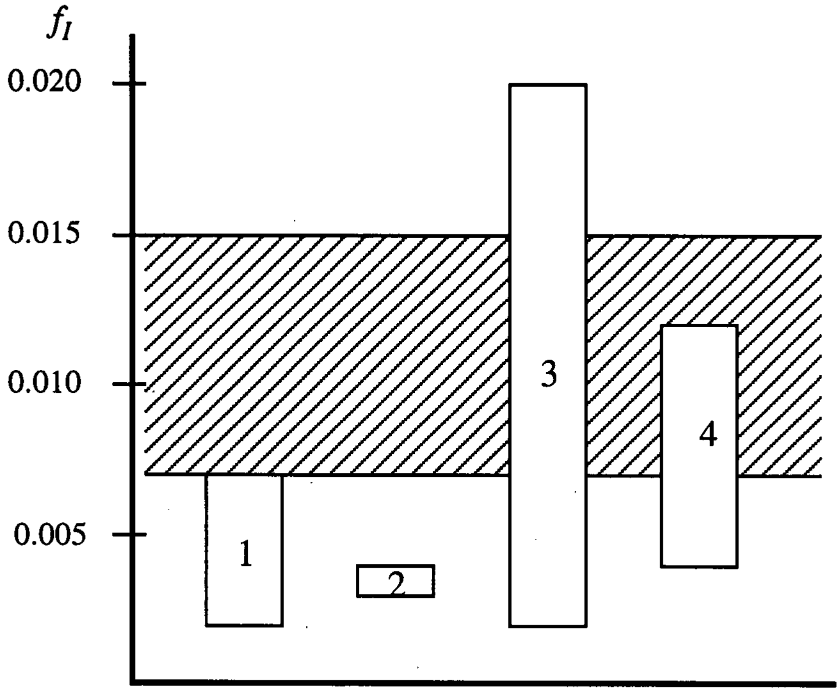

Figure 6.6 Comparison of the predictions of f_I using various methods with the measurements. 1, Dermissis & Partheniades (1984); 2, Abraham & Eysink (1971); 3, Grubert (1989); 4, Arita & Jirka (1987); shaded area, the measurements.

(a)

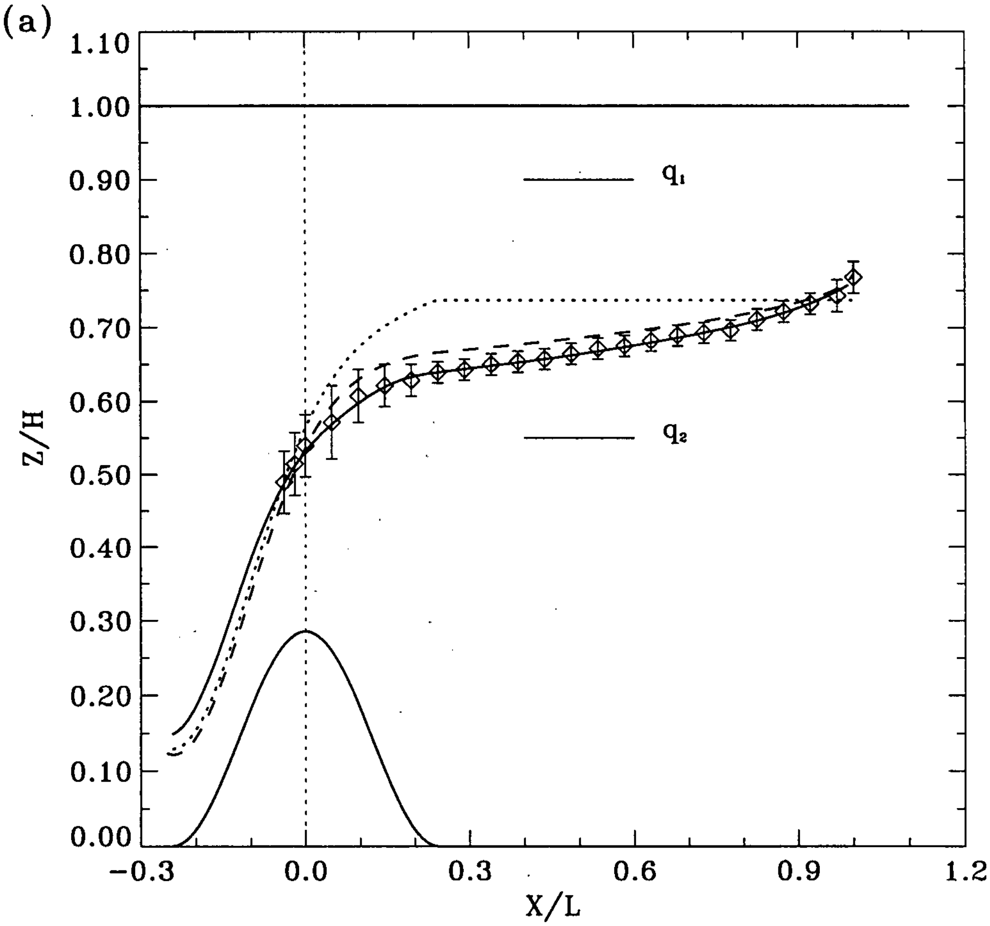

Figure 6.7 Comparison of theoretical predictions with the measurements in Exp. 2, (a) interface position, (b) E_H, (c) G^2. ·········, inviscid hydrostatic theory; – – – –, hydrostatic theory with friction; ———, non-hydrostatic theory with friction; ◊, the measurements with error bar. Friction factors are $f_w = 0.017$ and $f_I = 0.016$.

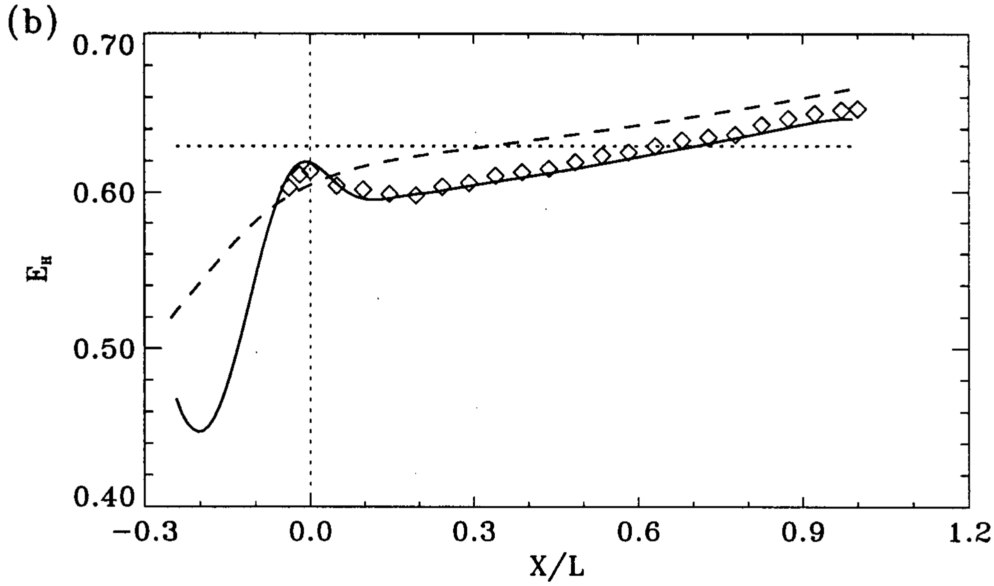

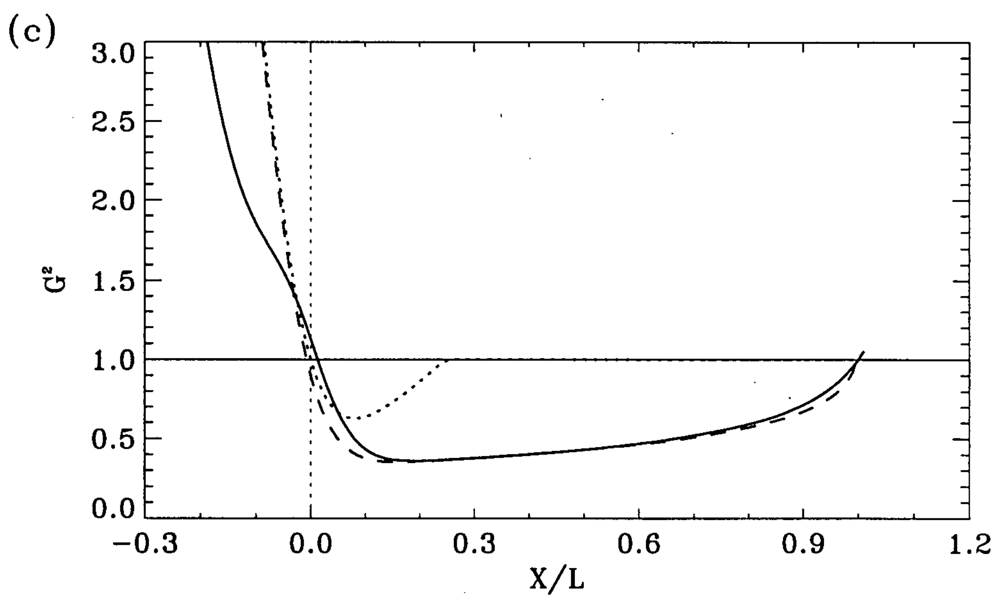

Figure 6.7 For captions, see previous page.

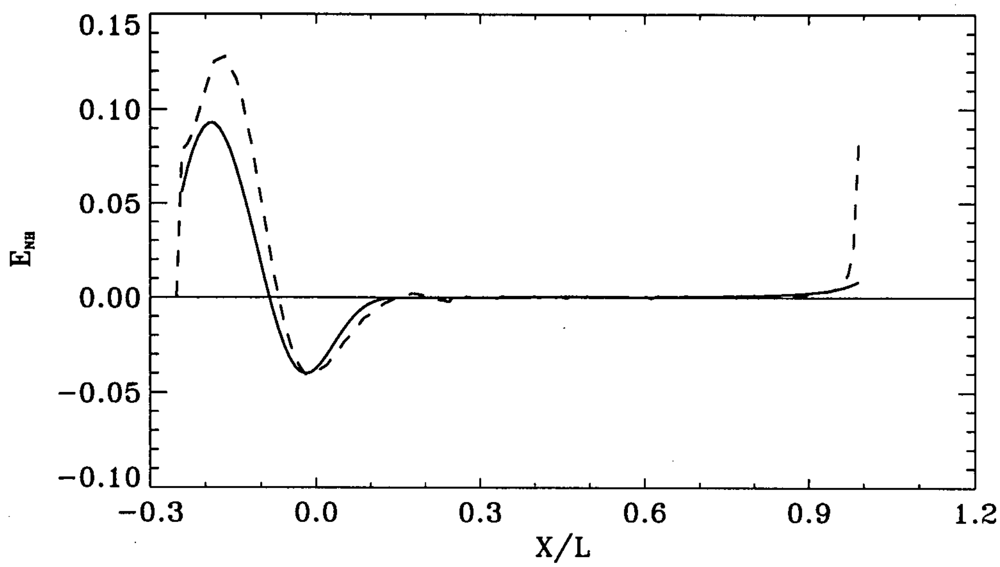

Figure 6.8 E_{NH} along the channel for Exp. 2. ——, predicted using the extended theory; – – – –, calculated from the hydrostatic prediction.

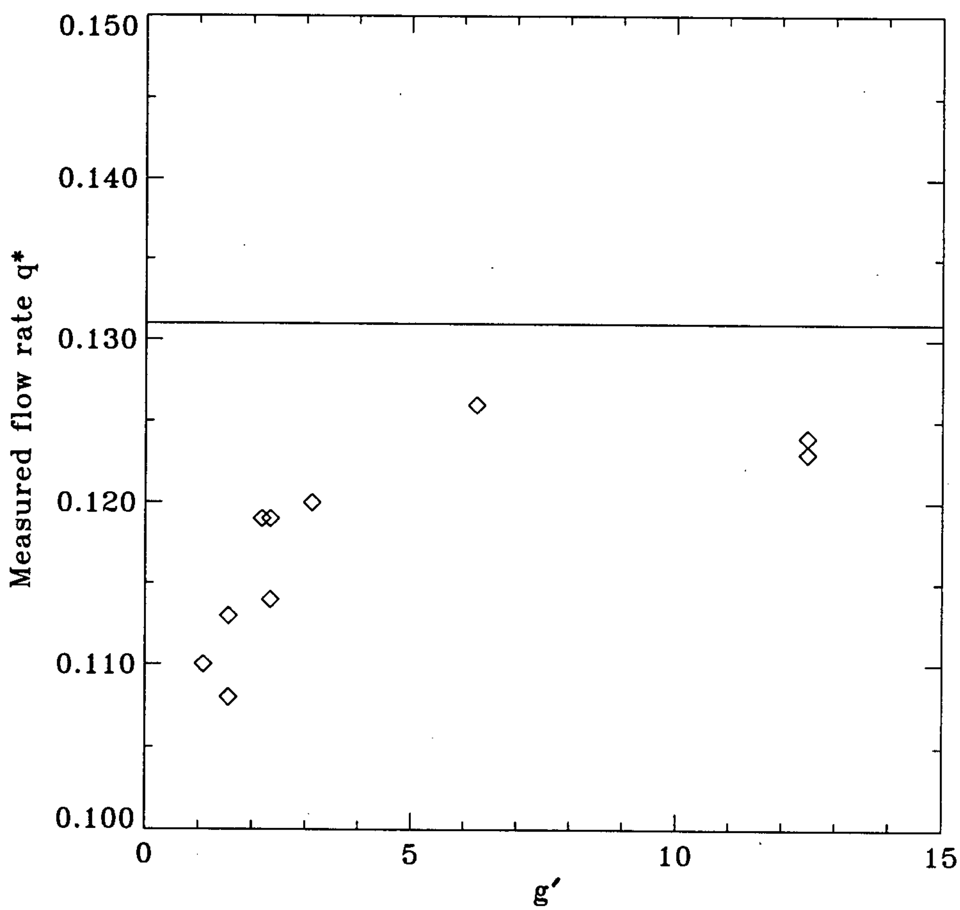

Figure 6.9 Change of the flow rate q^* with g' for all the experimental measurements.

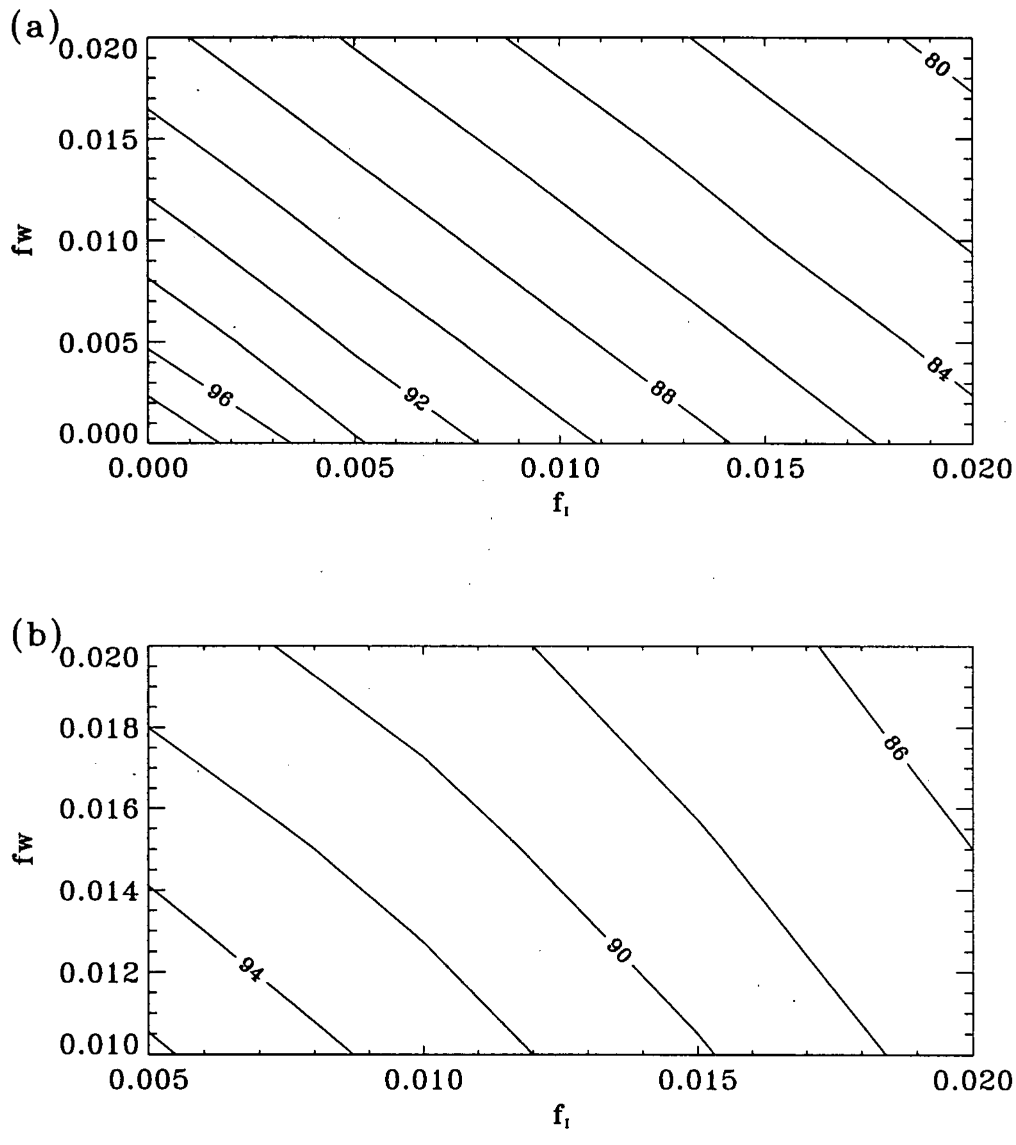

Figure 6.10 Predicted flow rate q^* given various friction factors, compared to the inviscid hydrostatic prediction (in percentage), (a) using the hydrostatic theory, (b) using the non-hydrostatic theory. The flow has the same setup as in Exp. 2.

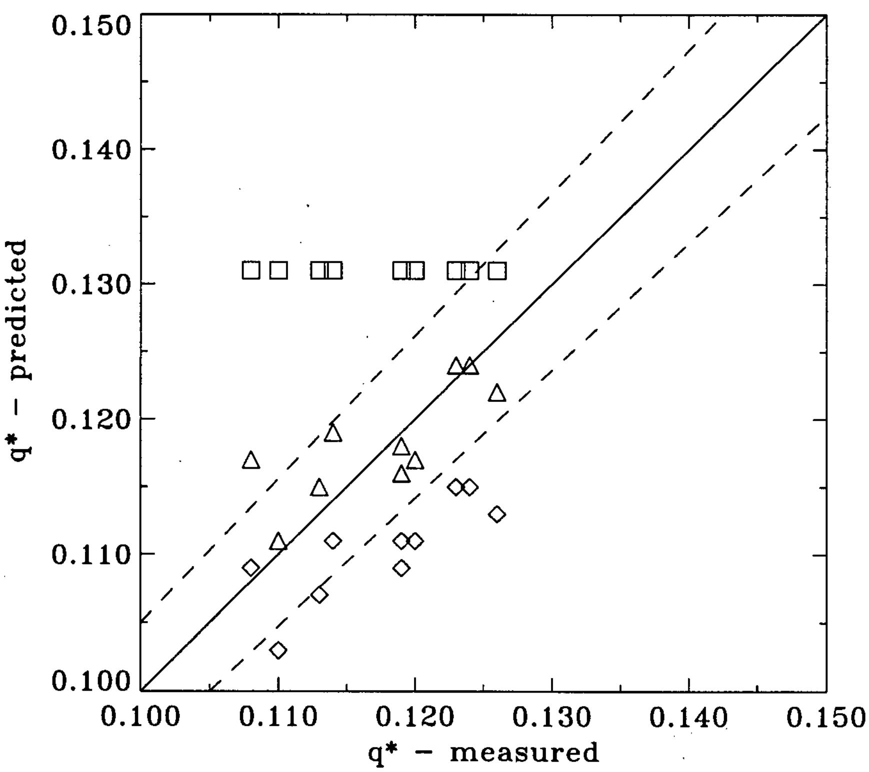

Figure 6.11 Comparison of the predicted flow rates using various theories with the measurements for Exp. 1 - Exp. 9. □ and ◊, the hydrostatic predictions without and with friction, respectively. Δ, the non-hydrostatic prediction with friction. – – – –, ± 5 % error in flow rate measurements.

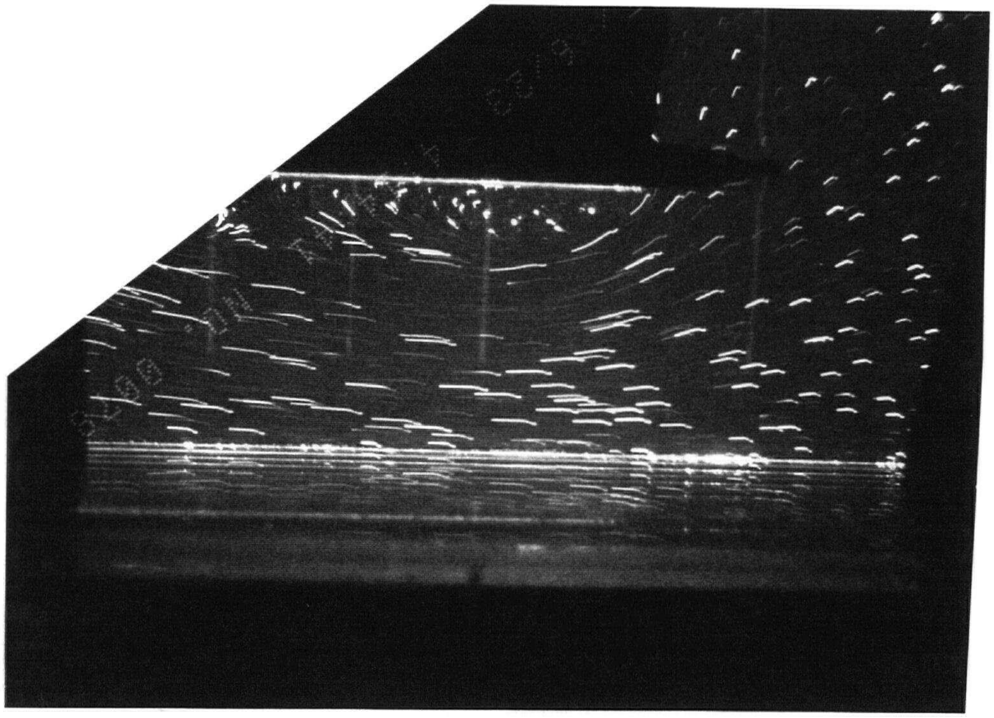

Figure 6.12 Vortex structure in the right hand exit region due to the channel sharp end for the lower layer. Photo was taken from the top. The width of the channel is 10 cm.

(a)

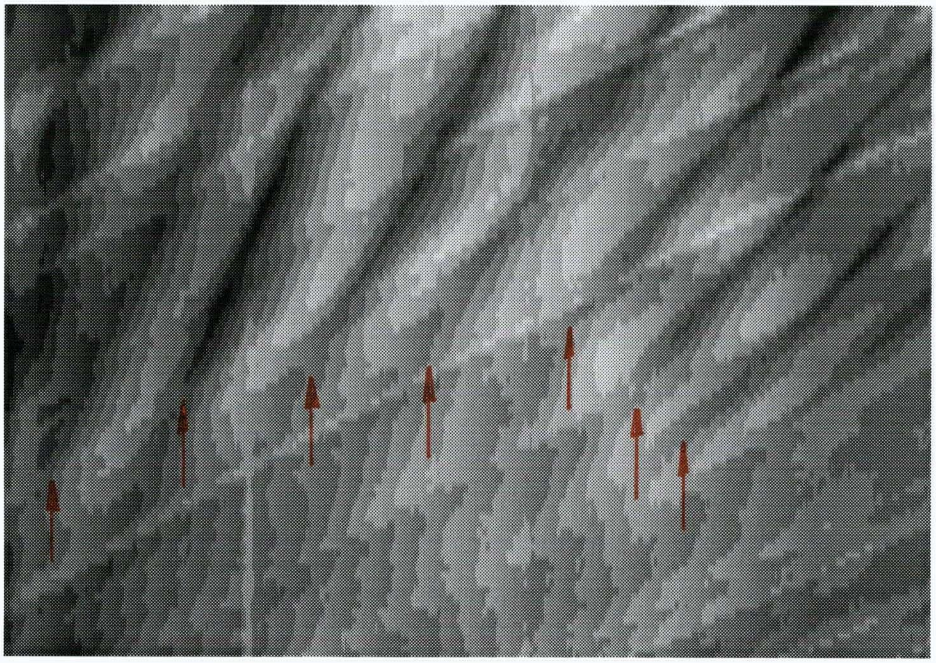

(b)

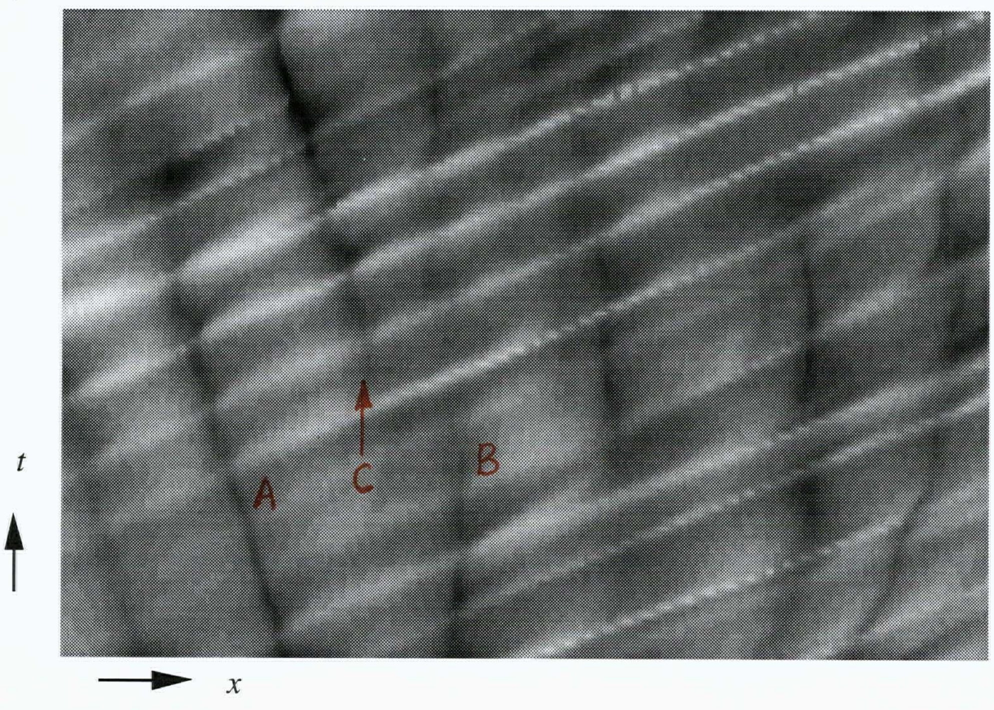

Figure 7.1 Wave characteristics showing the development of negative waves, seen as dark bands. Arrows indicate the starting points of the negative waves. (a) Exp. 9 with a horizontal length of 90 cm during the period $t^* = 10 \sim 13$, (b) Exp. 4 with a horizontal length of 50 cm during the period $t^* = 48 \sim 52$.

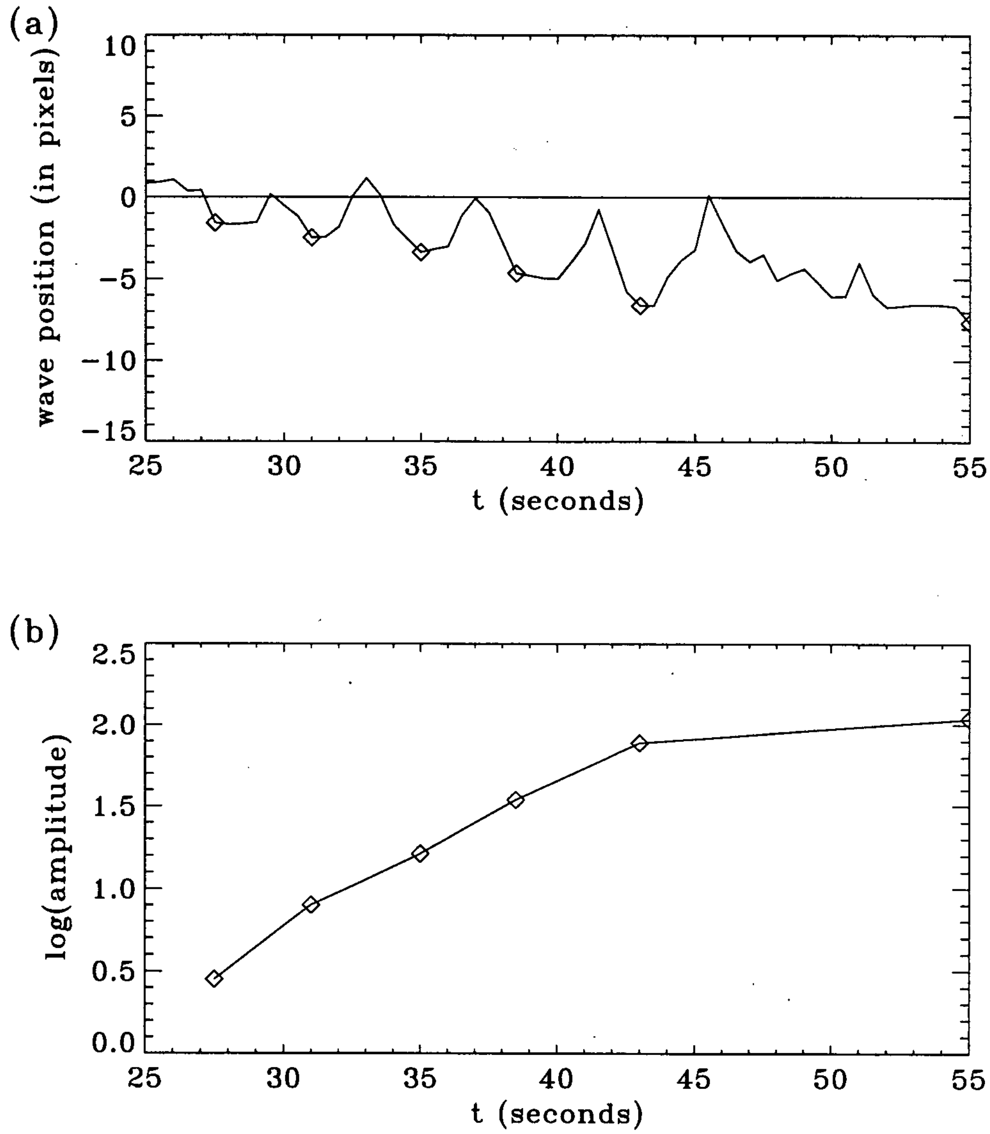

Figure 7.2 Development of the negative wave observed in Exp. 4 at $t^* = 47$ (10 minutes). (a) Development of the negative wave, (b) development of the amplitude of the negative wave. The flow has $\varepsilon \approx 0$, $J \approx 0.57$ and $Re \approx 1600$.

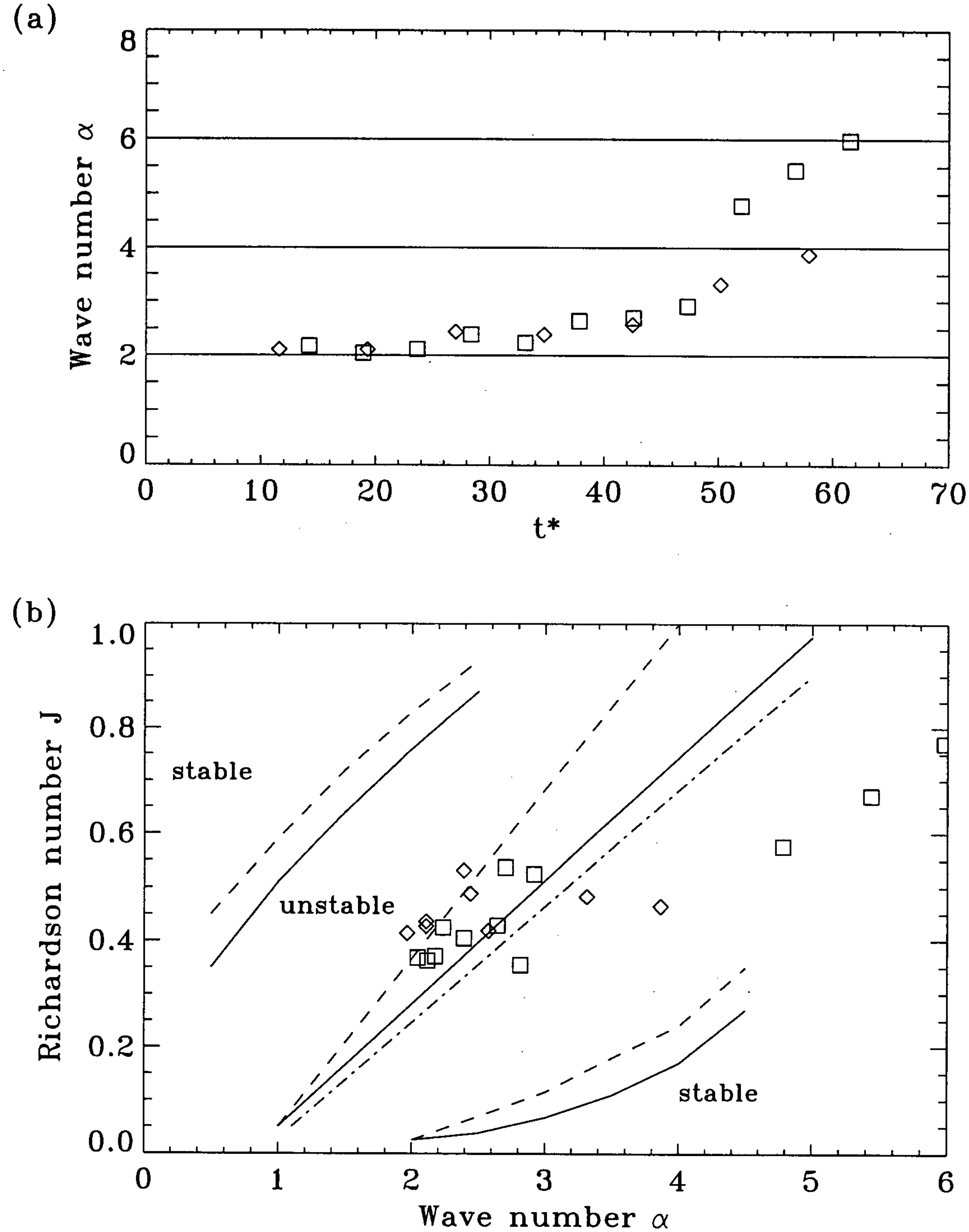

Figure 7.3 Change of the wave number of negative waves with time and with the Richardson number in Exp. 2 (◊) and Exp. 4 (□), (a) with t^*, (b) with J. ———, predictions of Haigh (1995) for the fastest growing waves and the stability boundaries for $\varepsilon = 0$; – – – –, predictions for $\varepsilon = -0.25$; – · – · – · –, prediction of Nishida & Yoshida (1987).

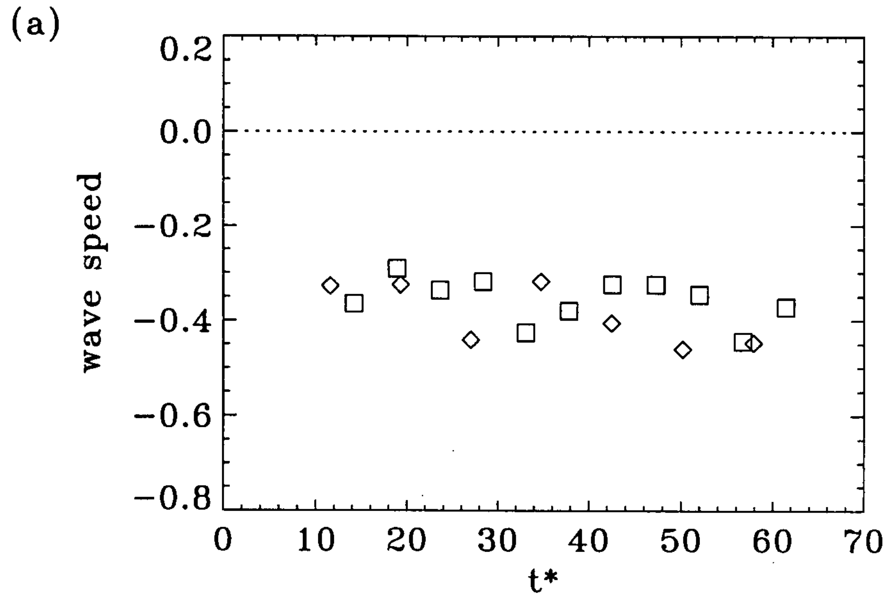

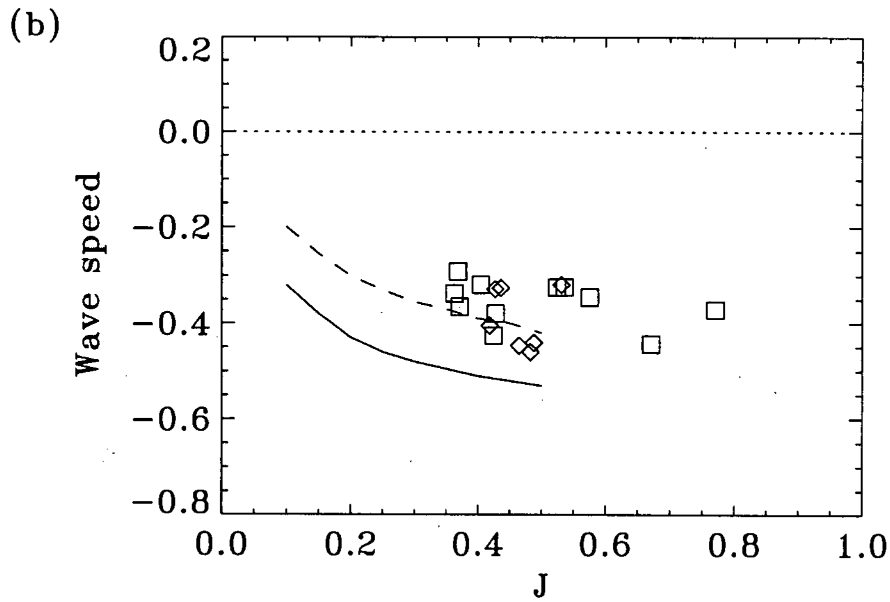

Figure 7.4 Change of the wave speed of negative waves with time and with the Richardson number in Exp. 2 (◊) and Exp. 4 (□), (a) with t^*, (b) with J. ———, predictions of Haigh (1995) for the fastest growing waves for $\varepsilon = 0$; – – – –, predictions for $\varepsilon = -0.25$.

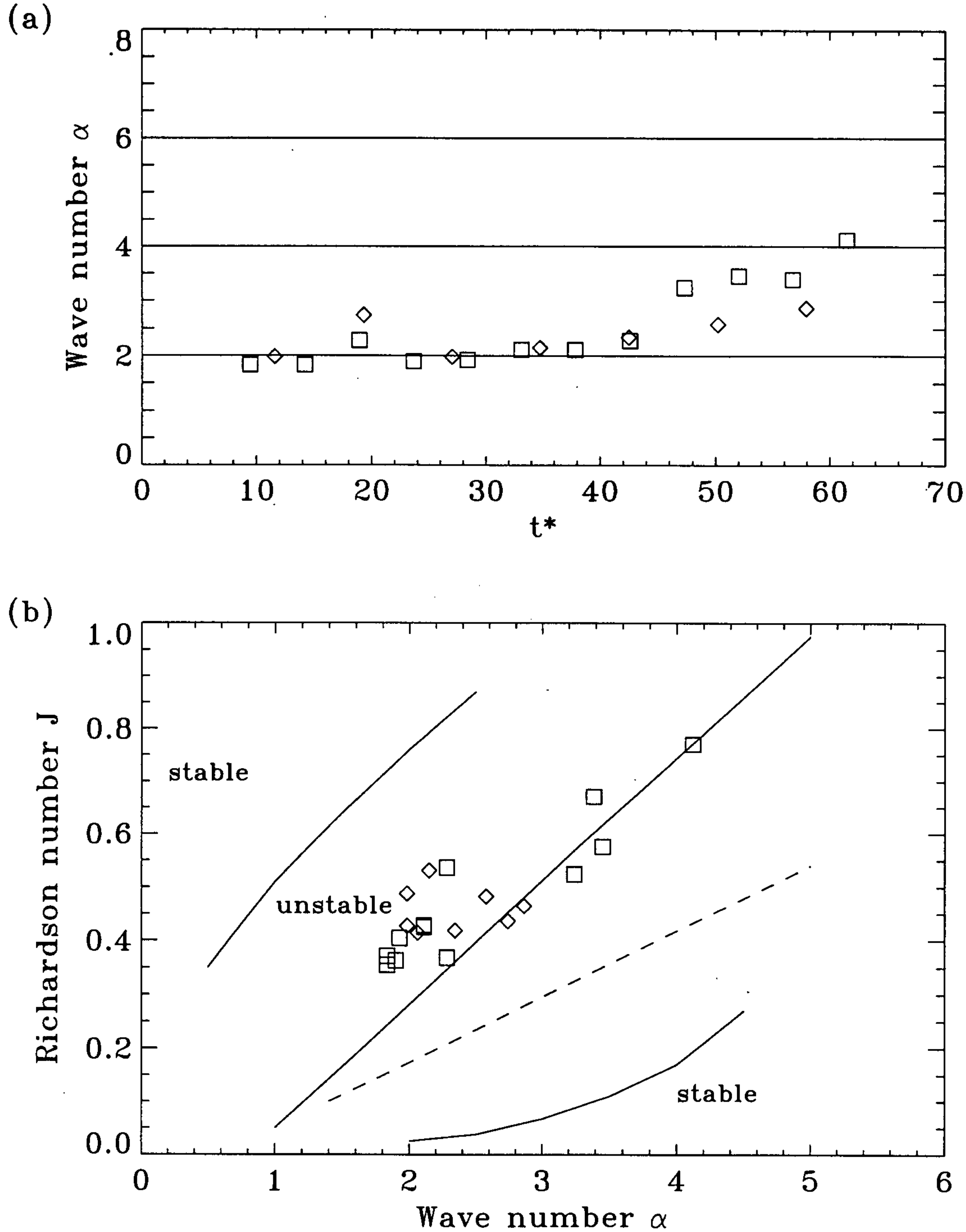

Figure 7.5 Change of the wave number of positive waves with time and with the Richardson number in Exp. 2 (◊) and Exp. 4 (□), (a) with t^*, (b) with J. ———, predictions of Haigh (1995) for the waves with the fastest growth rate, and the stability boundaries for $\varepsilon = 0$; – – – –, predictions for $\varepsilon = -0.25$.

(a)

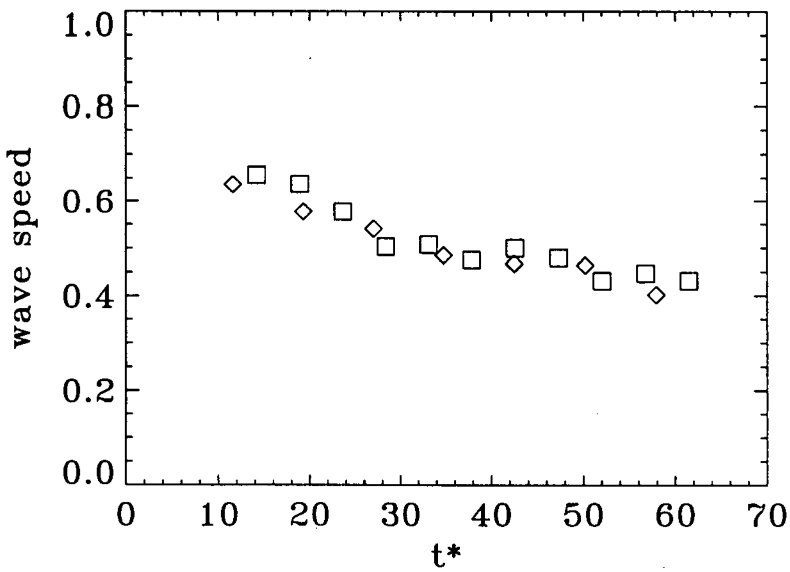

(b)

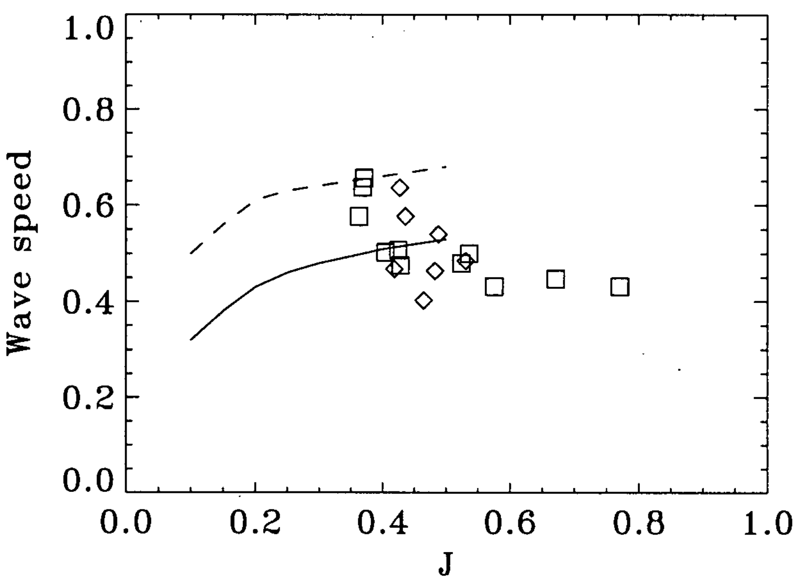

Figure 7.6 Change of the wave speed of positive waves with time and with Richardson number in Exp. 2 (◊) and Exp. 4 (□), (a) with t^*, (b) with J. ———, predictions of Haigh (1995) for the waves with the fastest growth rate for $\varepsilon = 0$; – – – –, predictions for $\varepsilon = -0.25$.

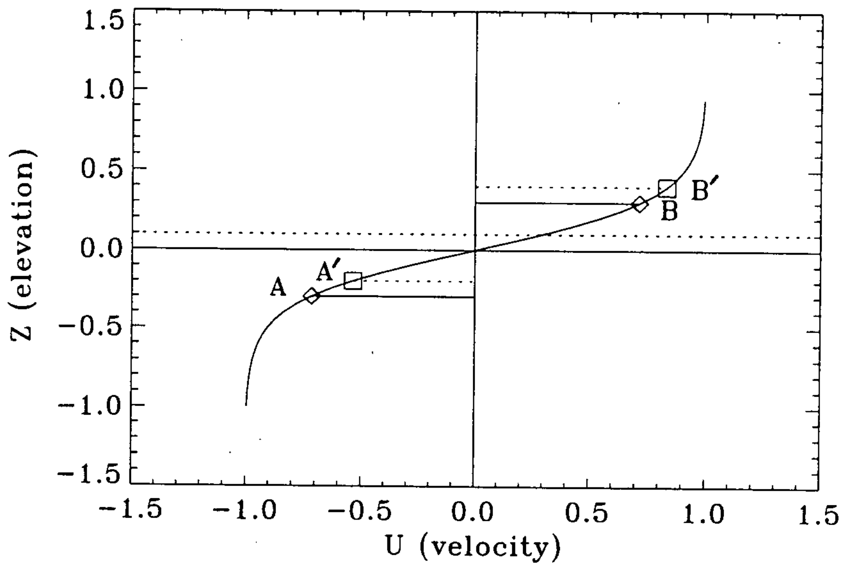

Figure 7.7 Illustration diagram for the relationship between the shift and waves speeds. ———, initial density interface (at z = 0) and positions of the critical layer (A & B) where $u(z) = c_r^{\pm}$; ·········, new density interface (at z = 0.1) and new positions of the critical layer (A' & B').

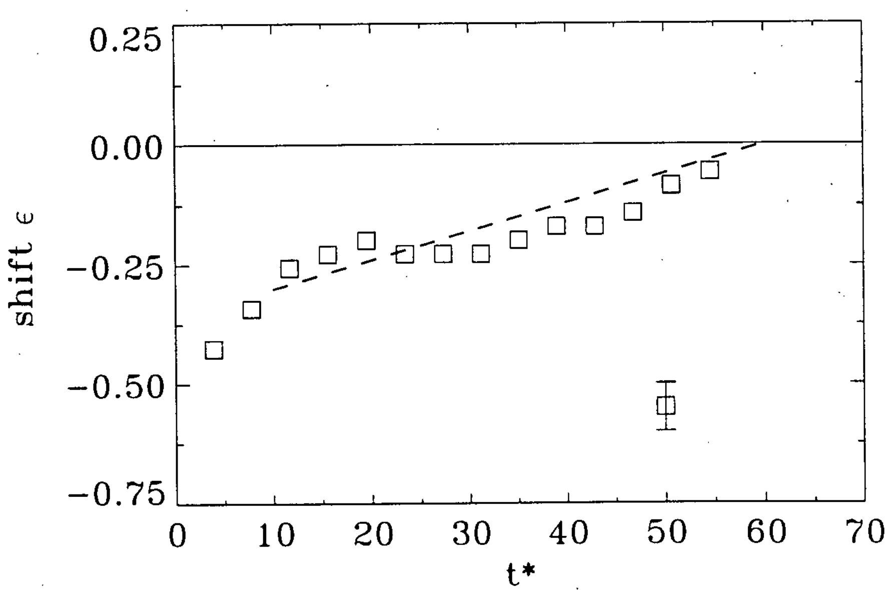

Figure 7.8 Prediction of the shift from the wave speeds using $\varepsilon = -(c_r^+ + c_r^-)$, compared with the measurements. – – – –, prediction of the shift; □, measured shift in Exp. 2.

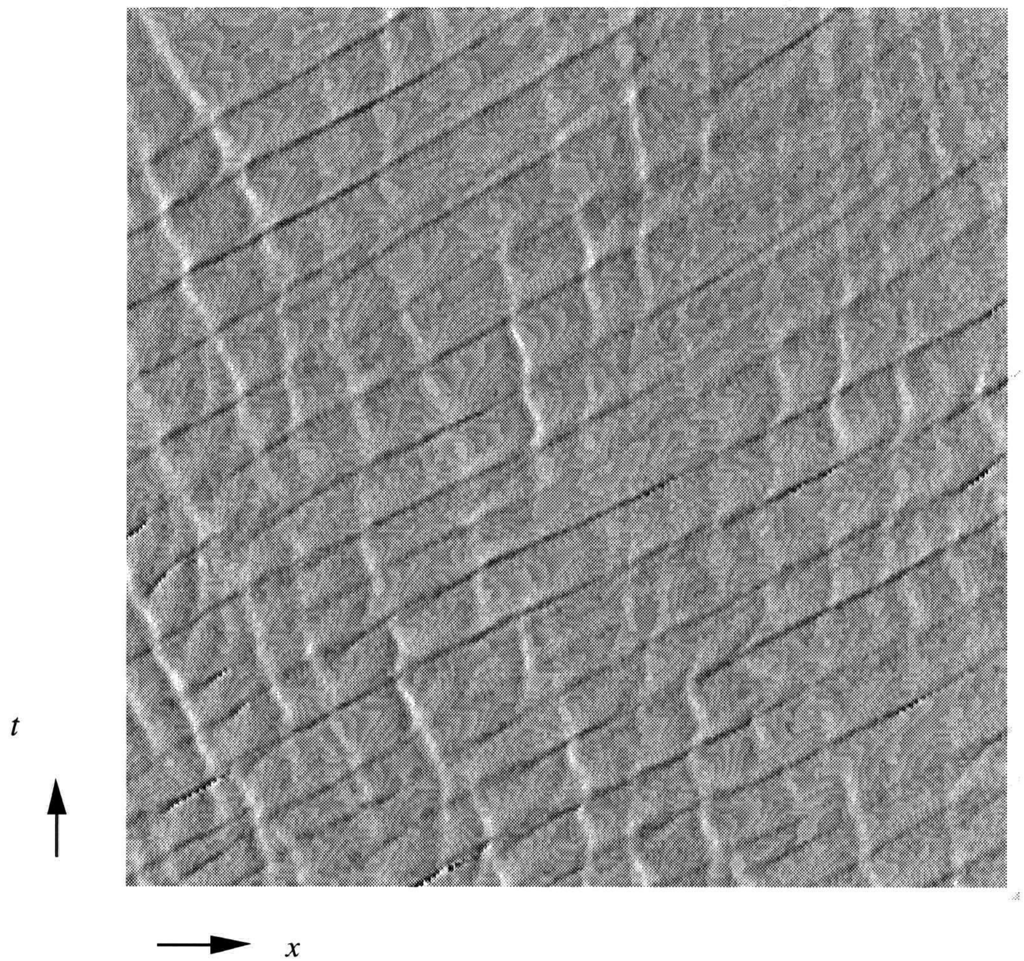

Figure 7.9 Interactions of wave speeds observed in Exp. 9. The positive and negative waves are seen as the dark and bright bands. The horizontal length is 92 cm, and $t^* = 40 \sim 44$. The flow has $\varepsilon \approx 0$, $J \approx 0.45$, and $Re \approx 1580$.

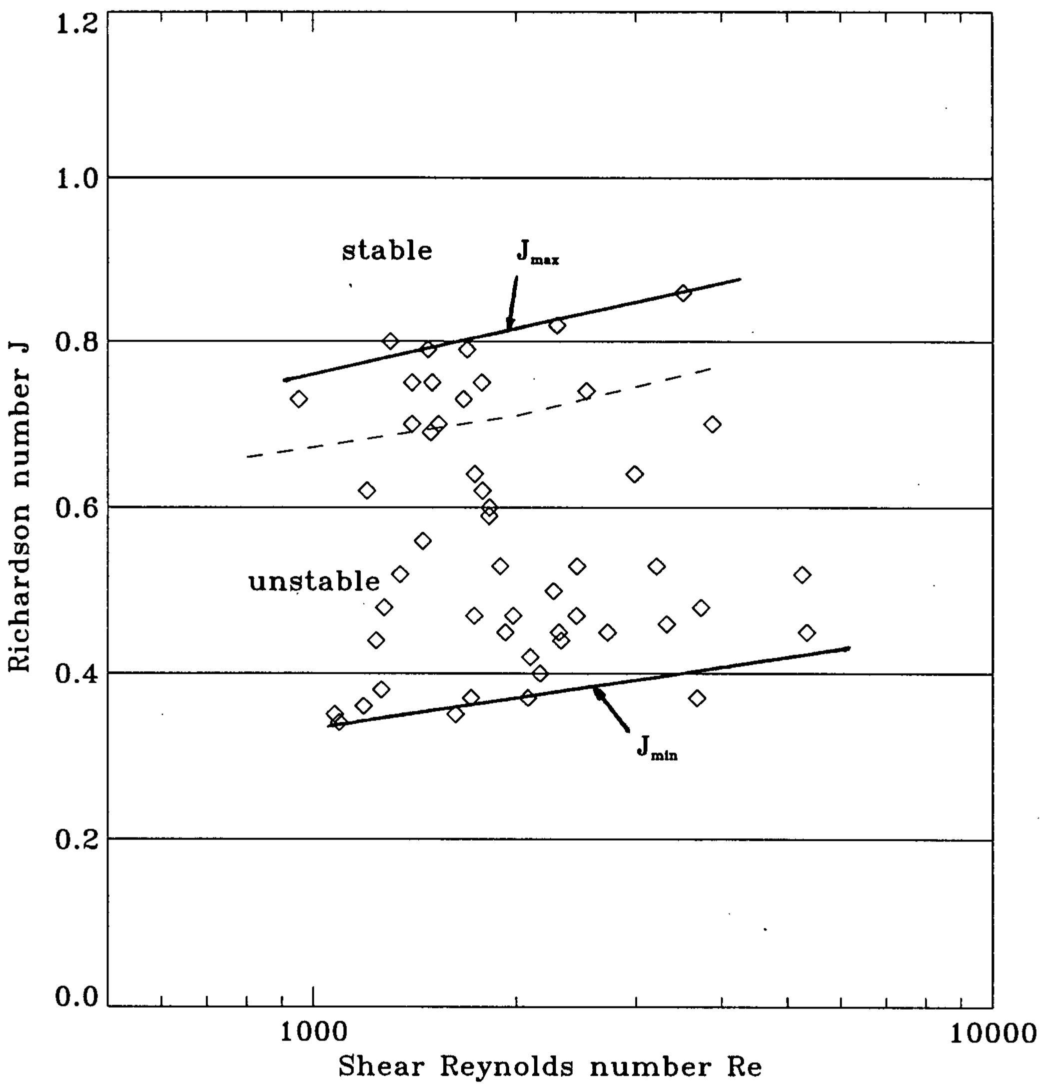

Figure 7.10 Conditions for Holmboe instabilities on a (*Re*, *J*) plot. ◊, flow conditions with Holmboe instabilities observed. ——, J_{min} and J_{max} obtained from measurements; – – – –, prediction of Nishida & Yoshida (1987).

(a) Thermally stratified flow

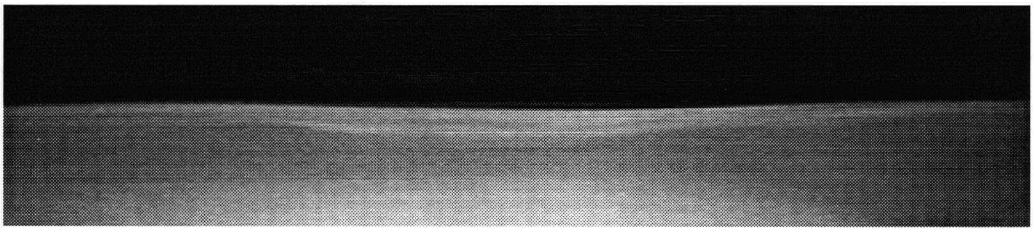

(b) Salinity stratified flow

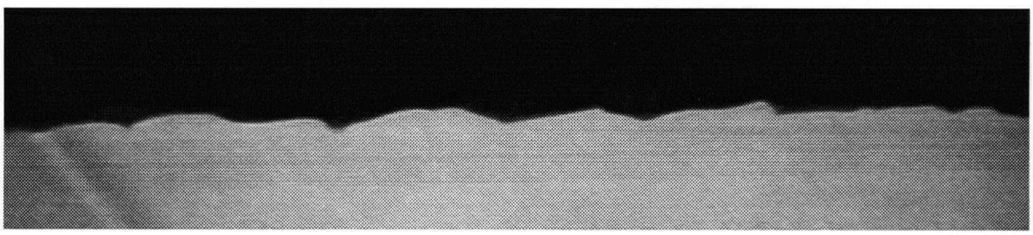

Figure 7.11 Observations of the interface in the experiments with thermally and salinity stratified flows. (a) Thermally stratified flow (Exp. 5) with T_1 = 27 °C and T_2 = 16 °C. $J \approx 0.32$ and $Re \approx 1800$. (b) Salinity stratified flow (Exp. 4), with $J \approx 0.32$ and $Re \approx 2100$.

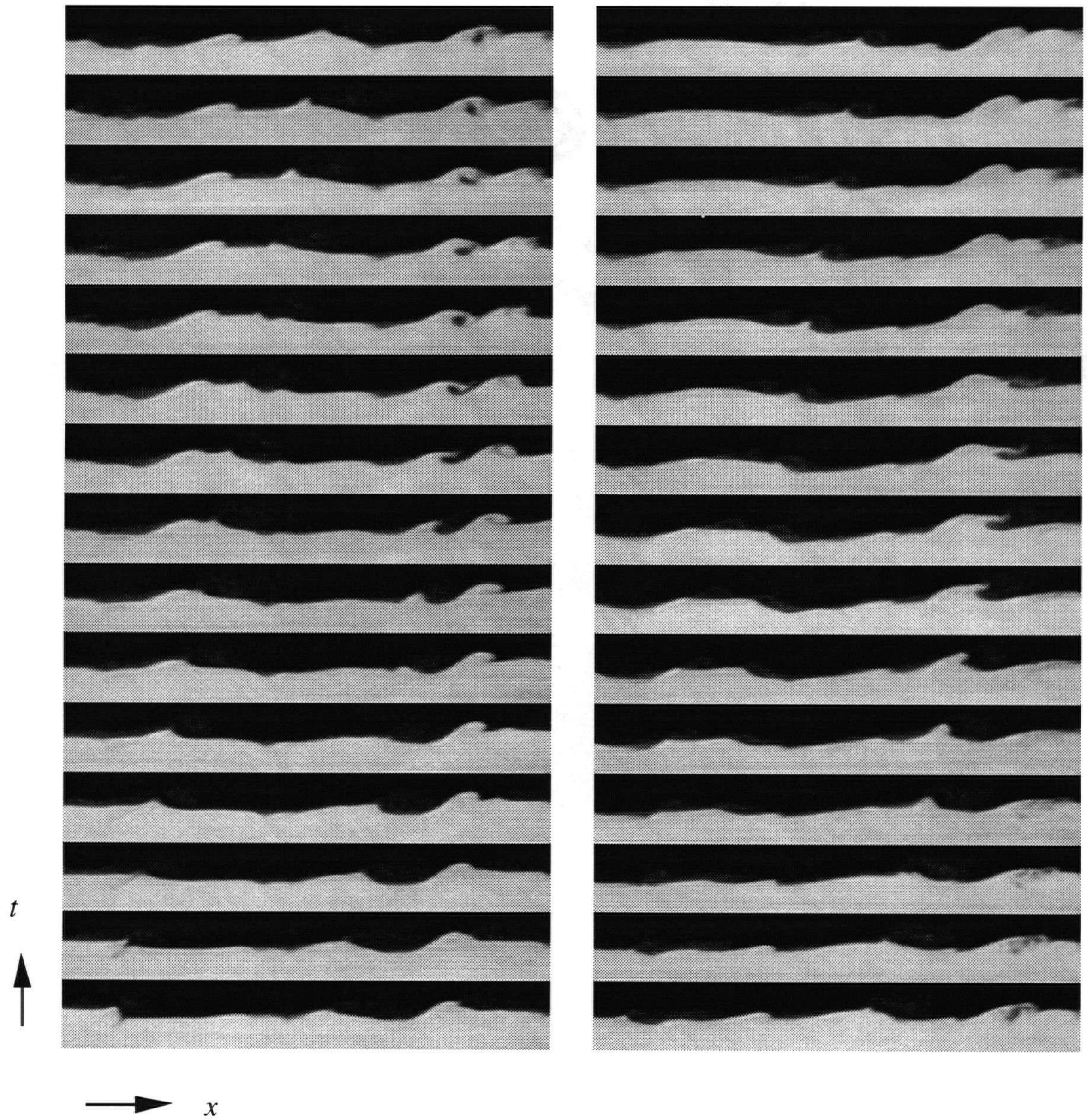

Figure 7.12 Series of images showing the deformation of interfacial waves in Exp. 4 starting t^* = 19 (5 minutes). Images were captured at Δt = 0.5 seconds. The horizontal length is 32 cm.

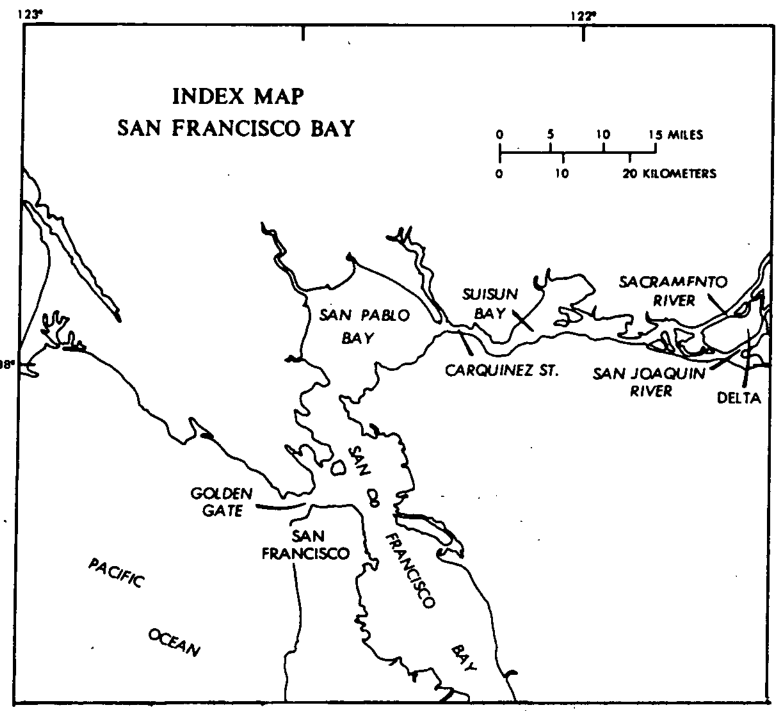

Figure 8.1 Map showing the location of the Carquinez Strait in San Francisco Bay.

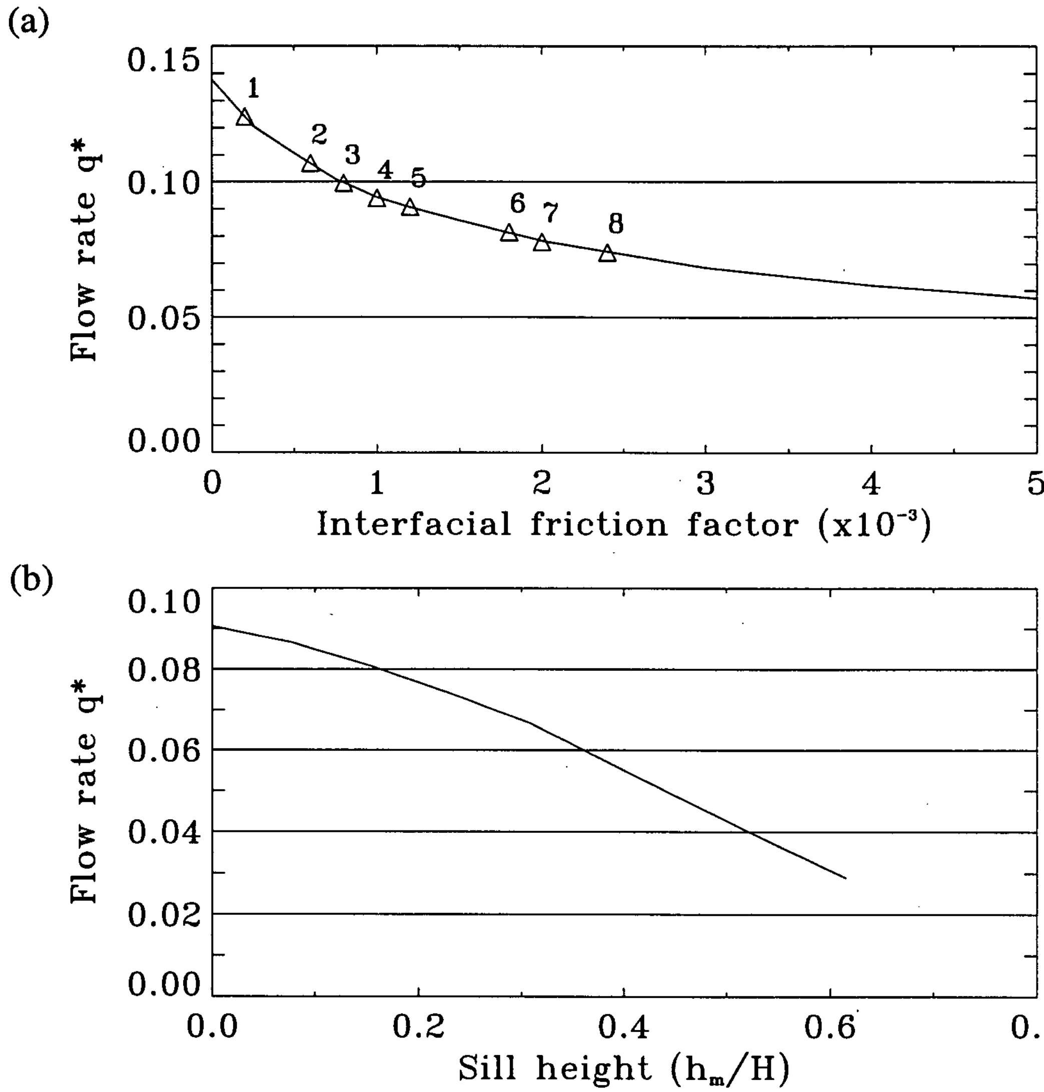

Figure 8.2 Prediction of the maximal exchange flow through the Carquinez Strait. (a) Flow rate against interfacial friction factor f_I with $f_w = 0.005$. Numbers indicate the f_I values predicted using various methods. $Q = 663\ m^3/s$, $\delta \approx 2$ m, $y_1 = y_2 = 6.5$ m are used in the predictions.

1. Oguz *et al.* (1990) for Bosphorus Strait;
2. Arita & Jirka (1987);
3. Sherenkov *et al.* (1971);
4. Bo Pederson (1986);
5. Dermissis & Parthenlades (1984);
6. Abraham *et al.* (1979);
7. Hamblin & Lawrence (1990) for Burlington Ship Canal;
8. Oguz & Sur (1989) for Dardanelles Strait.

(b) Flow rate against the sill height, with $f_w = 0.005$ and $f_I = 0.0012$.